

From Supernovae to Neutron Stars: A Systematic Approach to Axion Production at Finite Density

Konstantin Springmann,^{a,b} Michael Stadlbauer,^{a,c} Stefan Stelzl,^d Andreas Weiler^a


^a*Technical University of Munich, TUM School of Natural Sciences, Physics Department, James-Frank-Str. 1, 85748 Garching, Germany*

^b*Department of Particle Physics and Astrophysics, Weizmann Institute of Science, Rehovot, Israel 7610001*

^c*Max Planck Institute for Physics, Boltzmannstr. 8, 85748 Garching, Germany*

^d*Institute of Physics, Theoretical Particle Physics Laboratory, École Polytechnique Fédérale de Lausanne, CH-1015 Lausanne, Switzerland*

E-mail: konstantin.springmann@weizmann.ac.il,
michael.stadlbauer@tum.de, stefan.stelzl@epfl.ch,
andreas.weiler@tum.de

ABSTRACT: We present a systematic study of QCD axion production in environments with finite baryon density and temperature, implying significant changes to axion phenomenology. Within heavy baryon chiral perturbation theory, we derive the effective Lagrangian describing axion interactions with nucleons and mesons up to next-to-leading-order in the chiral expansion. We focus on corrections to the axion-nucleon couplings from higher orders and finite density. These couplings are modified by up to an order of magnitude near nuclear saturation density, significantly impacting axion production in supernovae and neutron stars. Density-dependent corrections enhance the axion luminosity in supernovae by an order of magnitude, strengthening current best bounds by a factor of three. We stress the importance of including all axion production channels up to a given chiral order for a consistent luminosity calculation and classify the missing contributions up to the third chiral order. The modified axion-nucleon couplings also affect neutron star cooling rates via axion emission. A re-evaluation of existing neutron star cooling bounds, constrained to regions where perturbative control is reliable, weakens these bounds by a factor of four. Lastly, our results have implications for terrestrial axion searches that rely on precise knowledge of axion-nucleon couplings. 

Contents

1	Introduction	1
2	Axion Heavy Baryon Chiral Perturbation Theory	4
2.1	From the Axion QCD Lagrangian ...	4
2.2	... to Axion Chiral Perturbation Theory ...	5
2.3	... to Axion Heavy Baryon Chiral Perturbation Theory...	7
2.4	... to Axion Heavy Baryon Theory	9
3	Axion Couplings in Heavy Baryon Chiral Perturbation Theory	10
3.1	Axion-nucleon couplings in vacuum	10
3.1.1	Consistent choice of Lagrangian parameters	14
3.1.2	Results	15
3.2	Axion-nucleon couplings at finite density	18
3.2.1	Axion-nucleon vertex corrections	19
3.2.2	Results	21
4	Implications of density and momentum dependent couplings	25
4.1	Supernova cooling bound	25
4.2	Neutron star cooling bound	30
4.3	Terrestrial experiments	32
5	Conclusions	33
A	Construction of the effective axion HBChPT Lagrangian	37
A.1	Chiral QCD Lagrangian	37
A.2	Effective Pion Lagrangian	37
A.3	Effective Baryon Lagrangian	38
A.4	Construction of nucleon contact terms	45
A.4.1	Pure nucleon contact terms	46
A.4.2	Higher order nucleon contact terms	46
B	Cooling rates at finite density	47
B.1	Nucleon propagator in thermal field theory	47
B.2	Particle production rates	50
B.3	Cutting rules at finite density	51
B.4	Axion emissivity from supernova explosions	53
C	Explicit loop calculations	55
C.1	Useful integrals	55
C.1.1	Integrals for vacuum form factor	55
C.1.2	Integrals for finite density form factor	56

C.2	Loop corrections in vacuum	57
C.2.1	Renormalization	58
C.3	Density corrections	59
C.3.1	Isospin symmetric matter	59
C.3.2	Arbitrarily mixed matter	60
C.4	DFSZ axion additional results	61
D	Temperature corrections	63
	Bibliography	67

1 Introduction

In recent years, there has been a resurgence of interest in the QCD axion, both as a solution to the strong CP problem [1–4] and as a compelling dark matter candidate [5–7]. This attention is driven by a robust experimental program, accompanied by the emergence of novel theoretical concepts and refinements of astrophysical constraints.

Astrophysical environments, such as supernovae (SNe) and neutron stars (NSs) are excellent laboratories to test the physics of weakly coupled (light) scalar fields such as the QCD axion [8–15], for recent reviews see *e.g.* [16, 17]. They are particularly relevant because of the large temperatures or large number density of SM particles, which can compensate for the weak coupling of the QCD axion to these particles. The constraints from the observation of the neutrino signal from SN 1987A and the observation of NS cooling rates set the most stringent constraints on the QCD axion, see *e.g.* [11, 12, 18–24].


In this work, we revisit the theory prediction of axion production in dense and hot baryonic matter, focussing on the regime where the axion can freely escape the SN or the NS. While previous works include density and temperature effects on production rates in a phenomenological manner or ignore them altogether, a systematic treatment of the interactions of axions with nucleons in a thermal bath and finite density background is still missing [23, 24]. Concretely, for the first time, we systematically calculate axion production rates within the framework of Chiral Perturbation Theory (ChPT) expansion, where reliable theory error estimates are possible. We focus on the dominant axion production mechanism in NS and SN matter environments, $NN \rightarrow NN a$, where $N = (p, n)^T$ is the nucleon field. In this work, we take the first step towards a systematic evaluation of this rate. In particular, we include higher order and finite density corrections to the axion-nucleon coupling. This leads to significant changes in the axion luminosity during SN 1987A and from NSs and, hence, effects resulting bounds on the QCD axion decay constant f_a .

Our main tools for this systematic calculation are various effective field theories (EFTs) for the QCD axion. Starting at energies above the QCD scale, we match to the ChPT Lagrangian of mesons and nucleons at two flavors $N_f = 2$, which is valid at energies below the cut-off Λ_χ , which is around the QCD scale where baryons are non-relativistic. We then

integrate out the pions and arrive at an effective theory of baryons and the axion only [25]. Note that at densities within SNe or NSs, pion dynamics are crucial. Keeping the pions as part of our effective theory, we investigate the couplings of the QCD axion to nucleons within the controlled expansion of heavy baryon ChPT.

We find that the couplings of the QCD axion to protons and neutrons depend on axion energy ω_a , the nucleon chemical potential as well as the temperature. We estimate the uncertainty due to the truncation of the chiral expansion and due to the uncertainty in low energy constants (see e.g. Fig. 5 for the KSVZ axion). Furthermore, a background of nucleons can change the potential of the QCD axion as well as other light particles. The phenomenology of these effects has largely been worked out in [26–32].

Here, we calculate the modification of the axion production rate, focusing on the QCD axion coupling to nucleons due to higher-order corrections and interactions with the density background. The impact of finite density on the QCD axion-nucleon coupling was first explored in [27], where an initial estimate of the coupling magnitude was provided. Notably, a change of up to $\mathcal{O}(10)$ in the coupling of a KSVZ axion to the neutron has been estimated. Our findings indicate that at nuclear saturation density, $n_0 \simeq 0.16 \text{ fm}^{-3}$, the KSVZ axion couplings undergo significant changes. Specifically, the proton coupling exhibits a relative change of $\mathcal{O}(1)$, while the neutron coupling shows a change of $\mathcal{O}(10)$, consistent with the previous estimate (see also *e.g.* Fig. 8).

The substantial magnitude of these effects can be attributed to the proximity of the theory’s cutoff. In particular, the dominant effects are naively $(k/\Lambda_\chi)^3$ suppressed, where k is the typical momentum and Λ_χ is the UV-cutoff of the theory. However, the naive power counting is mitigated by the existence of a low-lying $\Delta(1232)$ -resonance, which amplifies the effects. Thus, certain contributions are only suppressed by $(k/\Lambda_\chi)^2(k/\delta m_{N-\Delta})$, *i.e.* by the mass difference $\delta m_{N-\Delta}$ between the nucleons and the $\Delta(1232)$ -resonance [33]. Note that while for the form factors in vacuum, we generically find $k = k_0 = \{\omega_p, \omega_a\}$, *i.e.* an expansion in energy, in the case of a density background, we instead find an expansion in k_f/Λ_χ , where k_f is the Fermi momentum of the background nucleons. This shows that in the limit $\omega_a \rightarrow 0$, density effects dominate since $\omega_p \simeq k_f^2/2m_N \ll k_f$, where m_N is the nucleon mass. The systematic expansion allows us to estimate an error in our predictions due to missing higher-order terms. In a supplementary material, we provide numerical tables of the density and temperature dependence of the axion-nucleon couplings for use in dedicated supernova simulations. These tables can be accessed at our GitHub repository ¹ .

The effective couplings are of significant importance both for astrophysical constraints on the QCD axion as well as for terrestrial experiments. On the astrophysical side, we explore the modifications of the supernova bound as well as neutron star cooling bounds. Within supernovae, axions are dominantly produced by nucleon axion Bremsstrahlung process, $NN \rightarrow NN a$ [12]. If the axion luminosity during the supernova exceeds the neutrino luminosity, a shorter neutrino signal would have been observed from SN 1987A. We find that by including density dependent axion-nucleon couplings, the supernova axion

¹<https://github.com/michael-stadlbauer/Axion-Couplings.git>

bound on f_a is strengthened by a factor of a few compared to previous works. In particular, we find

$$f_a \gtrsim 1.0_{-0.2}^{+0.5} \times 10^9 \text{ GeV}, \quad m_a \lesssim 5.9_{-2.0}^{+1.8} \text{ meV}, \quad (\text{KSVZ}) \quad (1.1)$$

for the KSVZ axion.

Density-dependent axion-nucleon couplings are, however, not the only contributions to the $NN \rightarrow NNa$ process. We hence classify all the relevant topologies that contribute to the process up to order $(k/\Lambda_\chi)^3$. The evaluation of these extends the scope of this work and is left for a separate publication, which replaces phenomenological approaches and paves the way to a consistent and systematic axion production in SNe and NS environments.

The breakdown of the effective theory at high densities, as found in NSs, challenges the common interpretation of NS bounds [22].

While a significant portion of the NS’s luminosity originates from regions with densities around $(0.5 - 2)n_0$, the exact contribution depends on the NS’s maximum mass and the chosen equation of state. However, an order-one fraction of the luminosity comes from the deep core, where the ChPT expansion is not valid.

This limitation presents two potential approaches for addressing the high-density region. The first approach sets the axion cooling bound by considering only the parts of the NS where controlled calculations are feasible—specifically, regions with densities below nuclear saturation density. This approach neglects a substantial portion of the NS, typically resulting in a weakening of the cooling bound by roughly a factor of four. Within this framework, the emissivity can be systematically calculated using finite-density couplings. For the KSVZ axion, this method reduces the bound by an additional factor of two due to the density corrections to the couplings.

The second, less rigorous approach involves estimating axion production in the high-density region by approximating the axion couplings using naive dimensional analysis (NDA). In this scenario, there is generally no clear theoretical prediction that differentiates between various axion models. Instead, all models predict roughly the same rate in the high-density region and have an uncertainty of $\mathcal{O}(1)$. This suggests that vacuum couplings have minimal influence on NS cooling via axions.

Finally, our findings have significant implications for axion dark matter experiments that target the axion-nucleon coupling [34–53]; the bulk of a nucleus effectively serves as a background density for the nucleon interacting with the axion. This effect is reminiscent of the quenching of the axial coupling g_A as measured in beta decay in large nuclei [54, 55]. Understanding the QCD axion couplings to matter is particularly crucial in spin precession experiments, especially if axion detection occurs, as it could provide insights into possible ultraviolet (UV) completions. Similarly, non-derivative axion-nucleon couplings undergo corrections in a comparable manner, although these corrections have yet to be fully calculated. This is relevant for both current and future searches for new physics using nuclear clocks, including those involving the recent measurement of the low-lying transition in the ^{229}Th nucleus [56–60].

The paper is organized as follows. In Sec. 2, we review the EFTs describing the interactions of the axion at different energies, with a particular emphasis on the EFT that

will be used later on, heavy baryon ChPT (HBChPT). In Sec. 3.1, we calculate the axion couplings within this framework, including two subleading orders. In Sec. 3.2, we extend this analysis to calculate the effective axion-nucleon coupling in the presence of a nucleon density background. Finally, in Sec. 4, we explore phenomenological implications of the above findings. In Sec. 4.1 we re-evaluate the axion luminosity during SN explosions, in Sec. 4.2 we study the impact on neutron star cooling and in Sec. 4.3 we comment on implications for terrestrial axion searches. We conclude in Sec. 5. A comprehensive derivation of the next-to-leading order terms of the heavy baryon Lagrangian is provided in App. A. In App. B, we review calculations of particle production rates at finite temperature and chemical potential, focusing specifically on the case of axion-nucleon couplings. In App. C, we show additional details of the explicit loop calculation, as well as some further results for the DFSZ axion. Finally, in App. D, we investigate the relative importance of temperature compared to chemical potential.

2 Axion Heavy Baryon Chiral Perturbation Theory

In this section, we review chiral perturbation theory in the heavy baryon limit, including the QCD axion. We start with the QCD Lagrangian extended by the axion in the UV and construct the effective theory of non-relativistic baryons, pions, and the axion for two light quark flavors. Finally, at momenta below the pion mass, we integrate out the pions and match our EFT with the one found in [25].

2.1 The Axion QCD Lagrangian

Below the scale of electroweak symmetry breaking the effective Lagrangian of QCD, including the QCD axion field $a(x)$, with decay constant f_a is given by

$$\mathcal{L}_{\text{QCD}} = \mathcal{L}_{\text{QCD},0} - \bar{q}M_q q + \frac{1}{2}(\partial a)^2 + \frac{a}{f_a} \frac{g^2}{32\pi^2} G^{\mu\nu} \tilde{G}_{\mu\nu} + \frac{\partial_\mu a}{2f_a} J_{\text{PQ},0}^\mu, \quad (2.1)$$

where

$$\mathcal{L}_{\text{QCD},0} = -\frac{1}{4}G^{\mu\nu}G_{\mu\nu} + i\bar{q}\not{D}q, \quad (2.2a)$$

$$J_{\text{PQ},0}^\mu = \sum_q c_q^0 \bar{q} \gamma^\mu \gamma_5 q. \quad (2.2b)$$

In the chiral limit, the theory is classically invariant under the symmetry group

$$SU(3)_c \times SU(N_f)_L \times SU(N_f)_R \times U(1)_V \times U(1)_A. \quad (2.3)$$

For simplicity we neglect the effects of the strange quark and take the number of light quark flavors to be $N_f = 2$, such that $M_q = \text{Diag}(m_u, m_d)$. $J_{\text{PQ},0}^\mu$ is the model-dependent axial quark current associated with the spontaneously broken Peccei-Quinn (PQ) symmetry $U(1)_{\text{PQ}}$, with the axion as Nambu-Goldstone Boson (NGB). The axion-gluon coupling can be removed by performing a chiral rotation on the quark fields

$$q \rightarrow e^{\frac{ia}{2f_a} \gamma_5 Q_a} q, \quad q = (u, d)^T, \quad (2.4)$$

with Q_a an arbitrary matrix in flavor space, as long as $\text{Tr}[Q_a] = 1$. It is defined as

$$Q_a = \frac{\text{Diag}[1, z]}{1 + z} + \text{corrections}, \quad z \equiv \frac{m_u}{m_d}, \quad (2.5)$$

to remove the leading order tree level mixing of the axion with the pion [25], resulting from Eq. (2.14). At next-to-leading order additional mixing terms arise Eq. (2.18), which modify Q_a , see Eq. (2.19). In this basis, the Lagrangian above the QCD confinement scale reads

$$\mathcal{L}_{\text{QCD}} = \mathcal{L}_{\text{QCD},0} - (\bar{q}_L M_a q_R + \text{h.c.}) + \frac{1}{2} (\partial a)^2 + \frac{\partial_\mu a}{2f_a} J_{\text{PQ}}^\mu, \quad (2.6)$$

where M_a is the axion dressed quark matrix and J_{PQ}^μ the shifted PQ current

$$M_a \equiv e^{\frac{ia(x)}{2f_a} Q_a} M_q e^{\frac{ia(x)}{2f_a} Q_a}, \quad (2.7a)$$

$$J_{\text{PQ}}^\mu = \sum_{q=u,d} c_q^{\text{UV}} \bar{q} \gamma^\mu \gamma_5 q, \quad c_q^{\text{UV}} \equiv c_q^0 - [Q_a]_q. \quad (2.7b)$$

The couplings c_q^{UV} are defined at energies around f_a . At the scales of interest, *i.e.* around the QCD scale, the couplings are given by [25]

$$c_q \equiv c_q^{\text{IR}} \simeq C_{qq'} c_{q'}^{\text{UV}}, \quad C_{qq'} = \begin{cases} 0.975 & q = q' \\ -0.024 & q \neq q' \end{cases}, \quad (2.8)$$

which follow from RG evolution. Decomposing the PQ current into isoscalar and isovector, we find

$$J_{\text{PQ}}^\mu = \bar{q} \gamma^\mu \gamma_5 \left(c_{u+d} \frac{\partial_\mu a}{2f_a} \mathbb{1} + c_{u-d} \delta_{b3} \frac{\partial_\mu a}{2f_a} \tau^b \right) q, \quad (2.9)$$

where

$$c_{u\pm d} = (c_u \pm c_d)/2 \quad (2.10)$$

contain the corresponding contribution from Q_a .

2.2 Axion Chiral Perturbation Theory

At low energies QCD confines and forms a chiral condensate $|\langle \bar{q}_L q_R + \text{h.c.} \rangle| \equiv B f_\pi^2$, spontaneously breaking the approximate chiral symmetry

$$SU(2)_L \times SU(2)_R \times U(1)_V \rightarrow SU(2)_{L+R} \times U(1)_V. \quad (2.11)$$

The low energy degrees of freedom are described as fluctuations around the chiral condensate by the unitary 2×2 matrix in flavor space

$$U = e^{i \frac{\Pi}{f_\pi}}, \quad \Pi = \pi^a \tau^a = \begin{pmatrix} \pi^0 & \sqrt{2} \pi^+ \\ \sqrt{2} \pi^- & -\pi^0 \end{pmatrix}, \quad (2.12)$$

with the pion decay constant $f_\pi \simeq 93 \text{ MeV}$. This leads to the EFT of pions, a systematic expansion in small pion momenta $p/(4\pi f_\pi)$, called chiral perturbation theory (ChPT) [61–63]. Note that a generalization to three flavors is straightforward but will not alter the results below. The pion Lagrangian is

$$\mathcal{L}_{\pi\pi} = \mathcal{L}_{\pi\pi}^{(2)} + \mathcal{L}_{\pi\pi}^{(4)} + \dots, \quad (2.13)$$

where $\mathcal{L}_{\pi\pi}^{(2)}$ is the leading pion axion Lagrangian given by

$$\mathcal{L}_{\pi\pi}^{(2)} = \frac{f_\pi^2}{4} \text{Tr} \left[\nabla_\mu U (\nabla^\mu U)^\dagger + \left(\chi U^\dagger + \chi^\dagger U \right) \right], \quad (2.14)$$

with² $\chi = 2BM_d^\dagger$, and where the covariant derivative ∇_μ is given by

$$\nabla_\mu U = \partial_\mu U - i \{a_\mu, U\} - 2ia_\mu^s U. \quad (2.15)$$

Here the isovector and isoscalar axion currents are

$$a_\mu = c_{u-d} \frac{\partial_\mu a}{2f_a} \tau_3, \quad \text{and} \quad a_\mu^s = c_{u+d} \frac{\partial_\mu a}{2f_a} \mathbb{1}, \quad (2.16)$$

as can be seen from Eq. (2.9). For details about the construction, see App. A. Note that Eq. (2.14) gives the leading order QCD axion mass [25],

$$m_a^2 = \frac{z}{(1+z)^2} \frac{m_\pi^2 f_\pi^2}{f_a^2}. \quad (2.17)$$

We now want to eliminate all the axion-pion mixing at next-to-leading order. The mixing comes from loops from the leading order Lagrangian $\mathcal{L}_{\pi\pi}^{(2)}$ as well as tree level contributions from the next-to-leading order Lagrangian $\mathcal{L}_{\pi\pi}^{(4)}$. The loop level mixing between a and π^0 generated from $\mathcal{L}_{\pi\pi}^{(2)}$ is however suppressed by m_a^2 and thus negligible. There is a single term in $\mathcal{L}_{\pi\pi}^{(4)}$ that gives rise to tree level mixing [62]

$$\mathcal{L}_{\pi\pi}^{(4)} \supset -\frac{\ell_7}{16} \left(\text{Tr} \left[\chi U^\dagger - \chi^\dagger U \right] \right)^2. \quad (2.18)$$

We can remove this additional contribution to the mixing by choosing

$$Q_a = \frac{\text{Diag} [1, z]}{1+z} - 4\ell_7 \frac{m_\pi^2 (1-z)z}{f_\pi^2 (1+z)^3} \tau^3. \quad (2.19)$$

We see that it contributes to the isovector coupling c_{u-d} but leaves the isoscalar coupling c_{u+d} unchanged, see Eq. (2.9).

Next, we include baryons in our theory. Since their mass is at the ChPT cut-off, no consistent power counting scheme can be found for relativistic nucleons and antinucleons. Treating the nucleons as heavy and non-relativistic, a systematic expansion in p/Λ_χ is available, see e.g. [61, 64–67]. Here $\Lambda_\chi \sim 700 \text{ MeV}$ is the cutoff chosen such that most Wilson coefficients are $O(1)$. The leading order chiral pion-nucleon Lagrangian [62] can be extended to include the axion [25]

$$\mathcal{L}_{\pi N}^{(1)} = \bar{\Psi} \left(i\not{D} - m_N + \frac{g_A}{2} \not{a} \gamma_5 + \frac{g_0}{2} \not{a} \gamma_5 \right) \Psi, \quad (2.20)$$

²Note that, in accordance with the standard convention in ChPT, the strong coupling constant and the Wilson coefficient, which relate the pion mass and the product of f_π and the quark masses, are included in χ . Consequently, the coefficients for operators involving higher powers of χ are small, as evidenced e.g. by the coefficient ℓ_7 .

with $\Psi = (p, n)^T$ being the nucleon isospin doublet. The usual building blocks of chiral perturbation theory are given by

$$D_\mu \Psi = \partial_\mu \Psi + \Gamma_\mu \Psi, \quad (2.21a)$$

$$\Gamma_\mu = \frac{1}{2}[u^\dagger, \partial_\mu u] - \frac{i}{2}u^\dagger a_\mu u + \frac{i}{2}u a_\mu u^\dagger, \quad (2.21b)$$

$$u_\mu = i \left\{ u^\dagger, \partial_\mu u \right\} + u^\dagger a_\mu u + u a_\mu u^\dagger, \quad \hat{u}_\mu = u^\dagger a_\mu^s u + u a_\mu^s u^\dagger, \quad (2.21c)$$

with $u = \sqrt{U}$. Note that u_μ and \hat{u}_μ are isovector and isoscalar quantities, respectively. See App. A for a detailed derivation of the NLO Lagrangian $\mathcal{L}_{\pi N}^{(2)}$.

2.3 Axion Heavy Baryon Chiral Perturbation Theory...

The Lagrangian in Eq. (2.20) describes the leading order interactions of non-relativistic nucleons with pions and the axion. To simplify, we decompose the nucleon momentum into a piece proportional to its mass and a small residual momentum

$$p^\mu = m_N v^\mu + k^\mu, \quad (2.22)$$

where we choose $v^\mu = (1, \vec{0})^T$, which leads to a double expansion in k/m_N and k/Λ_χ , called heavy baryon chiral perturbation theory (HBChPT) [64, 68], and see *e.g.* for reviews [33, 69, 70]. We split Ψ into velocity-dependent heavy and light components and integrate out the heavy component (see App. A for details). This is analogous to the construction of heavy quark effective theory (HQET) [71–74]. The Lagrangian Eq. (2.20) at leading order in HBChPT is

$$\hat{\mathcal{L}}_{\pi N}^{(1)} = \bar{N} \left(i v \cdot D + g_A S \cdot u + g_0 S \cdot \hat{u} \right) N, \quad (2.23)$$

with $S^\mu = \frac{i}{2} \gamma_5 \sigma^{\mu\nu} v_\nu = (0, \vec{\sigma}/2)$. Here $N \equiv e^{im_N v \cdot x} P_+ \Psi$ is the light component of the field Ψ , with $P_+ = (1 + \not{v})/2$ the corresponding projection operator. The leading order nucleon contact interactions are

$$\hat{\mathcal{L}}_{NN}^{(1)} = -\frac{1}{2} C_S (\bar{N} N)(\bar{N} N) + 2C_T (\bar{N} S N) \cdot (\bar{N} S N). \quad (2.24)$$

In this context, leading order refers to a systematic diagrammatic power counting in HBChPT, developed in [61, 64–67], where we treat k/Λ_χ on the same footing as k/m_N . We define the chiral order ν of the expansion as $(k/\Lambda_\chi)^\nu$, where k can denote both $|\vec{k}|$ or k_0 . For a Feynman diagram with two external nucleons ν is given by

$$\nu = 2L + \sum V_i \Delta_i, \quad \Delta_i = d_i + \frac{1}{2} n_i - 2, \quad (2.25)$$

where L is the number of loops and Δ_i is the order of each vertex, appearing V_i times in the diagram. Here d_i is the number of derivatives or m_π insertions, and n_i denotes the number of nucleon lines associated with the vertex i . Note, that for the vertices of the leading order Lagrangians Eqs. (2.23), (2.14), and Eq. (2.24) one finds $\Delta_i = 0$.

On the other hand, for very low momenta, the existence of bound states interferes with our power counting. In the environments we are interested in, typical nucleon energies are

large compared to typical bound state energies, allowing us to ignore their effects. Implicitly, this coincides with only keeping the leading term in an expansion in $(m_N E_B/p^2) \ll 1$, where $E_B \sim \mathcal{O}(\text{MeV})$ is the binding energy of bound states such as deuteron.

In the non-relativistic limit, the nucleon propagator only has a single pole in the complex plane. Consequently, pure nucleon loops (with more than one nucleon propagator) do not contribute. In other words, anti-nucleons are not included in our EFT.

The next-to-leading order pion-nucleon and contact interaction interactions, which include the QCD axion, are constructed in App. A, see Eq. (A.51) and Eqs. (A.60), (A.62). We find

$$\begin{aligned} \hat{\mathcal{L}}_{\pi N}^{(2)} = & \bar{N} \left[-\frac{1}{2m_N} \left(D^2 - (v \cdot D)^2 + ig_A \{S \cdot D, v \cdot u\} + ig_0 \{S \cdot D, v \cdot \hat{u}\} \right) \right. \\ & + \hat{c}_1 \langle \chi_+ \rangle + \frac{\hat{c}_2}{2} (v \cdot u)^2 + \hat{c}_3 (u \cdot u) + \frac{\hat{c}_4}{2} i \epsilon^{\mu\nu\rho\sigma} [u_\mu, u_\nu] v_\rho S_\sigma \\ & \left. + \hat{c}_5 \tilde{\chi}_+ + \frac{\hat{c}_8}{4} (v \cdot u) (v \cdot \hat{u}) + \hat{c}_9 (u \cdot \hat{u}) \right] N, \end{aligned} \quad (2.26a)$$

$$\mathcal{L}_{\pi NN}^{(2)} = \frac{c_D}{2f_\pi^2 \Lambda_\chi} (\bar{N} N) (\bar{N} S \cdot u N) + \frac{\tilde{c}_D}{2f_\pi^2 \Lambda_\chi} (\bar{N} N) (\bar{N} S \cdot \hat{u} N), \quad (2.26b)$$

where the terms \hat{c}_8 , \hat{c}_9 and \tilde{c}_D have not been considered before. Here

$$\chi_\pm = u^\dagger \chi u^\dagger \pm u \chi^\dagger u, \quad \tilde{\chi}_\pm = \chi_\pm - \frac{1}{2} \langle \chi_\pm \rangle, \quad (2.27)$$

and $\langle \cdot \rangle$ denotes the flavor trace. Note that hatted constants are divided by one power of the cut-off, *i.e.* $\hat{c}_i = c_i/\Lambda_\chi$. Without any additional suppression, one naively expects $c_i \sim \mathcal{O}(1)$. Without a pseudo-scalar source, the coefficient \hat{c}_5 has only isospin-breaking effects. Its size is smaller than the naive estimate, as it is only generated by isospin-breaking physics in the UV.

However, other coefficients can be larger due to the low-lying $\Delta(1232)$ -resonance, which is only ~ 300 MeV above the nucleon mass [33, 75]. The $\Delta(1232)$ resonance has isospin $3/2$, and thus its presence can enhance the Wilson coefficients of the nucleon coupling to two isovectors, *i.e.* the coefficients \hat{c}_2 , \hat{c}_3 and \hat{c}_4 . This enhancement has important implications, as it interferes with naive power counting. As we will see, contributions that are naively suppressed can, in fact, be dominant due to this enhancement. This is the reason why we keep certain $\nu = 3$ terms in our calculation while including all terms up to $\nu = 2$ in our expansion³. Since the axion decay constant f_a is orders of magnitude larger than any other scale, terms with more than one axion are strongly suppressed. All relevant Feynman rules can then be calculated by expanding the fundamental building blocks, and keeping only

³In a separate publication [76] we investigate the model-independent bound on the QCD axion, *i.e.* assuming that all derivative couplings of the axion are negligible, as *e.g.* in the astrophobic axion [77]. In this case, the enhanced terms vanish, and we keep the non-enhanced terms at this order. We show that these non-derivative operators give rise to novel axion production channels, which we evaluate in supernova environments. The constraint we find is model-independent and exceeds similar current best bounds [78] by two orders of magnitude.

the leading terms we find

$$\hat{u}_\mu = c_{u+d} \left(\frac{\partial_\mu a}{f_a} \right) \mathbb{1} + \dots, \quad (2.28a)$$

$$u_\mu = - \left(\frac{\partial_\mu \pi^a}{f_\pi} \right) \tau^a + c_{u-d} \left(\frac{\partial_\mu a}{f_a} \right) \tau_3 + c_{u-d} \left(\frac{\pi^a \pi^b \partial_\mu a}{2f_a f_\pi^2} \right) \left(\tau^b \delta^{3a} - \tau^3 \delta^{ab} \right) + \dots, \quad (2.28b)$$

$$D_\mu = \partial_\mu + \dots, \quad (2.28c)$$

$$\langle \chi_+ \rangle = 4m_\pi^2 \left[1 - \frac{\pi^a \pi^b}{2f_\pi^2} \delta^{ab} \right] + \dots, \quad (2.28d)$$

$$\tilde{\chi}_+ = -2m_\pi^2 \frac{1-z}{1+z} \tau^3 - m_\pi^2 \frac{4z}{(1+z)^2} \left(\frac{\pi^a a}{f_\pi f_a} \right) \tau^a + \dots \quad (2.28e)$$

Contributions to D_μ including pion or axion fields are kinematically suppressed by $v \cdot k \sim \vec{k}^2/m_N$, and we do not include them here. In astrophysical environments such as neutron stars and supernovae, typical momenta can be high, and pion dynamics cannot be integrated out. While terrestrial experiments are generally performed at much lower energies, the nucleons can still have non-negligible (Fermi-)momenta [54], such that the pions are still important.

2.4 ... to Axion Heavy Baryon Theory

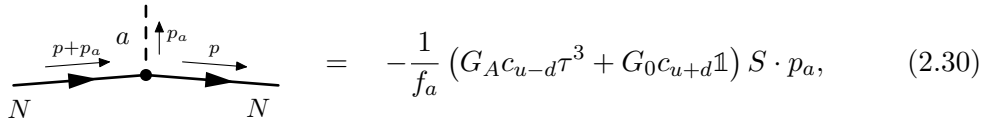
At even lower nucleon momenta $p \ll m_\pi$ one can integrate out the pion, see [25]. At these energies, the EFT at leading order takes the form

$$\begin{aligned} \mathcal{L}_{aN} = \bar{N} \left[i v \cdot \partial + \frac{S \cdot \partial a}{f_a} (G_A c_{u-d} \tau^3 + G_0 c_{u+d} \mathbb{1}) \right. \\ \left. + \sigma \langle \text{Re}(M_a) \rangle + b \text{Re} \left(M_a - \frac{1}{2} \langle M_a \rangle \right) + \dots \right] N. \end{aligned} \quad (2.29)$$

The isovector axial coupling $G_A = \Delta u - \Delta d = 1.2754(13)$ is known to high precision from measurements of nuclear β -decay [79] and the isoscalar axial combination $G_0 = \Delta u + \Delta d = 0.440(60)$ is inferred from the lattice [80], where we linearly added the statistical and systematic errors. From now on, we assume that the combined error is Gaussian.

Note that while the leading order isospin breaking effect is taken into account, *i.e.* $\propto c_{u-d}$, higher order isospin breaking terms, including the subleading axion pion mixing, are neglected here. The corrections from neglecting these terms are small and within the uncertainty of the choice of G_A , see [25]. Also, note that we slightly redefined the operators proportional to σ and b in comparison to [25] in order to separate them into isospin symmetric and isospin breaking contributions, respectively.

This Lagrangian gives rise to an axion nucleon vertex



$$\text{Diagram} = -\frac{1}{f_a} (G_A c_{u-d} \tau^3 + G_0 c_{u+d} \mathbb{1}) S \cdot p_a, \quad (2.30)$$

with model-dependent couplings

$$\begin{aligned} C_{ap} &= G_0 c_{u+d} + G_A c_{u-d} = -0.439(48) + 0.847(29)c_u^0 - 0.427(29)c_d^0, \\ C_{an} &= G_0 c_{u+d} - G_A c_{u-d} = 0.019(48) - 0.427(29)c_u^0 + 0.847(29)c_d^0. \end{aligned} \quad (2.31)$$

Note that for the KSVZ axion ($c_q^0 = 0$), there is a cancellation between two a priori unrelated terms in C_{an} , leading to a value compatible with zero.

3 Axion Couplings in Heavy Baryon Chiral Perturbation Theory

In this section, we examine the couplings of the QCD axion to nucleons both in vacuum and at finite density. By including pions in our theory, we first derive loop corrections to the axion-nucleon coupling identified in Axion Heavy Baryon Theory (see Eq. (2.31)) in Sec. 3.1. To evaluate these corrections, we match the Lagrangian constants to their experimentally determined values at the corresponding order in the chiral expansion. This approach reveals the non-trivial momentum dependence from higher-order corrections and reproduces the couplings of [25] in the small momentum limit. In the second part of this chapter, Sec. 3.2, we calculate the corrections to the couplings that arise in a finite-density background.

3.1 Axion-nucleon couplings in vacuum

We now discuss the couplings of the QCD axion to nucleons in vacuum up to chiral order $\nu = 3$. At this order, we focus on contributions enhanced by large Wilson coefficients from integrating the low-lying $\Delta(1232)$ -resonance, as they are numerically as significant as the $\nu = 2$ terms. These same diagrams will also lead to the dominant density modifications of the axion coupling in the subsequent section.

The leading order $\nu = 0$ axion-nucleon Lagrangian, according to Eq. (2.23), reads

$$\hat{\mathcal{L}}_{\pi N}^{(1)} \supset \left(\frac{\partial_\mu a}{f_a} \right) \bar{N} c_N S^\mu N, \quad N = (p, n)^T, \quad (3.1)$$

with the coupling given by

$$c_N = \text{Diag}(c_p, c_n) = g_A c_{u-d} \tau^3 + g_0 c_{u+d} \mathbb{1}. \quad (3.2)$$

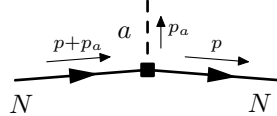
This leads to the $\Delta = 0$ (see Eq. (2.25)) Feynman rule of the tree-level axion-nucleon vertex within the HBChPT approximation,

$$\begin{array}{c} \begin{array}{c} \text{---} \xrightarrow{p+p_a} \bullet \xrightarrow{p} \text{---} \\ \uparrow a \\ \uparrow p_a \end{array} \\ N \qquad \qquad N \end{array} = -\frac{1}{f_a} \mathcal{A}^{(\nu=0)} S \cdot p_a = -\frac{1}{f_a} c_N S \cdot p_a, \quad (3.3)$$

where we introduced the form factor $\mathcal{A}^{(\nu=0)} = c_N$. We denote the vertices of this order ($\Delta = 0$) in all diagrams with a filled circle.

Higher order corrections start with a single tree level $\nu = 1$ diagram, containing only contributions from relativistic corrections to the leading order Lagrangian. At this order, no

new low-energy constants appear. Instead, we expect the contributions to be $\propto c_N \left(\frac{v \cdot p}{m_N}\right)$, where p is a typical nucleon momentum. Indeed, we find



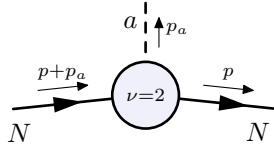
$$\begin{aligned}
&= -\frac{1}{f_a} \mathcal{A}^{(\nu=1)} S \cdot p_a - \frac{1}{f_a} \mathcal{B}^{(\nu=1)} S \cdot p \\
&= \frac{c_N}{2f_a m_N} (\omega - \omega_p) (S \cdot p_a + 2S \cdot p),
\end{aligned} \tag{3.4}$$

where we defined

$$\omega_a \equiv v \cdot p_a, \quad \omega_p \equiv v \cdot p, \quad \text{and} \quad \omega \equiv \omega_a + \omega_p, \tag{3.5}$$

and where we denote $\Delta = 1$ vertices by a filled square.

At chiral order $\nu = 2$, one-loop corrections start contributing and are renormalized by corresponding tree-level terms from $\hat{\mathcal{L}}_{\pi N}^{(3)}$. All relevant, *i.e.* non-zero $\nu = 2$ diagrams are shown in Fig. 1 and have been calculated in [81]. Note, however, that our result, which can be written as



$$= -\frac{1}{f_a} \mathcal{A}^{(\nu=2)} S \cdot p_a - \frac{1}{f_a} \mathcal{B}^{(\nu=2)} S \cdot p, \tag{3.6}$$

slightly differs from the result found in [81].⁴ We find the form factors \mathcal{A} and \mathcal{B} are given by

$$\begin{aligned}
\mathcal{A}^{(\nu=2)} &= -\frac{c_N}{4m_N^2} (\omega_p^2 - \omega^2 + \omega_p \omega - p^2) - \frac{3c_N}{2} \left(\frac{g_A m_\pi}{4\pi f_\pi} \right)^2 \\
&\quad - \frac{\hat{c}_N}{6} \left(\frac{g_A}{4\pi f_\pi} \right)^2 \left[m_\pi^2 + \frac{1}{\omega_a} \left(\frac{-\omega_a^3}{3} + m_\pi^3 F \left(\frac{-\omega_a}{m_\pi} \right) - m_\pi^3 F(0) \right) \right] \\
&\quad + 4m_\pi^2 \left[\left(\bar{d}_{16} \tau_3 - d_{17} \frac{1-z}{1+z} \right) c_{u-d} + \bar{d}_{16}^{u+d} c_{u+d} - (d_{18} + 2d_{19}) \frac{z}{(1+z)^2} \right],
\end{aligned} \tag{3.7}$$

and

$$\mathcal{B}^{(\nu=2)} = \frac{c_N}{4m_N^2} \left[2(\omega^2 - \omega_p^2) - (p + p_a)^2 + p^2 \right], \tag{3.8}$$

where we defined $\hat{c}_N = \tau^a c_N \tau^b \delta_{ab} = -g_A c_{u-d} \tau_3 + 3g_0 c_{u+d} \mathbb{1}$ and

$$F(x) = -(x^2 - 1 + i\varepsilon)^{3/2} \left[\log \left(x - \sqrt{x^2 - 1 + i\varepsilon} \right) - \log \left(x + \sqrt{x^2 - 1 + i\varepsilon} \right) \right], \tag{3.9}$$

see also App. C.2.

While the next order $\nu = 3$ is, of course, naively suppressed, it is well known that the low energy constants $\hat{c}_{3/4}$ from the NLO pion-nucleon Lagrangian, see Eq. (2.26a), are larger

⁴Our result is also valid for momenta above the pion mass and differs in the evaluation of one of the diagrams, see App. C.2.

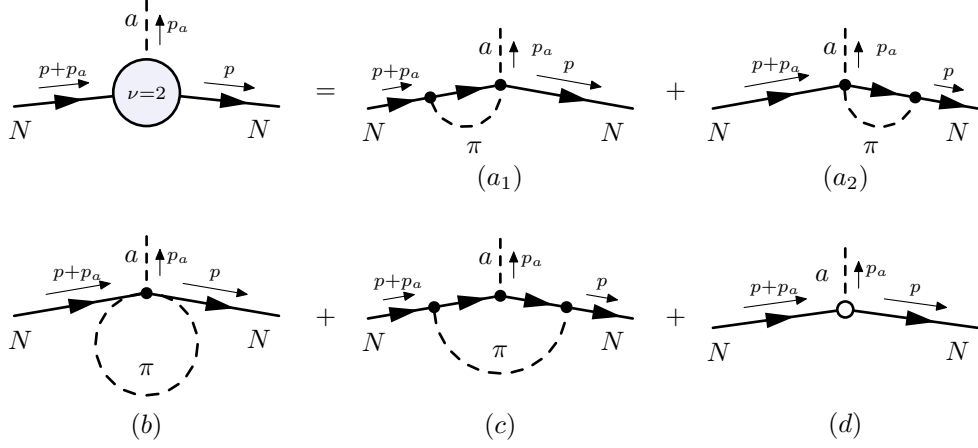


Figure 1: Corrections to the axion nucleon vertex at chiral order $\nu = 2$. Filled dots $(a_1), \dots, (c)$ denote $\Delta = 0$ vertices according to Eq. (2.25). The empty circle (d) denotes the tree-level contributions from $\hat{\mathcal{L}}_{\pi N}^{(3)}$, including terms needed to renormalize the previous diagrams and relativistic corrections, see [81].

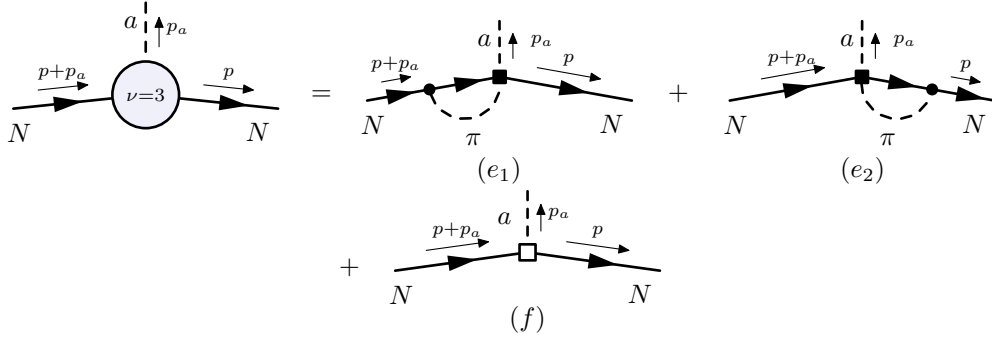


Figure 2: Corrections to the axion nucleon vertex at chiral order $\nu = 3$. Filled squares (e) denote $\Delta = 1$, filled circles denote $\Delta = 0$ vertices according to Eq. (2.25). The empty square (f) denotes tree-level contributions from $\hat{\mathcal{L}}_{\pi N}^{(4)}$, see Ref. [82], needed to renormalize the previous diagrams.

than the naive power counting expectation due to the low-lying $\Delta(1232)$ -resonance [33]. Note that while the coefficient \hat{c}_2 is also enhanced, its effects are kinematically suppressed and thus neglected. Including only the enhanced diagrams captures the dominant effects of the next order without calculating all diagrams at $\nu = 3$. In Fig. 2, we show the enhanced diagrams and the corresponding tree-level diagram necessary for their renormalization. Note that the analogous isoscalar diagrams, generated by \hat{c}_9 are not enhanced by the $\Delta(1232)$ -resonance and thus dropped. The result can be written in terms of a single form

factor

$$= -\frac{1}{f_a} \mathcal{A}^{(\nu=3)} S \cdot p_a, \quad (3.10)$$

with

$$\mathcal{A}^{(\nu=3)} = \frac{4g_A c_{u-d}}{3(4\pi f_\pi)^2} (\hat{c}_3 - 2\hat{c}_4) \tau^3 \left[m_\pi^2 \omega_a - \omega_a^3 - m_\pi^3 F\left(\frac{-\omega_a}{m_\pi}\right) - m_\pi^3 F(0) \right]. \quad (3.11)$$

To arrive at this result, we subtracted the piece

$$-\frac{2g_A}{3f_\pi^2} (\hat{c}_3 - 2\hat{c}_4) c_{u-d} \tau^3 \Lambda(\lambda) (6m_\pi^2 (\omega + \omega_p) - 4(\omega^3 + \omega_p^3)), \quad (3.12)$$

where $\Lambda(\lambda)$ collects the scale-dependent and divergent pieces in dimensional regularization. The isovector divergent parts are renormalized by the appropriate $\Delta = 3$ operators found in [82], and no finite pieces are generated. For details, see App. C.2.1.

Summarizing our findings, the result up to the relevant $\nu = 3$ contributions is given by

$$= -\frac{1}{f_a} \mathcal{A}^{(\nu \leq 3)} S \cdot p_a - \frac{1}{f_a} \mathcal{B}^{(\nu \leq 3)} S \cdot p$$

$$= -\left\{ \frac{c_N}{m_N} (\omega_p - \omega) + \frac{c_N}{4m_N^2} \left[2(\omega^2 - \omega_p^2) - ((p+p_a)^2 - p^2) \right] \right\} \frac{S \cdot p}{f_a}$$

$$- \left\{ c_N + \frac{c_N}{2m_N} (\omega_p - \omega) - \frac{c_N}{4m_N^2} (\omega_p^2 - \omega^2 + \omega_p \omega - p^2) - \frac{3c_N}{2} \left(\frac{g_A m_\pi}{4\pi f_\pi} \right)^2 \right. \quad (3.13)$$

$$- \frac{\hat{c}_N}{6} \left(\frac{g_A}{4\pi f_\pi} \right)^2 \left[m_\pi^2 + \frac{1}{\omega_a} \left(\frac{-\omega_a^3}{3} + m_\pi^3 F\left(\frac{-\omega_a}{m_\pi}\right) - m_\pi^3 F(0) \right) \right]$$

$$+ \frac{4g_A c_{u-d}}{3(4\pi f_\pi)^2} (\hat{c}_3 - 2\hat{c}_4) \tau^3 \left[m_\pi^2 \omega_a - \omega_a^3 - m_\pi^3 F\left(\frac{-\omega_a}{m_\pi}\right) - m_\pi^3 F(0) \right]$$

$$\left. + 4m_\pi^2 \left[\left(\bar{d}_{16} \tau_3 - d_{17} \frac{1-z}{1+z} \right) c_{u-d} + \bar{d}_{16}^{u+d} c_{u+d} - (d_{18} + 2d_{19}) \frac{z}{(1+z)^2} \right] \right\} \frac{S \cdot p_a}{f_a}.$$

The form factors are diagonal matrices in isospin space, and we define their components as

$$\mathcal{A}^{(\nu \leq 3)} = \text{Diag}(\mathcal{A}_{ap}, \mathcal{A}_{an}), \quad (3.14a)$$

$$\mathcal{B}^{(\nu \leq 3)} = \text{Diag}(\mathcal{B}_{ap}, \mathcal{B}_{an}). \quad (3.14b)$$

We want to stress at this point that it is important to make the correct choice of the (bare) Lagrangian constants such that our EFT predicts the measured coupling constants in the zero momentum limit. That is, as we go to chiral order $\nu = 3$, the constants have to be matched consistently at this order to the experimentally measured values.

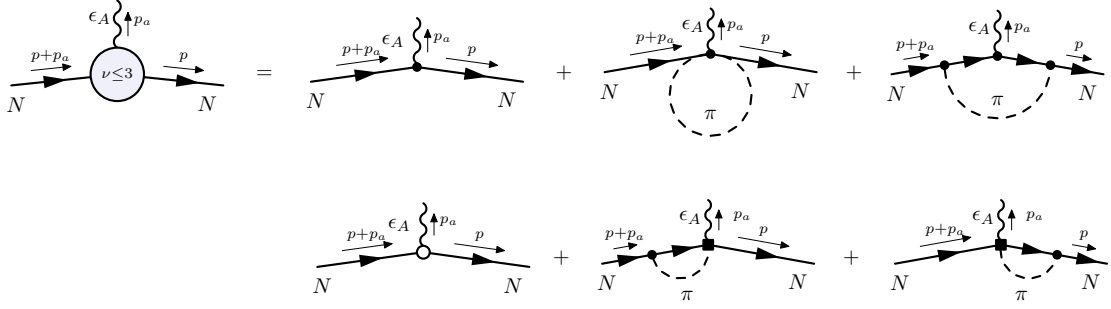


Figure 3: Diagrams contributing to the isovector form factor.

3.1.1 Consistent choice of Lagrangian parameters

We now determine the Lagrangian parameters consistently using experimental input. To do so, we calculate the matrix elements $\epsilon_A^\mu \langle N(p') | A_\mu^a | N(p) \rangle$ as well as $\epsilon_A^\mu \langle N(p') | A_\mu^s | N(p) \rangle$ to order $\nu = 3$, where A_μ^a and A_μ^s are isovector and isoscalar axial currents respectively while ϵ_A^μ are the corresponding polarization vectors for the isovector and isoscalar. The form factors $G_A(t)$ and $G_0(t)$ within HBChPT are related to the matrix elements by

$$\epsilon_A^\mu \langle N(p') | A_\mu^a | N(p) \rangle \supset G_A(t) \epsilon_A^\mu \bar{u}(p') \gamma_\mu \gamma_5 (\tau^a / 2) P_{v+} u(p), \quad (3.15a)$$

$$\epsilon_A^\mu \langle N(p') | A_\mu^s | N(p) \rangle \supset G_0(t) \epsilon_A^\mu \bar{u}(p') \gamma_\mu \gamma_5 (\mathbb{1} / 2) P_{v+} u(p), \quad (3.15b)$$

where P_{v+} is the projector onto the light baryon component, see App. A.3. In the limit $t = (p' - p)^2 \rightarrow 0$ these are fixed experimentally, from beta decay $G_A(0) \equiv G_A = 1.2754(13)$ [79], and the lattice $G_0(0) \equiv G_0 = 0.440(60)$ [80].

In order to calculate the matrix elements, we need to evaluate the diagrams shown in Figs. 3 and 4, and multiply each by two factors of the nucleon wave function renormalization $\sqrt{Z_N}$, one for each external leg, given by

$$Z_N = 1 + \Sigma'(0) = 1 - \frac{3g_A^2 m_\pi^2}{32\pi^2 f_\pi^2}, \quad (3.16)$$

where at $\nu = 3$, consistent with our calculation above, we dropped the terms that are not $\Delta(1232)$ -enhanced. The isovector axion form factor in the limit $t \rightarrow 0$ to this order is

Parameter	G_A [79]	G_0 [80]	M_N [79]	F_π [80]	M_π [79]
Value	1.2754(13)	0.440(60)	938.9(5) MeV	92.07(57) MeV	139.6(5) MeV

Table 1: Numerical values for the measured parameters. Note that we add the electromagnetic mass splitting as an error for the proton and pion mass and choose as the central value the average between charged and neutral masses for the nucleons, while for the pion, we choose the charged pion mass.

given by [83, 84]

$$G_A = g_A - \frac{g_A^3 m_\pi^2}{16\pi^2 f_\pi^2} + 4m_\pi^2 \bar{d}_{16} + \frac{g_A m_\pi^3}{6\pi f_\pi^2} (2\hat{c}_4 - \hat{c}_3), \quad (3.17)$$

while we find that the analogous result for G_0 at this order reads

$$G_0 = g_0 - \frac{3g_0 g_A^2 m_\pi^2}{16\pi^2 f_\pi^2} + 4m_\pi^2 \bar{d}_{16}^{u+d}. \quad (3.18)$$

A similar calculation at this order can be done for the pion mass and decay constant, as well as the nucleon mass, which up to small isospin-breaking corrections gives [33, 85]

$$M_\pi^2 = m_\pi^2 \left[1 - \frac{m_\pi^2}{32\pi^2 f_\pi^2} \bar{\ell}_3 \right], \quad (3.19)$$

$$F_\pi = f_\pi \left[1 + \frac{m_\pi^2}{16\pi^2 f_\pi^2} \bar{\ell}_4 \right], \quad (3.20)$$

$$M_N = m_N \left[1 - 4\hat{c}_1 \frac{m_\pi^2}{m_N} - \frac{3g_A^2 m_\pi^3}{32\pi f_\pi^2 m_N} \right]. \quad (3.21)$$

We denote physical parameters with capital letters, *i.e.* G_A, G_0, M_π, F_π and M_N summarized in Tab. 1, while Lagrangian (bare) quantities are referred to by lowercase letters and are summarized in Tab. 2. Clearly, they are different from the tree-level results shown in Sec. 2.4.

Since the isospin breaking effects to the nucleon masses cancel in the average, we use $2M_N = m_p + m_n$ (see Table 1) to match. On the other hand, we identify M_π with the mass of the charged pion, as the neutral pion gets an additional isospin-breaking contribution to the mass not included in Eq. (3.19). In this work, we neglect electromagnetic effects, which we account for by adding a ± 0.5 MeV uncertainty when identifying the above masses with their measured value. Note that up to isospin-breaking electromagnetic and tiny Yukawa corrections, the ratio of quark masses z is scale and scheme-independent.

In analogy to [81], we assume that the undetermined low-energy constants \bar{d}_{16}^{u+d} , d_{17} , and d_{19} are drawn from a superposition of two normal distributions with $d_i = \pm 0.5(5)$ GeV $^{-2}$. Note that while we assume a Gaussian error for all input parameters, the errors of derived quantities are strongly correlated. We can now discuss our predictions Eq. (3.13).

3.1.2 Results

Let us start with evaluating the axion coupling to protons and neutrons up to $\nu = 3$ in the limit of all external momenta $p_i \rightarrow 0$. As evident from Eq. (3.13) the analytic result

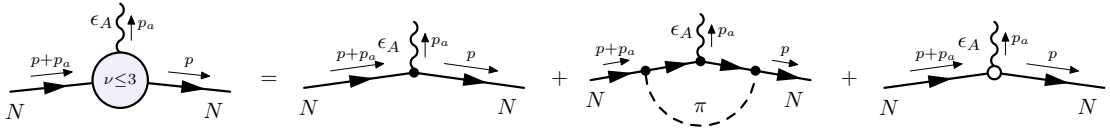


Figure 4: Diagrams contributing to the isoscalar form factor.

Lagrangian parameter	Value
g_A	1.23(11)
g_0	0.478(90)
m_N	870.8(36) MeV
f_π	85.52(77) MeV
m_π	141.7(75) MeV
z [79]	0.474(65)
$\bar{\ell}_3$ [80]	3.41(82)
$\bar{\ell}_4$ [80]	4.40(28)
ℓ_7 [25]	$7(4) \times 10^{-3}$
\bar{d}_{16} [86]	$-3.0(1.6) \text{ GeV}^{-2}$
d_{18} [87]	$-0.44(24) \text{ GeV}^{-2}$
\hat{c}_1 [87]	$-1.07(2) \text{ GeV}^{-1}$
\hat{c}_3 [87]	$-5.32(5) \text{ GeV}^{-1}$
\hat{c}_4 [87]	$3.56(3) \text{ GeV}^{-1}$
C_S [88]	$-119(7) \text{ GeV}^{-2}$

Table 2: Numerical values of the bare parameters. Note that the first ones are derived from the physical parameters in Tab. 1. For simplicity, we assumed that all errors in the input parameters are Gaussian around the central value. Note, however, that the errors in the derived quantities are strongly correlated.

consists of two form factors $\mathcal{A}^{(\nu \leq 3)}$ and $\mathcal{B}^{(\nu \leq 3)}$, however in this limit, the only surviving contribution comes from $\mathcal{A}^{(\nu \leq 3)}$. Here, our results necessarily agree with [25], as both EFTs are equally valid. All relevant Lagrangian parameters are summarized in Table 2.

The model-dependent result for the axion neutron and axion proton coupling is

$$\begin{aligned}
C_{ap} &\equiv \lim_{p_i \rightarrow 0} \mathcal{A}_{ap}^{(\nu \leq 3)} = -0.423(54) + 0.847(30)c_u^0 - 0.427(30)c_d^0, \\
C_{an} &\equiv \lim_{p_i \rightarrow 0} \mathcal{A}_{an}^{(\nu \leq 3)} = 0.020(54) - 0.427(30)c_u^0 + 0.847(30)c_d^0,
\end{aligned}
\tag{3.22}$$

where we choose the corresponding entries of the isospin matrix \mathcal{A} . This agrees with Eq. (2.31). However, here we included isospin-breaking effects, including the change in c_{u-d} due to NLO axion-pion mixing. The remaining numerical differences compared to [25] come from an updated choice for the central values of physical input parameters, *i.e.* mostly due to taking Δu and Δd from [80]. Note further that we do not take the strange quark as well as heavier quarks into account. Finally, for a KSVZ axion ($c_q^0 = 0$) we find

$$C_{ap}^{\text{KSVZ}} = -0.423(54), \quad C_{an}^{\text{KSVZ}} = 0.020(54),
\tag{3.23}$$

while for a DFSZ axion ($c_u^0 = \sin^2 \beta/3$, $c_d^0 = 1 - c_u^0$), we obtain

$$\begin{aligned}
C_{ap}^{\text{DFSZ}} &= -0.565(50) + 0.425(7) \sin^2 \beta, \\
C_{an}^{\text{DFSZ}} &= 0.300(50) - 0.425(7) \sin^2 \beta.
\end{aligned}
\tag{3.24}$$

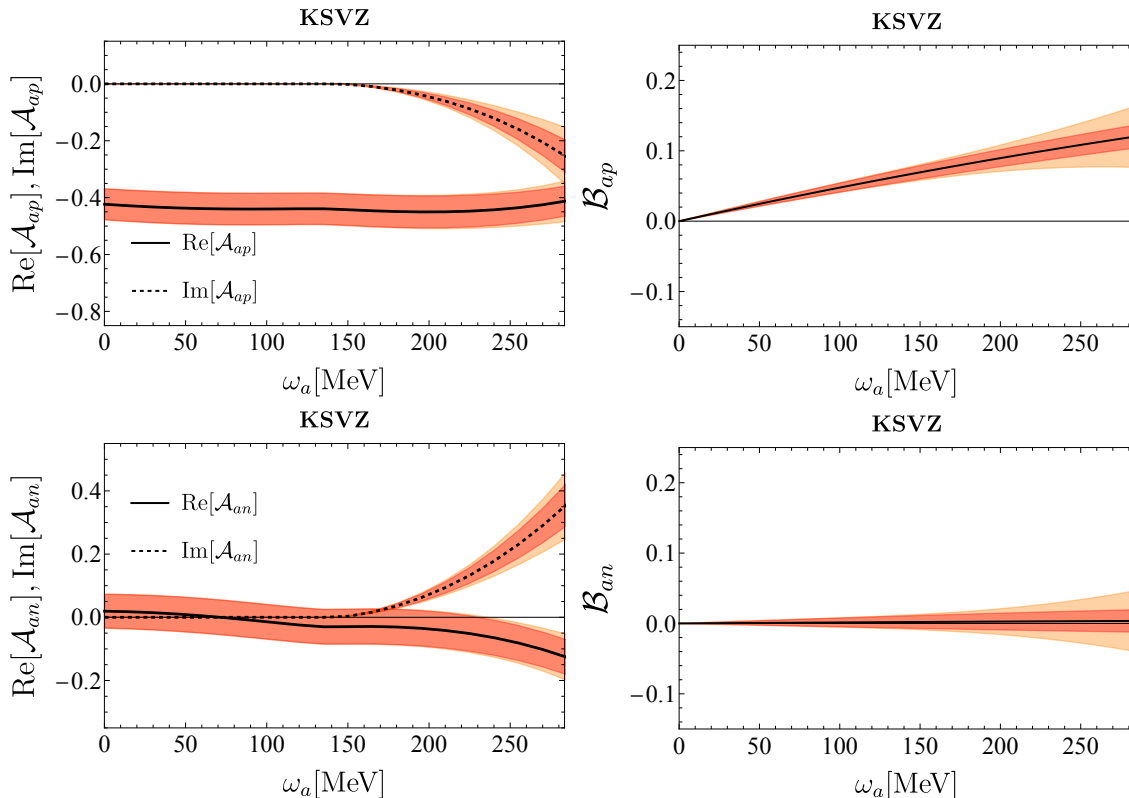


Figure 5: Dependence of the KSVZ axion-nucleon couplings on the axion energy $\omega_a = v \cdot p_a$. The red-shaded region represents the error bars resulting from the uncertainties of the constants given in Table 2, the orange-shaded region represents the estimated error emerging from the truncation of the chiral expansion. At $\omega_a \sim m_\pi$ one can see the pion production threshold, at which the coupling gets an imaginary part that becomes the dominant contribution at large energies. Note that since \mathcal{B} does not include loop corrections, hence there is no imaginary part.

While the calculation for the $\nu = 2$ correction closely resembles [81], the interpretation of our results differ; we determine the Lagrangian parameters from experiment at the order of our perturbative expansion, thereby ensuring we reproduce the results of [25] in the limit of small momentum. This ensures that there is no additional uncertainty due to the truncation of the ChPT expansion at zero momentum. More importantly, our main result is the non-trivial momentum dependence of the axion coupling in Eq. (3.13).

For non-negligible axion momenta both form factors $\mathcal{A}^{(\nu \leq 3)}$ and $\mathcal{B}^{(\nu \leq 3)}$ contribute. We show our full results in the rest frame of the outgoing nucleon, $p = 0$, for a KSVZ axion in Fig. 5 plotted against the axion energy ω_a . Note that we keep the outgoing axion and outgoing nucleon momenta on-shell.

Due to the $\Delta(1232)$ -resonance enhancement, the $\nu = 3$ diagrams are numerically more important than the $\nu = 2$ corrections. These higher-order diagrams also lead to more substantial modifications than those from the strange quark, as detailed in [89].

We address the uncertainties associated with truncating the chiral expansion by including an error in orange. We estimate the size of this neglected contribution by taking the $\nu = 3$ result and multiplying it by an additional factor of $\omega_a/(4\pi f_\pi)$.

In addition, we can determine the momentum dependence of an ALP, *i.e.* an axion without QCD anomaly, from Eq. (3.13); one first needs to drop terms that are not $\propto c_{u+d}$ or $\propto c_{u-d}$, which amounts to dropping terms $\propto d_{18}, d_{19}$. Further, the contributions to c_{u+d} and c_{u-d} only arise in the UV, and thus $c_{u\pm d} = (c_u^0 \pm c_d^0)/2$.

In summary, our findings show a distinct momentum dependence of the axion-nucleon coupling at higher orders in the chiral expansion, which is relevant for phenomenological applications as discussed in Sec. 4.

3.2 Axion-nucleon couplings at finite density

In the following, we systematically calculate the leading order corrections to the axion-nucleon coupling induced by a background nucleon density. Within the real-time formalism of thermal field theory, the effects of finite nucleon densities are captured by the nucleon propagator, which is extended by a term depending on the nucleon chemical potential μ and the temperature T [90–92]. For a detailed discussion, we refer to App. B and the associated references. Note that an initial estimate for the effective finite density modification of the axion-nucleon coupling has already been performed in [27]. Recently, these results have been used to show that density corrections do not spoil suppressed axion-nucleon couplings in tuned models [93].

In the non-relativistic limit, as $T \rightarrow 0$, the finite density nucleon propagator in HBChPT takes the following form:

$$iG(k) = \frac{i}{v \cdot k + i\epsilon} - 2\pi\delta(v \cdot k) \left[\frac{1 + \tau^3}{2} \theta(k_f^p - |\vec{k}|) + \frac{1 - \tau^3}{2} \theta(k_f^n - |\vec{k}|) \right], \quad (3.25)$$

where k^μ is the residual momentum as defined in Eq. (2.22). Here

$$k_f^p \equiv (3\pi^2 n_p)^{1/3} \quad \text{and} \quad k_f^n \equiv (3\pi^2 n_n)^{1/3} \quad (3.26)$$

are the proton and neutron Fermi momenta and n_n and n_p denote their respective number densities. Note that the propagator modification due to density dependence in the $T \rightarrow 0$ limit can also be derived without using thermal field theory, see App. A in Ref. [94].

The axion nucleon form factor at finite density is calculated, similarly to before, by evaluating loop diagrams using the above propagator. In fact, the first term of Eq. (3.25) is the zero density heavy baryon propagator, which, if chosen for every internal nucleon line, leads to the vacuum corrections of the coupling calculated in the previous section. The second term of the propagator accounts for the interaction of the nucleon with the background and is referred to as medium- or density-insertion. Diagrammatically Eq. (3.25) reads

$$iG(k) = \begin{array}{c} \text{---} \text{---} \text{---} \text{---} \text{---} \text{---} \\ \text{N} \quad \blacktriangleright \quad \text{N} \end{array} + \begin{array}{c} \text{---} \text{---} \text{---} \text{---} \text{---} \text{---} \\ \text{N} \quad \# \quad \text{N} \end{array}, \quad (3.27)$$

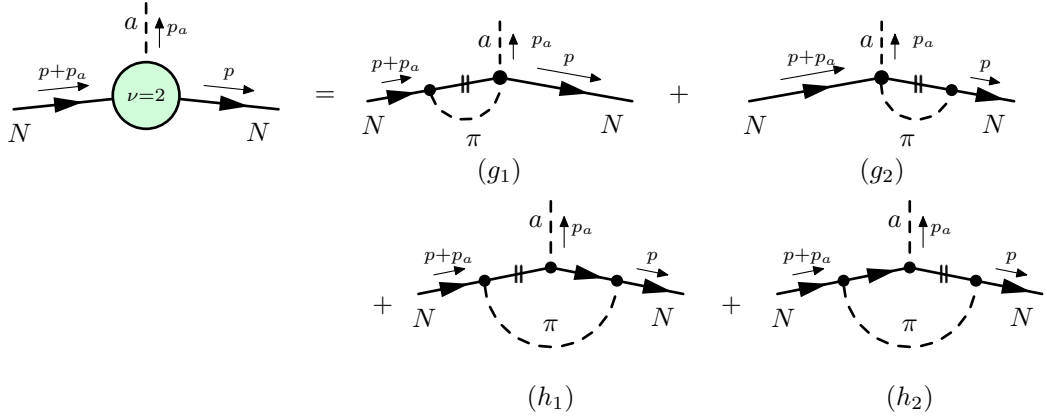


Figure 6: Corrections to the axion nucleon vertex at finite density at chiral order $\nu = 2$. Filled dots denote $\Delta = 0$ vertices according to Eq. (2.25). Two lines on the nucleon propagator mean that the vacuum nucleon propagator has been replaced by the density insertion.

where we follow the convention to denote the density insertion by the short double-stroke. In the isospin symmetric case, where $n/2 \equiv n_n = n_p$ with $k_f = (3\pi^2 n/2)^{1/3}$, Eq. (3.25) simplifies to

$$iG(k) = \frac{i}{v \cdot k + i\epsilon} - 2\pi\delta(v \cdot k)\theta(k_f - |\vec{k}|). \quad (3.28)$$

In the following we discuss the vertex corrections to the axion-nucleon coupling that arise due to the medium insertion.

3.2.1 Axion-nucleon vertex corrections

Density effects start to contribute at chiral order $\nu = 2$. As in the previous section we show diagrams that are non-zero in Fig. 6, while the explicit calculation is performed in App. C.3. Using the expressions defined in App. C.1.2, the full result at this order reads

$$\begin{aligned}
& \text{Diagram (Fig. 6): } \nu=2 \text{ vertex} \\
& = - \left(\frac{g_A^2 c_p}{f_a f_\pi^2} \right) (3 \mathbb{1} - \tau^3) G_1^p(\vec{p}, \vec{p}_a) + \left(\frac{c_{u-d} g_A}{f_a f_\pi^2} \right) (\mathbb{1} - \tau^3) G_2^p(\vec{p}, \vec{p}_a) \\
& \quad - \left(\frac{g_A^2 c_n}{f_a f_\pi^2} \right) (3 \mathbb{1} + \tau^3) G_1^n(\vec{p}, \vec{p}_a) - \left(\frac{c_{u-d} g_A}{f_a f_\pi^2} \right) (\mathbb{1} + \tau^3) G_2^n(\vec{p}, \vec{p}_a),
\end{aligned} \quad (3.29)$$

where $c_{n/p}$ are defined in Eq. (3.2), and $\tilde{m}_\pi^2 = m_\pi^2 - (p_a^0)^2$.

At the next higher order, *i.e.* $\nu = 3$, we again restrict ourselves to the diagrams proportional to the $\Delta(1232)$ -enhanced coupling constants $\hat{c}_{3/4}$. The corresponding diagrams are shown in figure Fig. 7. Following the computation in C.3, we find

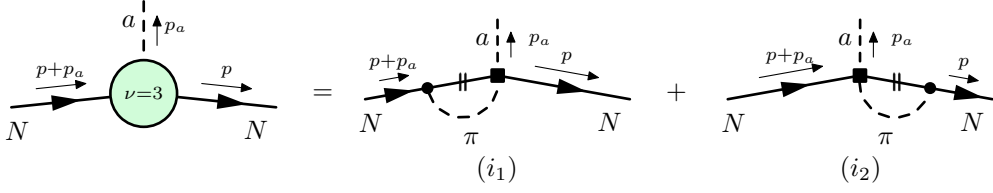
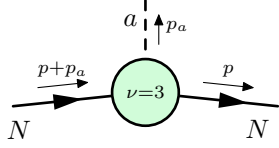


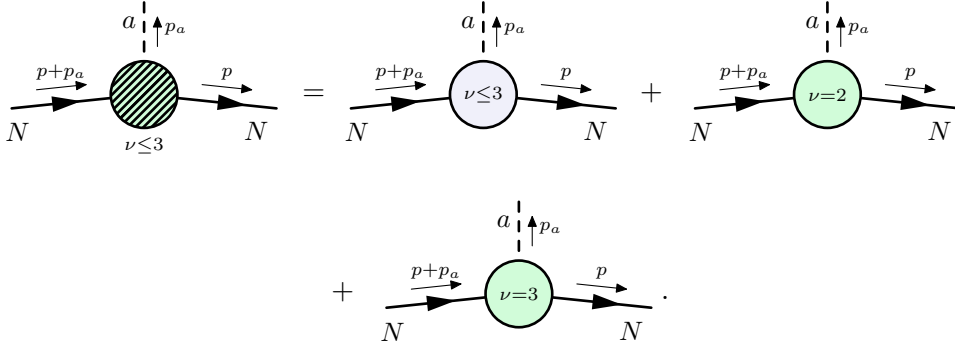
Figure 7: Dominant (*i.e.* Δ -enhanced) corrections to the axion nucleon vertex at finite density at chiral order $\nu = 3$. Filled squares denote $\Delta = 1$, filled circles denote $\Delta = 0$ vertices according to Eq. (2.25).



(3.30)

$$\begin{aligned}
&= \left(\frac{\hat{c}_4 c_u - d g_A}{f_a f_\pi^2} \right) (\tau^3 - \mathbb{1}) G_3^p(\vec{p}, \vec{p}_a) + \left(\frac{\hat{c}_3 c_u - d g_A}{f_a f_\pi^2} \right) (\tau^3 + \mathbb{1}) G_4^p(\vec{p}, \vec{p}_a) \\
&+ \left(\frac{\hat{c}_4 c_u - d g_A}{f_a f_\pi^2} \right) (\tau^3 + \mathbb{1}) G_3^n(\vec{p}, \vec{p}_a) + \left(\frac{\hat{c}_3 c_u - d g_A}{f_a f_\pi^2} \right) (\tau^3 - \mathbb{1}) G_4^n(\vec{p}, \vec{p}_a).
\end{aligned}$$

The full result for the axion-nucleon vertex at finite density is then given by summing vacuum and density contributions denoted by gray and green blobs, respectively,



(3.31)

In order to gain some intuition of the parametric dependence of these expressions, we take a simplifying limit of Eq. (3.29) and Eq. (3.30), namely $|\vec{p}| \rightarrow k_f$, $k_f^n = k_f^p = k_f$, $m_\pi/k_f \rightarrow 0$ and keep only the leading order in p_a^0 . The result then simplifies to

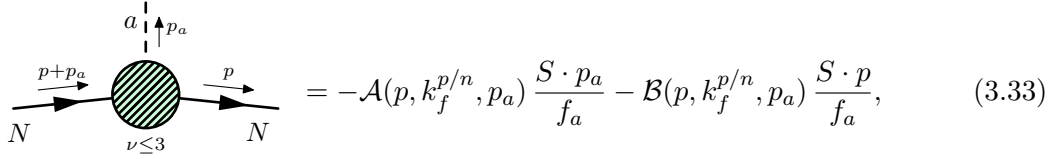
$$\begin{aligned}
&= - \left(- \frac{g_A^2 \hat{c}_N}{9} \frac{k_f^2}{(4\pi f_\pi)^2} + \frac{16 g_A c_u - d \tau^3}{9} \frac{k_f^3 (\hat{c}_3 - 5 \hat{c}_4)}{(4\pi f_\pi)^2} \right) \frac{S \cdot p_a}{f_a} \\
&- \left(- \frac{g_A (17 g_A \hat{c}_N + 108 c_u - d \tau^3)}{27} \frac{k_f p_a^0}{(4\pi f_\pi)^2} + \frac{16 g_A c_u - d \tau^3}{9} \frac{k_f^2 p_a^0 (\hat{c}_3 + \hat{c}_4)}{(4\pi f_\pi)^2} \right) \frac{S \cdot p}{f_a} + \dots \quad (3.32)
\end{aligned}$$

Except for very low densities, $n \ll n_0$, this simplified expression describes the result shown in Fig. 8 quite well.

In the limit where tensor-like terms are neglected, $(\vec{k} \cdot \vec{\sigma}) \vec{k} \sim 1/3 k^2 \vec{\sigma}$, the result includes the terms of the chiral two-body current calculations in heavy nuclei, see [54, 55]. However, in Eq. (3.32) there are additional terms that in the formalism of [54, 55] arise from solving the Lippmann-Schwinger equation. Note also that we only keep terms consistent with our power counting, *i.e.* we neglect terms $\propto \hat{c}_D$, relativistic corrections and terms that are kinematically suppressed.

3.2.2 Results

Finally, in analogy to Eq. (3.13), we collect our results in terms of form factors, now including density effects, as



$$\begin{array}{c}
 \begin{array}{ccc}
 \xrightarrow{p+p_a} & \begin{array}{c} a \\ \uparrow p_a \\ \bullet \\ \nu \leq 3 \end{array} & \xrightarrow{p} \\
 N & & N
 \end{array}
 \end{array}
 = -\mathcal{A}(p, k_f^{p/n}, p_a) \frac{S \cdot p_a}{f_a} - \mathcal{B}(p, k_f^{p/n}, p_a) \frac{S \cdot p}{f_a}, \quad (3.33)$$

where the density dependent form factors \mathcal{A} and \mathcal{B} are again diagonal matrices in isospin space in analogy to Eq. (3.14). In order to compare the two contributions it is useful to rescale the second form factor to $\mathcal{B}|\vec{p}|/|\vec{p}_a|$, since to leading order $\mathcal{B} \sim p_a$. In this case, they multiply a spin structure of similar size, *i.e.*

$$|\vec{p}_a| \left(\mathcal{A} S \cdot \hat{p}_a + \frac{|\vec{p}|}{|\vec{p}_a|} \mathcal{B} S \cdot \hat{p} \right). \quad (3.34)$$

We proceed by making motivated kinematic approximations in order to plot the above results. At low temperatures, nucleons are expected to have momenta close to the Fermi momentum $|\vec{p}| \sim k_f$. Furthermore, the momentum of the axion is small compared to the momenta of the nucleons, *i.e.* $|\vec{p}_a| \ll k_f \sim p$, and we only keep the leading order which is independent of $|\vec{p}_a|$. Additionally, we average over the direction of the outgoing axion $\vec{p}_a \cdot \vec{p} \sim k_f |\vec{p}_a|/3$.

Note that typically \mathcal{B} is dominated by the vacuum contribution, while \mathcal{A} is dominated by $\nu = 3$ density loops. The vacuum contribution to \mathcal{B} is $\propto p_a$, which after rescaling results in $\mathcal{B} \propto n^{1/3}$, as shown in the right panels of Figs. 8 and 10.

Let us estimate the error coming from truncating the ChPT expansion. The first $\Delta(1232)$ -enhanced diagrams appear at chiral order $\nu = 3$, and we expect that higher order terms can be enhanced as well. We can estimate them, assuming that the next order has a similar numerical prefactor as the calculated diagrams but is suppressed by an additional factor of k_f/m_N (or similarly k_f/Λ_χ). As in Sec. 3.1.2, we add an uncertainty to the result, which we take to be the $\nu = 3$ result multiplied by the above suppression factor.

In the following, we show the density dependence of the axion-nucleon coupling, based on the systematic calculations within the validity of the ChPT expansion from the previous sections, for two benchmark models, the KSVZ and the DFSZ axion.

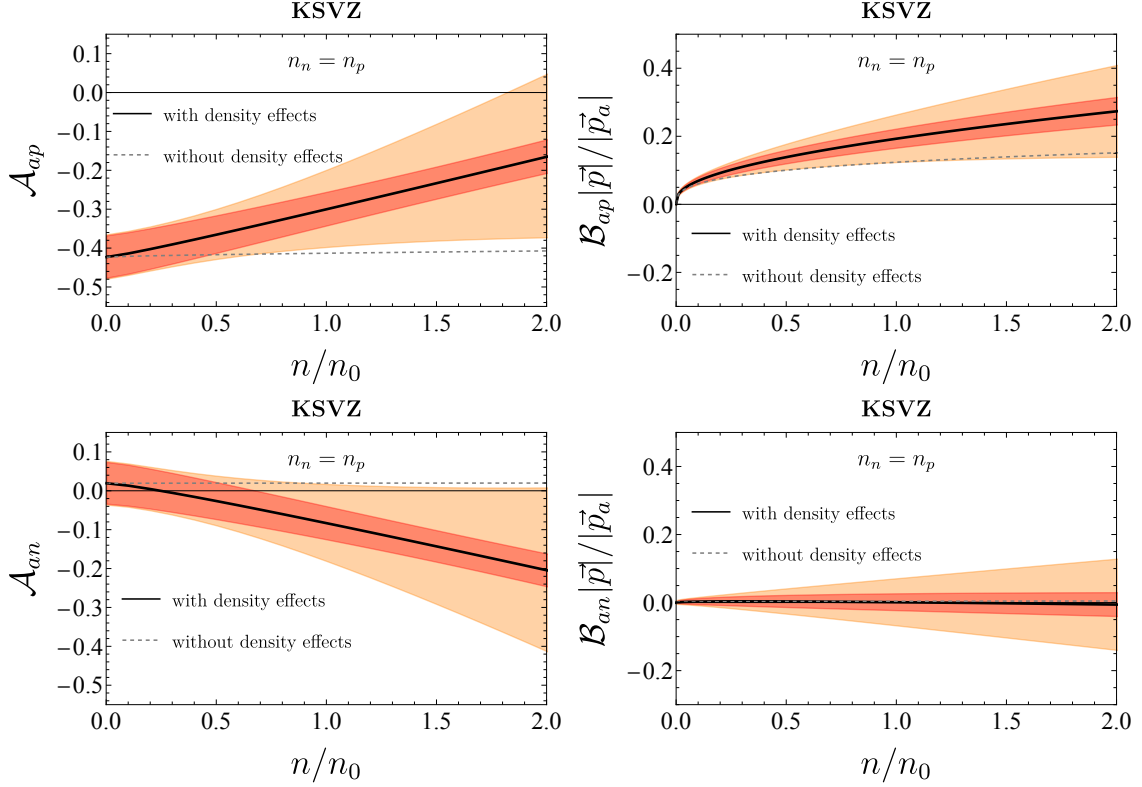


Figure 8: Density dependence of the KSVZ axion-nucleon couplings in isospin symmetric nuclear matter as a function of number density in units of nuclear saturation density n_0 . Error bars are shown as in Fig. 5. The gray dashed line shows the vacuum results, see Eq. (3.33), *i.e.* it neglects all density effects and only shows the effects of the momentum dependence evaluated at the corresponding Fermi momentum.

KSVZ axion

For the KSVZ axion, ($c_q^0 = 0$), we find that the density corrections are crucial: the accidental cancellation in the axion neutron coupling, Eq. (2.31), is eliminated by finite density effects. We show our results of the axion-nucleon coupling in isospin symmetric matter, ($n_p = n_n = n/2$), in Fig. 8. Around nuclear saturation density $n = n_0 \simeq 0.16 \text{ fm}^{-3}$ to leading order in p_a , we find

$$\mathcal{A}_{ap}^{\text{KSVZ}}(n_0) = -0.299(43)(98), \quad \frac{|\vec{p}|}{|\vec{p}_a|} \mathcal{B}_{ap}^{\text{KSVZ}}(n_0) = +0.193(28)(70), \quad (3.35a)$$

$$\mathcal{A}_{an}^{\text{KSVZ}}(n_0) = -0.083(43)(98), \quad \frac{|\vec{p}|}{|\vec{p}_a|} \mathcal{B}_{an}^{\text{KSVZ}}(n_0) = 0.001(25)(69), \quad (3.35b)$$

where the first error is due to the uncertainty of the low energy constants, while the second error is the total error estimate, including both the uncertainty of the ChPT expansion as well as the uncertainty of low energy constants. In Fig. 9, we show the results for pure neutron matter ($n_p = 0$ and $n_n = n$). At nuclear saturation density, we find the

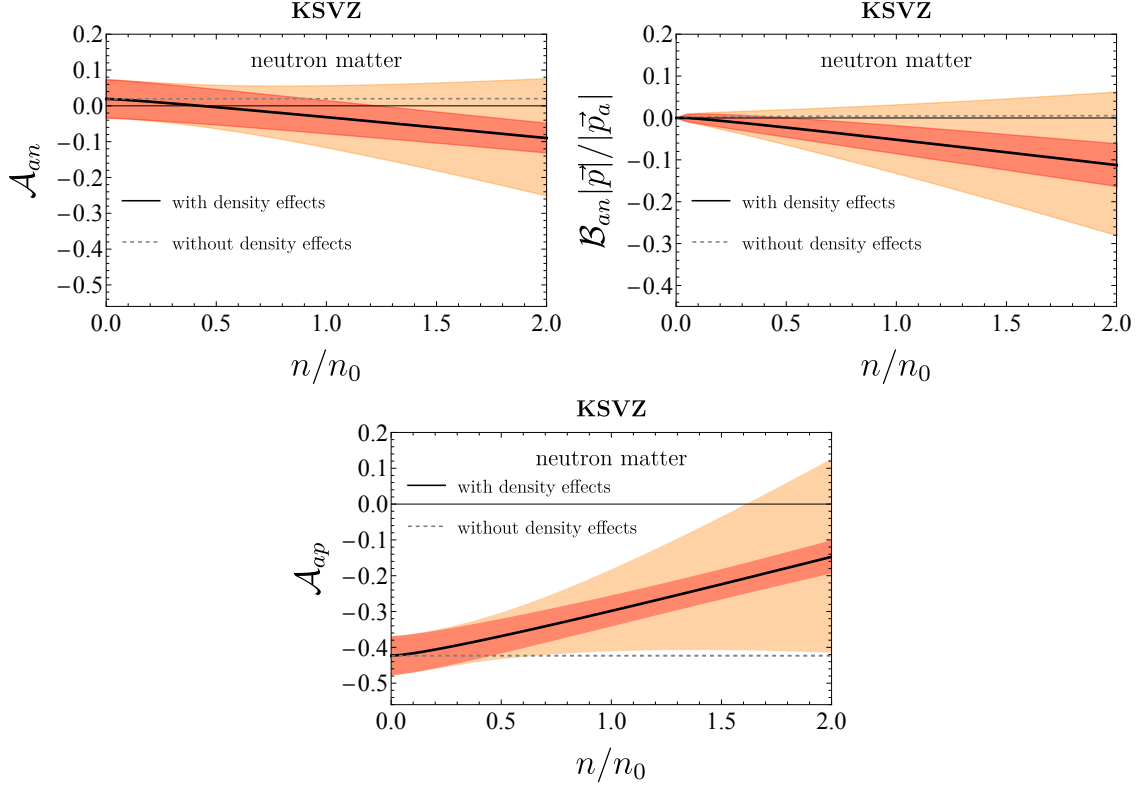


Figure 9: Density dependence of the KSVZ axion-nucleon couplings in pure neutron matter as a function of density in units of nuclear saturation density n_0 . Error bars are shown as in Fig. 5. Note that for pure neutron matter, the vacuum contribution to \mathcal{B}_{an} is small (see Eq. (3.13)), and the dominant contribution comes from the $\nu = 3$ density diagram $\propto \hat{c}_3$. Therefore, we do not find the $\propto n^{1/3}$, but instead a $\propto n$ scaling. The gray dashed line shows the vacuum results (see Eq. (3.33)). Note that \mathcal{B}_{ap} is zero in the limit of $|\vec{p}| \sim k_f^p \sim 0$ and therefore suppressed.

axion-nucleon couplings for pure neutron matter to be

$$\mathcal{A}_{an}^{\text{KSVZ}}(n_0) = -0.031(47)(86), \quad \frac{|\vec{p}|}{|\vec{p}_a|} \mathcal{B}_{an}^{\text{KSVZ}}(n_0) = -0.051(33)(82), \quad (3.36)$$

$$\mathcal{A}_{ap}^{\text{KSVZ}}(n_0) = -0.298(43)(115). \quad (3.37)$$

At large densities, the dominant error comes from truncation of the ChPT series, while at low densities, it comes from uncertainties in the low energy constants.

Note that the coupling to a proton in pure neutron matter is similarly modified by $\mathcal{O}(1)$ as shown in Fig. 9. This is because the neutron density alone can modify the proton vertex by contributing as an internal line to the density loop. Hence in a small proton but large neutron density, corrections to the proton vertex are important as well.

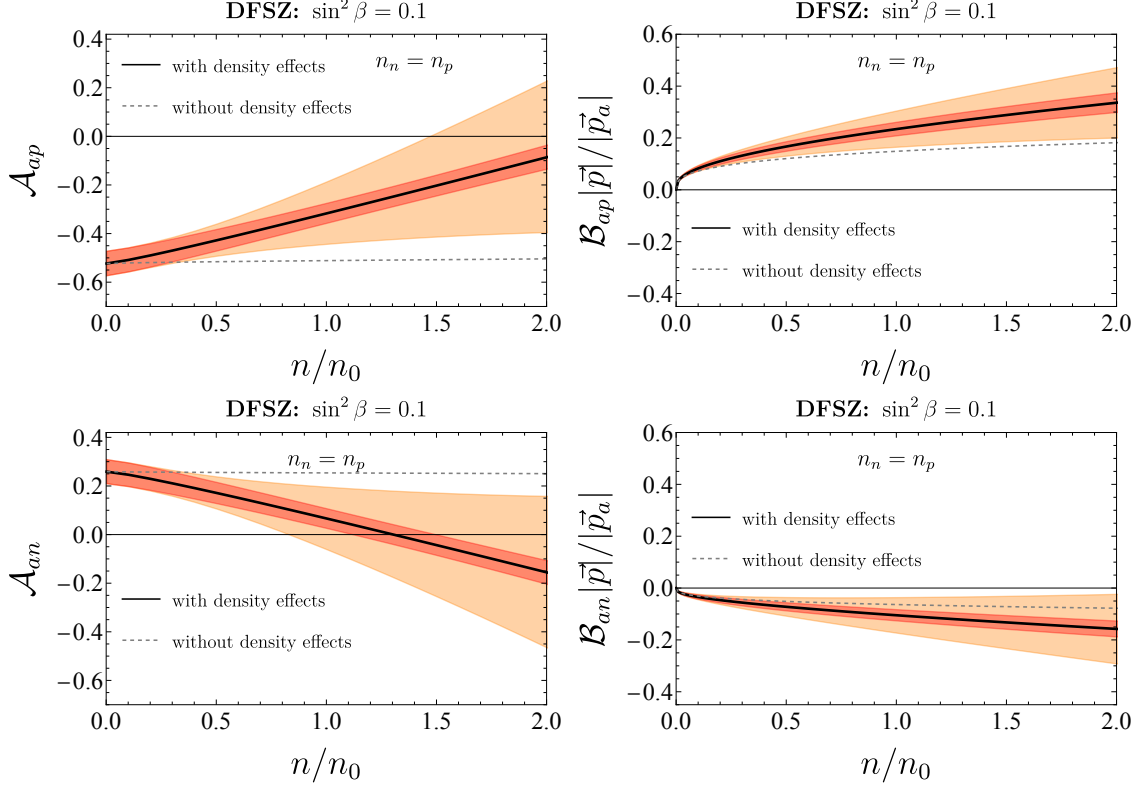


Figure 10: Density dependence of the DFSZ axion-nucleon couplings with $\sin^2 \beta = 0.1$ in symmetric nuclear matter as a function of density in units of nuclear saturation density n_0 . Error bars are shown as in Fig. 5. The gray dashed line shows the vacuum results (see Eq. (3.33)).

DFSZ axion

Next, we consider the DFSZ axion model with $c_u^0 = \sin^2 \beta / 3$, $c_d^0 = 1 - c_u^0$, where β is a parameter in the IR theory that is related to the vacuum expectation values of the two Higgs fields in the UV theory. Here, we find $\mathcal{O}(1)$ changes in the couplings, which we show a benchmark point $\sin^2 \beta = 0.1$ for symmetric nuclear matter in Fig. 10. In isospin symmetric matter, at nuclear saturation density, the axion-nucleon couplings \mathcal{A} with error estimates are given by

$$\mathcal{A}_{ap}^{\text{DFSZ}}(n_0) = -0.339(43)(98) + 0.208(22)(62) \sin^2 \beta, \quad (3.38a)$$

$$\mathcal{A}_{an}^{\text{DFSZ}}(n_0) = -0.087(43)(98) - 0.208(22)(62) \sin^2 \beta, \quad (3.38b)$$

while we find the coupling \mathcal{B} to be

$$\frac{|\vec{p}|}{|\vec{p}_a|} \mathcal{B}_{ap}^{\text{DFSZ}}(n_0) = +0.253(27)(70) - 0.184(13)(60) \sin^2 \beta, \quad (3.39a)$$

$$\frac{|\vec{p}|}{|\vec{p}_a|} \mathcal{B}_{an}^{\text{DFSZ}}(n_0) = -0.123(22)(68) + 0.184(13)(60) \sin^2 \beta. \quad (3.39b)$$

We show the results for another benchmark point, $\sin^2 \beta = 0.5$, as well as both benchmark points in pure neutron matter in App. C.4.

4 Implications of density and momentum dependent couplings

We now investigate the influence of our results on two of the strongest bounds on QCD axions: supernova and neutron star cooling bounds. We then comment on how these effects also influence terrestrial experiments seeking to detect a QCD axion as well as an ALP coupling to nucleons.

4.1 Supernova cooling bound

The observed neutrinos during SN 1987A [95, 96] impose stringent upper limits on axion couplings, as axions escaping the SN would affect the neutrino burst [97]. These limits are among the leading constraints on the axion-nucleon coupling and, thus, the axion decay constant. In this work, we are only considering the case of free streaming axions and are not interested in the trapping regime. The dominant contribution to the axion luminosity comes from the LO tree-level one-pion-exchange (OPE) diagram, shown in the left panel of Fig. 12, and was first calculated in [11, 12]. In addition to the LO contribution, several partial corrections have recently been included in a phenomenological manner, see *e.g.* [23, 24]. However, an evaluation using a systematic expansion, including an estimation of the errors of the axion emissivity, is still missing.

For a systematic treatment of the process $NN \rightarrow NNa$, it is crucial to consider all contributing diagrams up to a specified chiral order. Although the chiral expansion is formally valid for small momenta, in typical SN environments the expansion parameter is non-negligible, $p/\Lambda \sim 1/3$. In particular, if there are accidental cancelations in the LO result, higher-order contributions can be of similar size. For example, the NLO diagrams of type-(d), which are naively suppressed by $(p/\Lambda)^2$, are enhanced by an $\mathcal{O}(1)$ factor, such that they are only down by roughly 1/3 compared to the leading order result.

We categorize all diagrams contributing to $NN \rightarrow NNa$ into distinct classes, see Fig. 11. Here, the green dashed blob represents all possible one-particle-irreducible (1PI) structures up to the chosen chiral order, including vacuum and finite density corrections. For the nucleon-axion vertex, this blob was calculated in the previous sections.

Let us first investigate the matrix elements at leading order, *i.e.* $\nu = 0$. In this case, the diagrams (a)-(d) reduce to the standard OPE diagram. Diagrams (e)-(g) at leading level come from nucleon contact terms, and have two contributions, one from C_T and one from C_S , see Eq. (2.24). The contribution proportional to C_S vanishes identically due to a pairwise cancellation of diagrams with the axion attached at different external legs. The low energy constant C_T is numerically small and thus neglected. There are no diagrams contributing to (h)-(k) at leading order.

At chiral orders, $\nu \geq 1$, the picture is more complicated, and a full evaluation of the axion emissivity is left for future work. Here, we take into account some of the diagrams (type (a) and (e)), and comment on some of the effects that will become important for a full evaluation at $\nu \leq 3$.

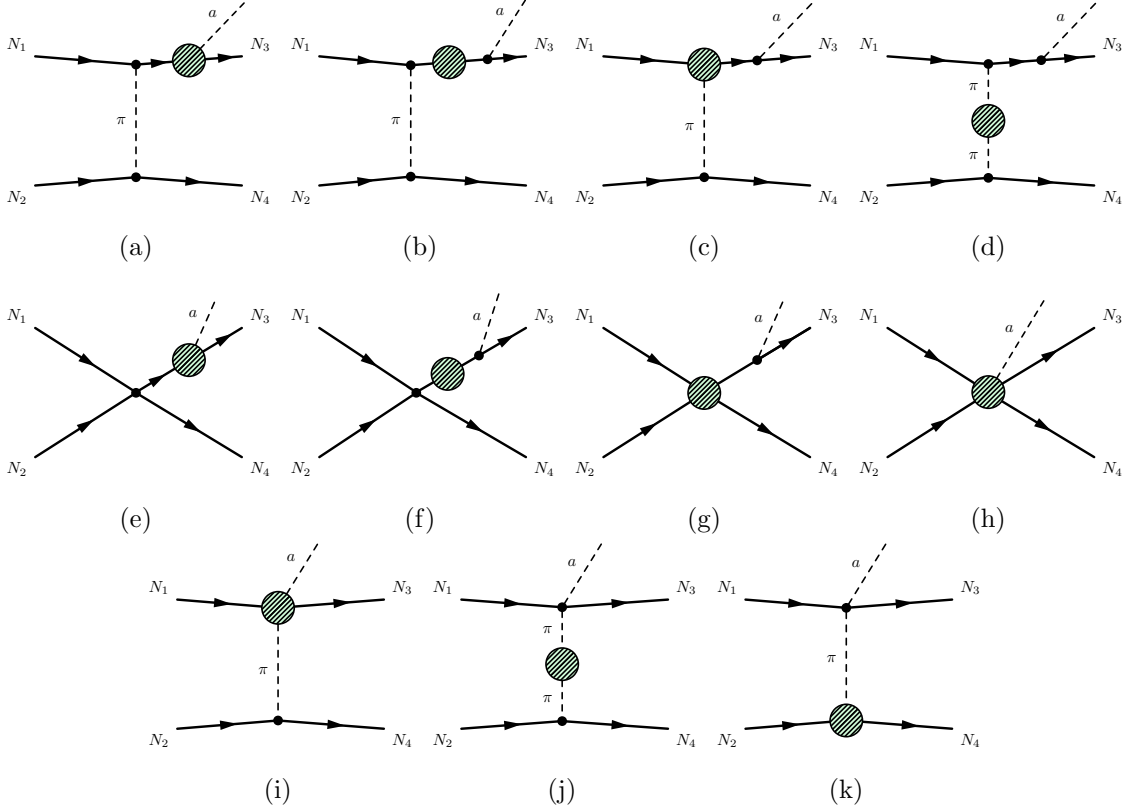


Figure 11: Classes of diagrams contributing to the axion emission. Green blobs represent 1PI diagrams. See text for details. We do not show mixed contributions from multiple lower-order blobs in a single diagram.

Diagrams of type (h)-(k) are suppressed by an additional power of $|\vec{p}_a|$, which in typical supernova environments is rather small compared to $|k_N|$ and of similar size as $\vec{k}_N^2/4\pi f_\pi$ corrections. The $\nu = 1$ diagrams of type (i) have been considered in [98], with the result confirming our expectation of this additional suppression.

Diagrams of type (c), (d), (g), which modify the nucleon-nucleon interaction at high momentum and density, have been considered, *e.g.*, in [99–102]. For the axion supernova bound, they have been modeled by an effective ρ -exchange [23] or taken into account as a ChPT-inspired correction factor [24]. These contributions seem to reduce the axion emissivity [99, 100, 103, 104] in the limit of $T \rightarrow 0$ and in the soft axion limit $\omega_a \rightarrow 0$. However, in supernova conditions high temperatures might spoil the suppression which we systematically explore in a forthcoming publication [105].

Diagrams of type (b) and (f) involve a resummed temperature and density-modified nucleon propagator. These corrections are interpreted as nucleon re-scatterings that can be sizable and have first been phenomenologically described in [106], and subsequently used, *e.g.*, in [10, 23, 24]. A systematic ChPT calculation of these contributions at finite density and temperature is still missing and is left for future work.

While we recognize the potential importance of all of these effects, our initial step

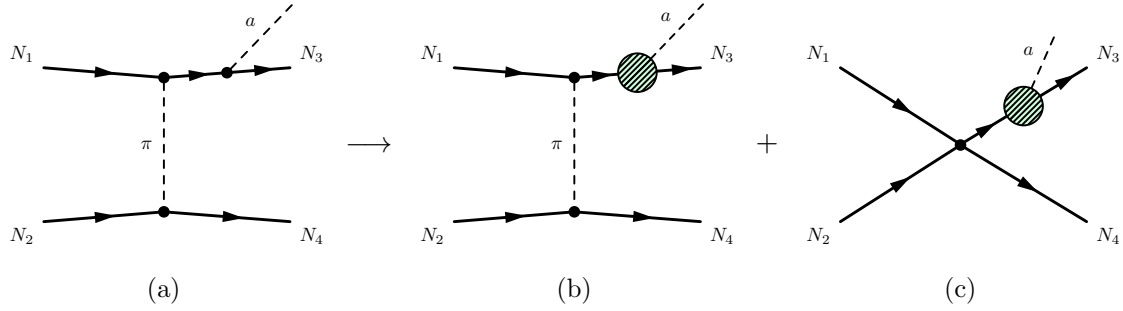


Figure 12: (a) Leading order OPE diagram. (b) OPE diagram with axion nucleon vertex corrections from finite and zero density. (c) Nucleon contact interaction with axion nucleon vertex corrections from finite and zero density.

towards a systematic calculation involves exclusively considering the effect that is separable into a change in the axion-nucleon coupling attached to a tree-level diagram, specifically types (a) and (e). One must remember that this approach comes at the cost of losing a systematic expansion. However, one can combine our results with contributions arising from other topologies.

For diagram (e), higher-order corrections introduce a non-trivial dependence on the external nucleon momenta. This lifts the cancellation that occurs at $\nu = 0$ and hence the correction proportional to C_S contributes $\mathcal{O}(1)$ to the $NN \rightarrow NNa$ process, while C_T remains numerically subdominant. Thus, when calculating the axion emissivity, we take into account the vertex-corrected OPE diagram as well as the vertex-corrected nucleon contact interaction, including all $\nu \leq 2$ and $\Delta(1232)$ -enhanced $\nu = 3$ corrections as shown in Fig. 12.

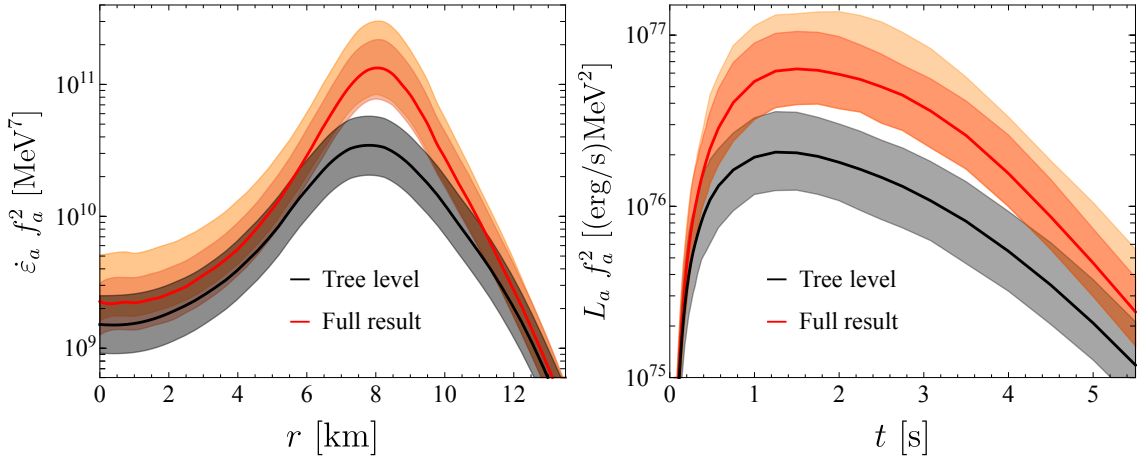


Figure 13: Left: Axion emissivity over radius for the KSVZ axion. Right: Axion luminosity over time integrated over the SN profile for the KSVZ axion. The shaded region represents the error bars resulting from the uncertainties of the constants given in, as well as the error emerging from higher-order terms in the chiral expansion.

The axion emissivity is given by

$$\dot{\epsilon}_a = \int \prod_{i=1}^4 d\Pi_i d\Pi_a (2\pi)^4 S |\mathcal{M}|^2 \delta^{(4)}(\sum_i p_i - p_a) E_a f_1 f_2 (1 - f_3) (1 - f_4), \quad (4.1)$$

which describes the amount of energy emitted by axions per volume and time. Here f_i denotes the Fermi-Dirac distribution of nucleon i and $d\Pi_i$ is the Lorentz invariant phase space measure. For details see App. B.4. The matrix element \mathcal{M} is the sum of the modified OPE and nucleon contact interaction diagrams, Fig. 12 (b) and (c).

To perform the integration explicitly, specific details about the supernova (SN) environment are required. For the numerical evaluation of the emissivity, we utilize data from SN simulations from the Garching group, which include contributions from muons as outlined here [107], based on [108]. Note that in the distribution functions f_i , we use the effective density-dependent nucleon mass provided by [107]. A similar density-dependent nucleon mass also arises within ChPT, see App. B.4. In the left panel of Fig. 13, we show the emissivity Eq. (4.1) for a KSVZ-type QCD axion evaluated at $t_{pb} = 1$ s post-bounce, (red) including axion-vertex corrections and (black) using only the leading order vacuum couplings.

The axion luminosity, *i.e.* the emitted energy by axions per time, is defined by the volume integral over the emissivity. When determining the luminosity observed by a distant observer from the supernova (SN), it is necessary to consider general-relativistic effects, as explained in Refs. [109, 110]. We adjust for the gravitational redshift experienced by axions as they are emitted from a radius r within the SN and travel to spatial infinity by multiplying with the lapse function squared provided by Ref. [107]. Additionally, the data of Ref. [107] is given in the comoving reference frame of the emitting medium. Thus, the radial velocity v_r of the SN causes another red- or blueshift due to the Doppler effect. In the limit of small radial velocity, this is accounted for by multiplying with a factor of $(1 + 2v_r)$ inside the volume integral. Hence, the axion luminosity is given by

$$L_a = \int dr 4\pi r^2 \dot{\epsilon}_a(r) (\text{lapse})^2 (1 + 2v_r). \quad (4.2)$$

In the right panel of Fig. 13, we show the luminosity for the KSVZ axion as a function of time including axion-vertex corrections (red), and compare to the leading order vacuum couplings (black). As can be seen, both the emissivity and the luminosity are enhanced by up to a factor of three, depending on radius and time, respectively. It is important to highlight that our calculations account for the uncertainties arising from the truncation of the ChPT expansion as well as from the low-energy constants, see Sec. 3.

In Fig. 14, we show the expectation value of the modified coupling of the axion to protons and neutrons as a function of the radius (lower four panels) for a given density and temperature profile (upper panel) taken from Ref. [107]. The expectation value is defined as

$$\langle \mathcal{A} \rangle \equiv \mathcal{N} \int \prod_{i=1}^4 d\Pi_i d\Pi_a \mathcal{A}(p, k_f^{p/n}, p_a) \delta^{(4)}(\sum_i p_i - p_a) f_1 f_2 (1 - f_3) (1 - f_4), \quad (4.3)$$

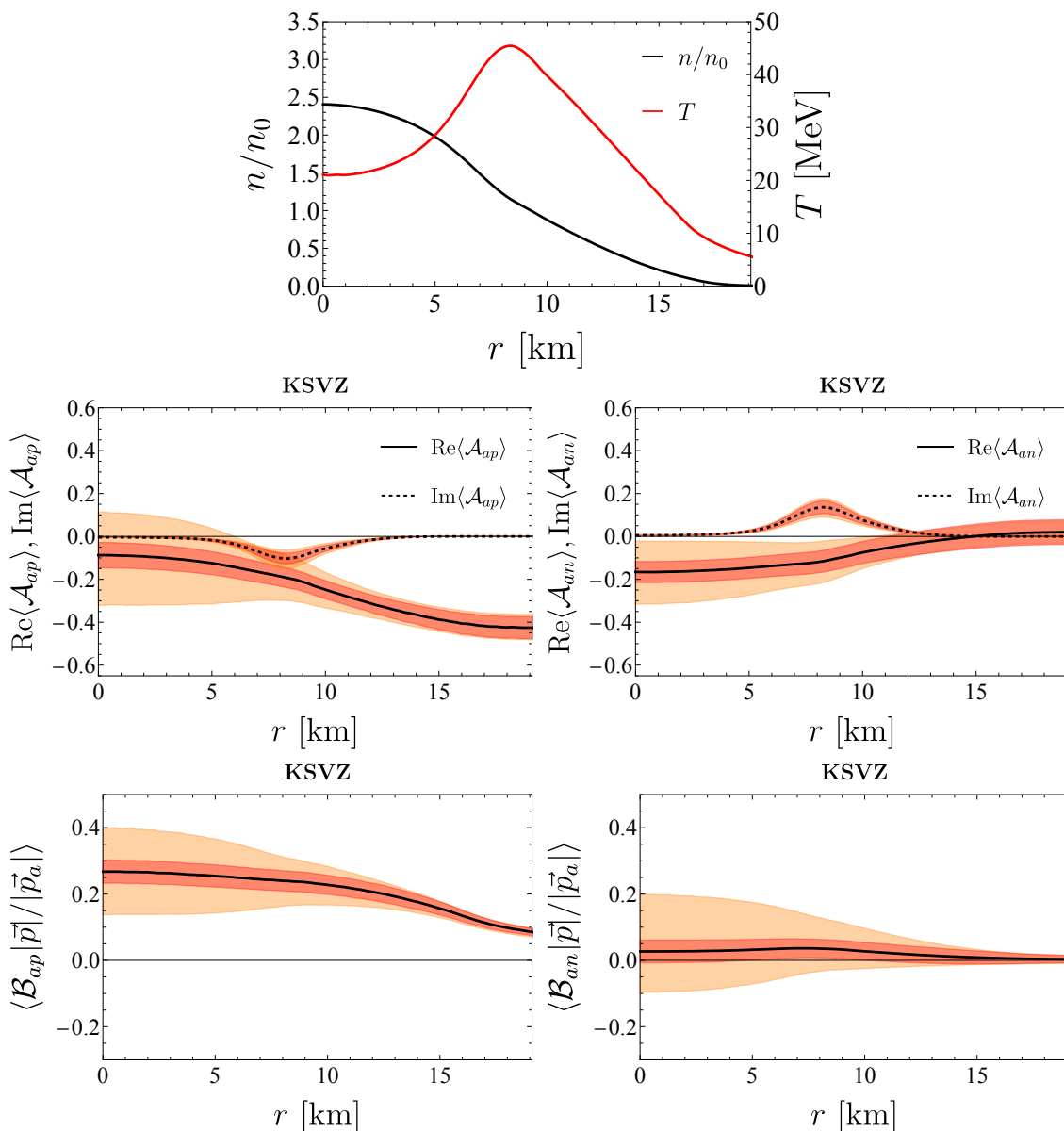


Figure 14: Top: Density and temperature profile taken from a SN simulation of [107] at $t_{pb} = 1$ s. Middle: Effective form factors \mathcal{A} of the KSVZ axion evaluated at typical momenta dictated by a SN profile at $t_{pb} = 1$ s taken from simulations of [107]. The red-shaded region represents the error bars resulting from the uncertainties of the constants given in Table 2, while the orange-shaded region represents the error emerging from higher-order terms in the chiral expansion. Note that the values of the real part of the couplings for large radii slightly deviate from the vacuum value in Eq. (3.23) because $T \neq 0$. Bottom: Analogous results for the form factor \mathcal{B} .

where \mathcal{N} is a normalization constant, and for simplicity we choose $p = p_1$. As can be seen, also temperature effects strongly modify the effective coupling, see also App. D.

In general, additional energy loss channels in a supernova can rival the neutrino channel, potentially conflicting with the observed neutrino signals from SN 1987A [95, 96]. This can be translated into a constraint on weakly coupled particles. In particular, if the luminosity in axions exceeds the neutrino luminosity, this would lead to a shortening of the neutrino signal [10]. As a criterion, we adopt comparing the luminosities 1 s post-bounce. The supernova simulation employed in this work has a neutrino luminosity 1 s post-bounce⁵ of

$$L_\nu \sim 5.5 \times 10^{52} \text{ erg s}^{-1}. \quad (4.4)$$

Demanding that the luminosity in axions is smaller than that leads to a bound of

$$f_a \gtrsim 1.0_{-0.2}^{+0.5} \times 10^9 \text{ GeV}, \quad m_a \lesssim 5.9_{-2.0}^{+1.8} \text{ meV}. \quad (\text{including vertex corrections}) \quad (4.5)$$

This can be compared with the naive bound that is found with the same SN but using the leading order process only. In that case one finds

$$f_a \gtrsim 6.1_{-1.4}^{+1.7} \times 10^8 \text{ GeV}, \quad m_a \lesssim 9.8_{-2.2}^{+3.0} \text{ meV}. \quad (\text{leading order}) \quad (4.6)$$

One can see that including the vertex corrections strengthens the SN bound on the axion mass (or decay constant) by roughly a factor of two.

Let us briefly compare our findings to the recent literature. We find a strengthening of the SN bound on f_a as compared to [23, 24] by a factor of a few and up to an order of magnitude, respectively. This enhancement can be attributed to two main factors. First, in our case, the luminosity is enhanced compared to the OPE when including the axion form factors. And second, in both [23] and [24] the reduction of the axion luminosity due to a reduction of the nucleon-nucleon interaction, as well as due to multiple nucleon scatterings [10], was modeled in a phenomenological way. A systematic analysis of these effects in SN environments is still missing [105] (see discussion of diagrams (c), (d), (g) above). Our focus has been on the previously unexplored and significant axion vertex corrections. We expect the enhancement due to the modified couplings to remain. This underscores that our analysis should be viewed as a first step and emphasizes the need for a systematic evaluation of axion emission during SN core collapse within ChPT.

Finally, we emphasize that a systematic and consistent axion bound from supernovae cannot be achieved by combining this ChPT approach with additional phenomenological corrections.

4.2 Neutron star cooling bound

Axions can be produced in scattering processes within the neutron star core and can escape the star due to their weak interaction [11, 112], the dominant contribution again being axion production via nucleon-nucleon Bremsstrahlung, and thereby modify the cooling of NSs [22].

⁵Note that similar effects as considered for the axion luminosity can also affect neutrino luminosity. However, while the axion is free streaming, neutrinos are trapped at large densities. Because of this, the neutrino luminosity mainly depends on low-density regions, and we expect only small corrections, as seen when including the quenching of g_A [111].

The typical density in the bulk of neutron star matter is $n \sim \mathcal{O}(\text{few})n_0$. While a significant portion of a neutron star’s luminosity arises from regions with densities around $(0.5 - 2)n_0$, the precise contribution depends on the neutron star’s maximum mass and the chosen equation of state (EOS). However, the luminosity originating from high-density regions, where no controlled calculation exists and, in particular, the ChPT expansion is no longer applicable, is considerable and can exceed the low-density contribution. This is especially pronounced for heavier NSs.

This limitation suggests two possible approaches for dealing with the high-density regions. The first approach sets the axion cooling bound by focusing solely on parts of the neutron star where controlled calculations are possible - specifically, regions with densities below nuclear saturation density. Since this approach neglects large parts of the star which contribute to the axion luminosity, we find that for vacuum couplings, it weakens the bound on the decay constant by a factor of three to six compared to Ref. [22], depending on the exact mass of the star and to a small extent on the EOS used.

However, within this approach, the emissivity can be systematically calculated using finite-density couplings. We compute the luminosity resulting from the region below nuclear saturation density ($n \lesssim 1n_0$), including the full systematic density dependence of the axion-nucleon coupling.⁶

We find that using systematically calculated axion-nucleon couplings further relaxes the bound—beyond the reduction already caused by neglecting a significant portion of the star—primarily due to the diminished axion-proton coupling at high densities (see Eq. (3.35)). This effect reduces the 1σ lower bound on the axion mass by a factor of a bit more than two. This result contrasts with the strengthening of the supernova bound discussed in Sec. 4.1, which arises because neutron star temperatures are significantly lower. Consequently, effects such as the energy dependence of the axion-nucleon coupling, which we include there for the first time, become negligible for NSs.

For concreteness, we consider a neutron star with $1.5M_\odot$ using the BSk24 EOS [116]. Comparing with Ref. [22], we find the bound on the KSVZ axion model from neutron star cooling in the conservative approach to be

$$f_a \gtrsim 1.0_{-0.2}^{+0.3} \times 10^8 \text{ GeV}, \quad m_a \lesssim 60_{-13}^{+28} \text{ meV}, \quad 68\% \text{ C.L.}, \quad (\text{KSVZ}) \quad (4.7)$$

where we sample over the axion-nucleon couplings within their ChPT error bars, see Sec. 3. This is a significant weakening of the bound on the axion mass and decay constant.

Another less rigorous approach estimates axion production in the high-density regime ($n \gtrsim 1n_0$) by making use of naive dimensional analysis to determine the axion couplings,

$$|\mathcal{A}_{aN}| \sim 0.3(3), \quad (4.8)$$

⁶We adopt the same phenomenological suppression factors as in [22] describing the short-range nucleon-nucleon scattering [113, 114], the density modification of the pion nucleon coupling [115] as well as multiple pion exchange. While this approach sacrifices all systematic rigor, a more consistent evaluation of these terms would be desirable but exceeds the scope of this work. We then compare these results with the luminosity from the entire star, however, using the phenomenological density dependence of the couplings from [115] employed in [22].

where the range is inspired by Eq. (2.31) with order one coefficients.

Due to the density gradient inside the star, it is improbable that the couplings remain small at all densities. If the vacuum couplings are not tuned, their values have minimal impact on axion-induced neutron star cooling, and no distinction between different axion models is possible. Assuming Eq. (4.8) for the region of the NS where $n \gtrsim 1n_0$, we calculate the luminosity and set a more aggressive bound on the axion mass and decay constant,

$$f_a \gtrsim 5.3_{-2.7}^{+1.8} \times 10^8 \text{ GeV}, \quad m_a \lesssim 11_{-2}^{+15} \text{ meV}, \quad 68\% \text{ C.L.} \quad (\text{model-independent}), \quad (4.9)$$

which is independent of the axion model under consideration, assuming no tuning, and completely neglects any potential axion production in the low-density region of the NS.

If additionally the contribution to the luminosity from the low-density region of the star is taken into account, we find for *e.g.* the KSVZ axion

$$f_a \gtrsim 5.4_{-2.7}^{+1.7} \times 10^8 \text{ GeV}, \quad m_a \lesssim 11_{-3}^{+12} \text{ meV}, \quad 68\% \text{ C.L.} \quad (\text{KSVZ}). \quad (4.10)$$

Similar bounds can be derived for any axion model, with the main contribution to the luminosity coming from the region with large densities, see Eq. (4.9), where a distinction between models is not possible.

However, there are QCD axion models, such as the astrophobic axion [77], where the shift symmetric couplings of the axion are tuned. In such cases, the dominant contribution to the coupling $|\mathcal{A}_{aN}|$ comes from shift symmetry- and isospin-breaking terms, which are hence suppressed. This suppression should also hold at large densities, see [93] for a related study. Therefore the NS cooling bound is weaker than expected from our NDA estimate.

Nevertheless, we point out that there exists an additional process that arises from a shift-symmetry breaking operator and contributes to axion cooling both in supernovae and neutron stars that cannot be tuned small for any QCD axion model. We explore this process in light of an additional energy loss channel during supernovae cooling in a companion paper [76].

For neutron star cooling, taking all derivative couplings to be zero, we calculate the axion luminosity, which gives rise to a bound from NS cooling on the axion mass of $m_a \lesssim 149_{-31}^{+87} \text{ meV}$ and decay constant of $f_a \gtrsim 4.1_{-1.5}^{+1.0} \times 10^7 \text{ GeV}$.

4.3 Terrestrial experiments

Our findings are not only relevant for high-density astrophysical objects like supernovae and neutron stars, but also have important implications for axion dark matter detection experiments, which target the axion-nucleon derivative coupling [34–53]. Similarly higher order density corrections to non-derivative couplings, can be important for time-dependent new physics searches such as current and future nuclear clock experiments [56–60]. Nucleons inside a large nucleus do not have small momenta, and in the axion-nucleon interaction, the rest of the nucleus can be seen as a background density.

This is in direct analogy to the well-known quenching of G_A in the beta decay of large nuclei, see, *e.g.*, [54, 55]. There, the rate of Gamov-Teller transitions is related to the reduced matrix element

$$|\mathcal{M}_{GT}| = |\langle f | \vec{O}_{GT}^\pm | i \rangle|. \quad (4.11)$$

with the usual Gamov-Teller operator,

$$\vec{O}_{GT}^{\pm} = 2G_A \vec{S} \tau^{\pm}. \quad (4.12)$$

Inside nuclei however, there are higher order contributions to the Gamov-Teller operator induced by the background nucleons, leading to a quenching of G_A as described *e.g.* in [54, 55].

The interaction of a dark matter axion background wind with nuclei on Earth is an analogous problem. One has to evaluate a similar matrix element, however with \vec{O}_{GT}^{\pm} replaced by $2\vec{S} (G_A \tau^3 + G_0 \mathbb{1})$. The higher-order contributions from a homogeneous background of the other nucleons are exactly the ones discussed in Sec. 3.2.

However, the study of axion coupling with nuclei is complex and depends on the specific nucleus, posing a challenging nuclear physics problem beyond the scope of our work. To provide a preliminary estimate, we model the nucleus as a Fermi gas, similar to the approach used in [54] for the quenching of G_A in beta decays.

Then the axion-nucleon coupling Eq. (3.31) has to be evaluated around nuclear saturation density and for mixed matter, leading for the KSVZ axion to Eq. (3.35). While this changes the predictions of the QCD axion and ALP couplings by $\mathcal{O}(1)$, in case of detection, this can be crucial to discriminate UV completions. Even if a UV model predicts a small (or vanishing) derivative axion coupling in vacuum, experiments using large nuclei are still expected to be sensitive. A notable example of this is the KSVZ axion neutron coupling, where the mean value is estimated to be enhanced by a factor of ~ 3 .

5 Conclusions

In this work, we have conducted the first systematic study on the interactions of QCD axions with nucleons in the formalism of chiral perturbation theory, including non-relativistic baryons, at finite nuclear density and temperature.

We reviewed the effective theory of QCD axions across different energy scales. We started with the effective axion theory at energies below electroweak symmetry breaking and matched to the chiral, two-flavor Lagrangian, including mesons and non-relativistic baryons, at energies below the QCD confinement scale. We constructed the effective Lagrangian consistent with power counting up to next-to-leading order. This theory describes the axion-nucleon and axion-meson interactions relevant in dense and hot environments, like those found in supernovae and neutron stars.

Our results reveal that the axion-nucleon couplings in these environments are highly sensitive to both momentum and energy, with contributions arising from ordinary loop corrections and finite density effects.

At energies $\omega_a \simeq m_\pi$, where virtual pions can go on-shell, we found that the form factor acquires a significant imaginary part, which has to be included in phenomenological applications. We have found that the axion-nucleon form factors generically change $\mathcal{O}(1)$ for axion energies up to $\omega_a \simeq 2m_\pi$. Notably, for the KSVZ axion, an accidental cancellation at zero energy that results in a suppressed coupling to neutrons is lifted as the axion energy increases, with the form factor enhanced by up to an order of magnitude at $\omega_a \simeq 2m_\pi$.

We calculated the density dependence of the axion-nucleon form factors systematically for the first time. We used the real-time formalism of thermal quantum field theory to do this. In this approach, the nucleon propagator gets an additional component that depends on temperature and chemical potential, which represents the interaction with the nucleon background. In the $T \rightarrow 0$ limit, this additional piece is usually referred to as a density insertion. In practice, density effects are then calculated by evaluating loop diagrams where an internal nucleon propagator is replaced by the density insertion.

We found that the density corrections predominantly scale with the nucleon Fermi momentum, contrary to the pure loop effects, which scale with the axion energy. Therefore, if the axion energies are negligible, the momentum dependence of the axion-nucleon couplings is dominated by density effects. This is particularly important for environments with low temperatures and high densities.

We have calculated both loop and density corrections up to chiral order $\nu = 3$, including large Wilson coefficients that occur due to the low-lying $\Delta(1232)$ -resonance. We found that higher-order and density-corrected couplings have significant implications for phenomenological applications both in astrophysical environments as well as for terrestrial experiments.

On the astrophysical side, supernova explosions present themselves as ideal laboratories to apply our result: the extreme densities and temperatures in supernova environments have a large influence on the axion couplings and, consequently, significantly change the axion production rate. We evaluated the supernova bound on the QCD axion, focussing on the predictive KSVZ model, including our density-dependent couplings, and found that the axion luminosity during SN 1987A can be enhanced by up to one order of magnitude. This translates to a stricter bound on the axion decay constant f_a by a factor of three compared to previous works, *e.g.* [23]. We highlighted the systematic treatment of the axion couplings, allowing for the first time to estimate a concise uncertainty for the axion luminosity, which directly propagates to the bound, which we found as

$$f_a \gtrsim 1.0_{-0.2}^{+0.5} \times 10^9 \text{ GeV}, \quad m_a \lesssim 5.9_{-2.0}^{+1.8} \text{ meV}. \quad (\text{KSVZ}) \quad (5.1)$$

For our analysis, we used the supernova profile [108] kindly provided by the Garching group of Thomas Janka [107]. While we found that the density correction due to the chemical potential alone could potentially reduce the axion luminosity, the large temperatures present during a supernova explosion, of order ~ 30 MeV, leads to a large axion high energy component and consequently to an enhanced axion production rate.

We emphasize that the density-dependent axion-nucleon couplings evaluated in this work mark an important first step towards a consistent evaluation of the complete axion production during supernovae. In order to get a consistent result up to a given order in the chiral expansion, one needs to evaluate every diagram that contributes to the axion production to that order. We classified all such contributions up to chiral order $\nu = 3$, which we will present in future publications. While the bound provided here incorporates all existing perturbative corrections, a comprehensive analysis that includes a complete set of diagrams could yield a different axion constraint. We stress that combining phenomeno-

logical effects, such as *e.g.* rho meson exchange or multiple scatterings, with our systematic corrections is inconsistent and should be avoided.

Next, we studied the effect of density-dependent axion-nucleon couplings on axion production in neutron star environments, which are characterized by large densities but low temperatures. We re-evaluated the neutron star cooling bound, including density-dependent axion-nucleon couplings.

Within neutron stars, densities exceed nuclear saturation by a factor of a few, and the axion-nucleon coupling is dominantly influenced by high nucleon densities, contrary to supernovae. At these large densities, the chiral series breaks down, and all perturbative control is lost. However, we consistently calculated the axion luminosity, including our modified density-dependent couplings at low densities, where the chiral expansion is valid.

In order to place a conservative, fully controlled bound, we considered the axion luminosity arising from these low densities only. By re-evaluating the most recent bound from Ref. [22], we found that the axion bound from neutron star cooling is relaxed by up to one order of magnitude. In particular, for the KSVZ axion, we find

$$f_a \gtrsim 1.0_{-0.2}^{+0.3} \times 10^8 \text{ GeV}, \quad m_a \lesssim 60_{-13}^{+28} \text{ meV}, \quad 68\% \text{ C.L.} \quad (\text{KSVZ}) \quad (5.2)$$

This relaxation of the bound comes from two effects: we restrict our analysis to regions of the star where the density is sufficiently low to permit a perturbative treatment, and the axion-proton coupling decreases at finite density, while temperature effects remain negligible. As for the supernovae calculation, one should calculate all axion production channels and include corrections systematically. We leave this and further improvements for future work.

In order to place a more aggressive but less rigorous bound, we included the axion luminosity from high-density regions using order one axion-nucleon couplings estimated via naive dimensional analysis, which are expected for any axion model that is not tuned. In this case, we find a similar bound as previous works Ref. [22], which holds independent of the underlying (not-tuned) QCD axion model. As a consequence, this more aggressive bound on the axion from neutron star cooling cannot distinguish between different axion models.

In the supplementary file, we provide numerical tables for density and temperature-dependent axion-nucleon couplings, including error bars as estimated within the ChPT expansion, which can be used in dedicated supernova simulations [🔗](#).

Finally, we investigated the phenomenological consequences of density-dependent axion-nucleon couplings in axion experiments on Earth. Inside large nuclei, our findings correct the axion couplings to nucleons by an order one factor, which is relevant to all searches sensitive to axion-nucleon couplings, such as nucleon spin-precession experiments or the nuclear clock. Especially in case of a discovery it will be important to precisely determine the fundamental couplings of the axion field to quarks and gluons, in which case our findings will be crucial.

Our work opens up multiple new avenues for future work. We have established a framework for a systematic and fully controlled axion precision phenomenology at finite density and temperature. In future works, we will address the crucial task of calculating

the missing diagrammatic contributions to axion production relevant to SNe and NSs, which we have classified in this work. In a subsequent paper, we will investigate how modifications to the nucleon-nucleon interaction influence the axion production rate in supernova environments [105]. Additionally, this framework should also be extended for key standard model processes, such as neutrino dynamics in the same environments, which we will explore in upcoming work [117].

Furthermore, a fully self-consistent SNe simulation, taking into account the additional energy loss from axion production, is needed. Such a simulation can benefit from our findings of axion couplings derived in this work but eventually has to include neutrino and axion production rates calculated consistently at finite density and temperature.

Lastly, we note that our findings allowed us to calculate a model-independent independent contribution to the axion luminosity during supernovae which we present in [76].

Our findings provide a framework for revisiting axion phenomenology in extreme astrophysical environments, enabling precision studies and guiding future discoveries in both theoretical and experimental axion physics.

Acknowledgements

We would like to thank Reuven Balkin, Alexander Bartl, Kai Bartnick, Andrea Caputo, Pierluca Carenza, Tim Cohen, Raffaele Del Grande, Majid Ekhterachian, Laura Fabbietti, Albert Feijoo, Tobias Fischer, Doron Gazit, Malte Heinlein, Anson Hook, Thomas Janka, Norbert Kaiser, Daniel Kresse, Valentina Mantovani Sarti, Georg Raffelt, Riccardo Rattazzi, Sanjay Reddy, Javi Serra, and Giovanni Villadoro for useful conversations and discussions. We would especially like to thank Thomas Janka and his group for providing us with supernova simulation data and Tobias Fischer for helping us cross-check our numerical simulations. This work has been supported by the Collaborative Research Center SFB1258, the Munich Institute for Astro-, Particle and BioPhysics (MIAPbP), and by the Excellence Cluster ORIGINS, which is funded by the Deutsche Forschungsgemeinschaft (DFG, German Research Foundation) under Germany’s Excellence Strategy – EXC 2094 – 39078331. The research of MS is partially supported by the International Max Planck Research School (IMPRS) on “Elementary Particle Physics”. KS is supported by a research grant from Mr. and Mrs. George Zbeda. SS is partially supported by the Swiss National Science Foundation under contract 200020-213104. SS thanks the CERN theory group for its hospitality.

A Construction of the effective axion HBChPT Lagrangian

In this appendix, we briefly summarize the construction of the effective axion chiral Lagrangian in HBChPT up to N²LO and some selected pieces N³LO, necessary for renormalization. We start by writing down the relativistic pion axion nucleon Lagrangians and projecting to HBChPT. For reviews on the subject without the axion, see *e.g.* Refs. [33, 69, 70], as well as Refs. [118] for the HBChPT projection. The LO axion HBChPT Lagrangian as well as some selected terms at N²LO are constructed in Ref. [81].

A.1 Chiral QCD Lagrangian

We analyze the transformation properties of external sources, performing a spurion analysis. Starting point is the QCD Lagrangian with external isovector axial vector (a_μ), isoscalar axial vector (a_μ^s), scalar (s) and pseudo-scalar (p) sources. In absence of isovector and isoscalar vector sources ($v_\mu^{(s)} = 0$), which is the case for axion ChPT, we can write parity eigenstates in terms of left- and right-handed fields, *i.e.* $r_\mu^{(s)} = a_\mu^{(s)}$ and $\ell_\mu^{(s)} = -a_\mu^{(s)}$. The QCD Lagrangian containing external sources then reads

$$\mathcal{L}_{\text{ext}} = \bar{q}_L \gamma^\mu (\ell_\mu + \ell_\mu^s) q_L + \bar{q}_R \gamma^\mu (r_\mu + r_\mu^s) q_R - \bar{q}_L (s - ip) q_R - \bar{q}_R (s + ip) q_L, \quad (\text{A.1})$$

where $q_{L/R}$ are left- and right-handed quark fields. Isovector and isoscalar parts are associated with the $SU(2)$ and $U(1)$ parts of $U(2)$, respectively. The Lagrangian $\mathcal{L}_{\text{QCD}} = \mathcal{L}_{\text{QCD},0} + \mathcal{L}_{\text{ext}}$, with $\mathcal{L}_{\text{QCD},0}$ given by Eq. (2.2a), is invariant under local $U(2)_L \times U(2)_R$ transformations

$$q_{L/R} \rightarrow \exp\left(-i\frac{\theta_{L/R}(x)}{3}\right) V_{L/R}(x) q_{L/R}, \quad \theta_{L/R} \in U(1)_{L/R}, \quad V_{L/R} \in SU(2)_{L/R}, \quad (\text{A.2})$$

as long as the external fields satisfy

$$\begin{aligned} r_\mu &\rightarrow V_R r_\mu V_R^\dagger + i V_R \partial_\mu V_R^\dagger, \\ \ell_\mu &\rightarrow V_L \ell_\mu V_L^\dagger + i V_L \partial_\mu V_L^\dagger, \\ \ell_\mu^s &\rightarrow \ell_\mu^s - \frac{1}{3} \partial_\mu \theta_L, \\ r_\mu^s &\rightarrow r_\mu^s - \frac{1}{3} \partial_\mu \theta_R, \\ (s - ip) &\rightarrow e^{-\frac{i}{3}(\theta_L - \theta_R)} V_L (s - ip) V_R^\dagger, \\ (s + ip) &\rightarrow e^{-\frac{i}{3}(\theta_R - \theta_L)} V_R (s + ip) V_L^\dagger. \end{aligned} \quad (\text{A.3})$$

The derivative terms cancel analogous terms originating from the kinetic terms in the Lagrangian and are later used to construct covariant derivatives.

A.2 Effective Pion Lagrangian

In the broken phase, pions are described by the unitary flavor matrix U , see Eq. (2.12). It transforms linearly under chiral and axial $U(1)_A$ transformations

$$U \rightarrow e^{-\frac{i}{3}(\theta_R - \theta_L)} V_R U V_L^\dagger. \quad (\text{A.4})$$

Since it collects the NGBs, associated with the broken generators of chiral symmetry breaking, it is charged under axial transformations only. Furthermore, under C and P transformations the NGBs and U transform as

$$\begin{aligned}\boldsymbol{\pi}(x) &\xrightarrow{\text{C}} \boldsymbol{\pi}^T(x), & \boldsymbol{\pi}(x) &\xrightarrow{\text{P}} -\boldsymbol{\pi}(\mathcal{P}x) \\ U(x) &\xrightarrow{\text{C}} U^T(x), & U(x) &\xrightarrow{\text{P}} U^\dagger(\mathcal{P}x).\end{aligned}\tag{A.5}$$

The covariant derivative is given by the linear representation

$$\nabla_\mu U = \partial_\mu U - i(r_\mu + r_\mu^s)U + iU(\ell_\mu + \ell_\mu^s),\tag{A.6}$$

resulting in Eq. (2.15). Another spurion in the pion sector can be defined as

$$\chi = 2BM_a^\dagger = 2B(s + ip),\tag{A.7}$$

see below Eq. (2.14), which transforms as

$$\chi \rightarrow V_R \chi V_L^\dagger.\tag{A.8}$$

In the meson sector, the list of fundamental building blocks that we are interested in *i.e.* up to $O(p^2)$ is

$$U, \nabla_\mu U, \nabla_\mu \nabla_\nu U, \chi.\tag{A.9}$$

Out of these, the only non-trivial, hermitian, C and P invariant scalars under Lorentz are collected in the Lagrangian Eq. (2.14).

At NLO one finds the following Lagrangian [69] with the covariant derivative and χ now including the axion,

$$\begin{aligned}\mathcal{L}_{\pi\pi}^{(4)} &= \frac{l_1}{4} \left\{ \text{Tr} \left[D_\mu U (D^\mu U)^\dagger \right] \right\}^2 + \frac{l_2}{4} \text{Tr} \left[D_\mu U (D_\nu U)^\dagger \right] \text{Tr} \left[D^\mu U (D^\nu U)^\dagger \right] \\ &+ \frac{l_3}{16} \left[\text{Tr} \left(\chi U^\dagger + U \chi^\dagger \right) \right]^2 + \frac{l_4}{4} \text{Tr} \left[D_\mu U (D^\mu \chi)^\dagger + D_\mu \chi (D^\mu U)^\dagger \right] \\ &- \frac{l_7}{16} \left[\text{Tr} \left(\chi U^\dagger - U \chi^\dagger \right) \right]^2 + \frac{h_1 + h_3}{4} \text{Tr} \left(\chi \chi^\dagger \right) \\ &+ \frac{h_1 - h_3}{16} \left\{ \left[\text{Tr} \left(\chi U^\dagger + U \chi^\dagger \right) \right]^2 + \left[\text{Tr} \left(\chi U^\dagger - U \chi^\dagger \right) \right]^2 \right. \\ &\left. - 2 \text{Tr} \left(\chi U^\dagger \chi U^\dagger + U \chi^\dagger U \chi^\dagger \right) \right\}.\end{aligned}\tag{A.10}$$

We use this Lagrangian to calculate the axion-pion mixing at NLO as well as for the matching of the pion mass and decay constant.

A.3 Effective Baryon Lagrangian

The baryon field transforms non-linearly under chiral transformations

$$\Psi' = e^{-i\theta_V(x)} K(V_L(x), V_R(x), U(x)) \Psi,\tag{A.11}$$

where $K(V_L, V_R, U)$ is the so-called compensator field and defines a non-linear $SU(N_f)$ valued function of U and V_L, V_R , defined by

$$U(x) = u^2(x), \quad u(x) \rightarrow u'(x) = \sqrt{V_R U V_L^\dagger} \equiv V_R u K^{-1}(V_L, V_R, U),\tag{A.12}$$

such that the explicit form of K is easily evaluated to

$$K(V_L, V_R, U) = (u')^{-1} V_R u = \left(\sqrt{V_R U V_L^\dagger} \right)^{-1} V_R \sqrt{U}. \quad (\text{A.13})$$

The covariant derivative is given by

$$\begin{aligned} D_\mu \Psi &= (\partial_\mu + \Gamma_\mu) \Psi, \\ \Gamma_\mu &= \frac{1}{2} \left[u^\dagger (\partial_\mu - i r_\mu) u + u (\partial_\mu - i \ell_\mu) u^\dagger \right], \end{aligned} \quad (\text{A.14})$$

where Γ_μ is the chiral connection. Under parity and charge conjugation it transforms as

$$D_\mu \xrightarrow{\text{P}} +\mathcal{P}_\mu^\nu D_\nu, \quad D_\mu \xrightarrow{\text{C}} -D_\mu^T. \quad (\text{A.15})$$

with $\mathcal{P}_\mu^\nu = \text{Diag}(1, -1, -1, -1)$. One can furthermore construct a hermitian, isovector, axial vector object containing one derivative, called the vielbein

$$u_\mu = i \left[u^\dagger (\partial_\mu - i r_\mu) u - u (\partial_\mu - i \ell_\mu) u^\dagger \right] = i u^\dagger (\partial_\mu U - i r_\mu U + i U \ell_\mu) u^\dagger. \quad (\text{A.16})$$

The transformation behavior under $SU(2)_L \times SU(2)_R$, parity (P) and charge conjugation (C) is

$$u_\mu \xrightarrow{SU(2)_L \times SU(2)_R} K u_\mu K^\dagger, \quad u_\mu \xrightarrow{\text{P}} -\mathcal{P}_\mu^\nu u_\nu, \quad u_\mu \xrightarrow{\text{C}} u_\mu^T. \quad (\text{A.17})$$

u_μ sandwiched between a baryon bilinear stays invariant under local chiral gauge transformations. There exist two identities for the covariant derivative,

$$[D_\mu, D_\nu] = \frac{1}{4} u_\mu u_\nu, \quad (\text{A.18a})$$

$$[D_\mu, u_\nu] = [D_\nu, u_\mu]. \quad (\text{A.18b})$$

The first is known as curvature relation and shows that only completely symmetrized products of D_μ with itself as well as products of D_μ with u_μ have to be considered. The second relation shows in a similar way that covariant derivatives on the vielbein have to be taken into account in a completely symmetrized combination only. We can construct an analogous quantity to the vielbein from the isoscalar part of the linearly realized covariant derivative

$$\hat{u}_\mu = i u^\dagger (-i r_\mu^s U + i U \ell_\mu^s) u^\dagger = i u^\dagger (-2i a_\mu^s U) u^\dagger = 2a_\mu^s, \quad (\text{A.19})$$

which under parity and charge conjugation has exactly the same transformation properties as u_μ but only transforms under $U(1)_A$

$$\hat{u}_\mu \xrightarrow{U(1)_A} \hat{u}_\mu - \partial_\mu \alpha_A, \quad \hat{u}_\mu \xrightarrow{\text{P}} -\mathcal{P}_\mu^\nu \hat{u}_\nu, \quad \hat{u}_\mu \xrightarrow{\text{C}} \hat{u}_\mu^T. \quad (\text{A.20})$$

Furthermore, we need a non-linearly transforming analog to the field χ , which we construct as hermitian and anti-hermitian combinations

$$\chi_\pm = u^\dagger \chi u^\dagger \pm u \chi^\dagger u, \quad (\text{A.21})$$

with transformation properties

$$\chi_{\pm} \xrightarrow{SU(2)_L \times SU(2)_R} K \chi_{\pm} K^\dagger, \quad \chi_{\pm} \xrightarrow{P} \pm \chi_{\pm}, \quad \chi_{\pm} \xrightarrow{C} \chi_{\pm}^T. \quad (\text{A.22})$$

For the construction of the chiral Lagrangian, it will be useful to separate every field into isovector and isoscalar components. Therefore we define

$$\tilde{X} = X - \frac{1}{2} \langle X \rangle, \quad (\text{A.23})$$

where $\langle \cdot \rangle$ denotes the flavor trace such that \tilde{X} projects out the isovector part of X . The basic building blocks in this form are therefore $u_\mu, \hat{u}_\mu, \tilde{\chi}_\pm, \langle \chi_\pm \rangle$. Note that in the special case of Pauli matrices, one finds

$$\langle \tau_i \tau_j \rangle \mathbb{1} = \{ \tau_i, \tau_j \}. \quad (\text{A.24})$$

We are now in the position to construct the chiral nucleon Lagrangian containing the axion. In the following we, write down the minimal set of operators for which we closely follow Ref. [118]. Invariant monomials take the generic form

$$\bar{\Psi} A^{\mu\nu\dots} \Theta_{\mu\nu\dots} \Psi + \text{h.c.} \quad (\text{A.25})$$

The operator $A^{\mu\nu\dots}$ is a product of pion and/or external fields and their covariant derivatives, all of course in the non-linear representation. $\Theta_{\mu\nu\dots}$ is a product of Clifford algebra elements $\Gamma_{\mu\nu\dots}$ and the symmetrized product of n covariant derivatives $D_{\alpha\beta\dots}^n = \{D_\alpha, \{D_\beta, \{\dots, D_\omega\}\}\}$ acting on the nucleon field.

$\Gamma_{\mu\nu\dots}$ contains Clifford algebra elements which are understood to be expanded in the basis $(\mathbb{1}, \gamma_5, \gamma_\mu, \gamma_5 \gamma_\mu, \sigma_{\mu\nu})$ and the metric $\eta_{\mu\nu}$ as well as Levi-Civita symbols $\varepsilon_{\mu\nu\alpha\beta}$. Eq. (A.25) is not the most general form. The fact that $\Theta_{\mu\nu\dots}$ contains only the totally symmetrized product of covariant derivatives acting on Ψ is due to the curvature relation, see Eq. (A.18a). Another property, namely that no two indices of $\Theta_{\mu\nu\dots}$ are contracted (except for Levi-Civita symbols) is due the fact that at a given chiral order $\not{D}\Psi$ can always be replaced by $-im_N\Psi$. This explains why a couple of Clifford algebra structures do not need to be considered, *e.g.* the LHS of $\bar{\Psi} A^{\alpha\beta\dots} \gamma^\lambda D_{\lambda\alpha\beta\dots}^n \Psi + \text{h.c.} = -im_N \bar{\Psi} A^{\alpha\beta\dots} D_{\alpha\beta\dots}^{n-1} \Psi$ is replaced by the RHS. More such eliminations due to the use of the EOM can be made and the minimal set is shown, ordered by ascending chiral power, given in Ref. [118] to be

$$\begin{aligned} & \mathbb{1}, \\ & \gamma_5 \gamma_\mu, D_\mu, \\ & \eta_{\mu\nu}, \sigma_{\mu\nu}, \gamma_5 \gamma_\mu D_\nu, D_{\mu\nu}, \end{aligned} \quad (\text{A.26})$$

where $D_{\mu\nu} = \{D_\mu, D_\nu\}$.

For the operator $A^{\mu\nu\dots}$ one writes down combinations of fields in every ordering. The number of Lorentz indices gives the chiral power. Furthermore, it is instructive to write them in terms of commutator and anticommutator. This has the advantage to obtain simple transformation properties for charge conjugation and parity. In the special case

of $SU(2)$ generators this is equivalent to write as isovector and isoscalar combinations respectively, see Eq. (A.24). The transformation behaviour of the Clifford algebra elements under parity-, charge- and hermitian conjugation in the form

$$\begin{aligned}\Gamma_{\mu\nu\dots}^p &= (\pm 1)\mathcal{P}_\mu^\alpha\mathcal{P}_\nu^\beta\dots\Gamma_{\alpha\beta\dots}, & \Gamma_{\mu\nu\dots}^c &= (\pm 1)\Gamma_{\mu\nu\dots}, \\ \Gamma_{\mu\nu\dots}^\dagger &= (\pm 1)\gamma_0^\dagger\Gamma_{\mu\nu\dots}\end{aligned}\quad (\text{A.27})$$

and the chiral order (including the metric and the Levi-Civita) are shown in Table 3. Note that the full transformation behavior of $\bar{\Psi}\Theta_{\mu\nu\dots\alpha\beta\dots}\Psi = \bar{\Psi}\Gamma_{\mu\nu\dots}D_{\alpha\beta\dots}^n\Psi$ may include an additional sign due to integration by parts, but is included in Table 3. All relevant operators from the minimal list of $\Theta_{\mu\nu\dots}$ are shown, see Eq. (A.26).

$\Theta_{\mu\nu\dots}$	$\mathbb{1}$	γ_5	γ_μ	$\gamma_5\gamma_\mu$	$\sigma_{\mu\nu}$	$\eta_{\mu\nu}$	$\epsilon_{\mu\nu\lambda\rho}$	D_μ	$\gamma_5\gamma_\mu D_\nu$	$D_{\mu\nu}$
$O(p^n)$	$O(1)$	$O(p)$	$O(1)$	$O(1)$	$O(1)$	$O(1)$	$O(1)$	$O(1)$	$O(1)$	$O(1)$
P	+	-	+	-	+	+	-	+	-	+
C	+	+	-	+	-	+	+	-	-	+
†	+	-	+	+	+	+	+	-	-	+

Table 3: Transformation properties of $\Theta_{\mu\nu\dots}$.

The transformation behaviour of the fields $A^{\mu\nu\dots}$ under parity, charge and hermitian conjugation in the form

$$A_{\mu\nu\dots}^p = (\pm 1)^{a_p}\mathcal{P}_\mu^\alpha\mathcal{P}_\nu^\beta\dots A_{\alpha\beta\dots} \quad A_{\mu\nu\dots}^c = (\pm 1)^{a_c}A_{\mu\nu\dots}^T \quad A_{\mu\nu\dots}^\dagger = (\pm 1)^{a_\dagger}A_{\mu\nu\dots} \quad (\text{A.28})$$

as well as the chiral order (including the metric and Levi-Civita) and the combinations of covariant derivatives acting on nucleons are shown in Table 4.

$A_{\mu\nu\dots}$	P	C	†
$O(p)$			
u_μ	-	+	+
\hat{u}_μ	-	+	+
$O(p^2)$			
$\tilde{\chi}_+$	+	+	+
$\langle\chi_+\rangle$	+	+	+
$\tilde{\chi}_-$	-	+	-
$\langle\chi_-\rangle$	-	+	-
$[u_\mu, u_\nu]$	+	-	-
$\langle u_\mu u_\nu \rangle$	+	+	+
$\{\hat{u}_\mu, u_\nu\}$	+	+	+
$\{\hat{u}_\mu, \hat{u}_\nu\}$	+	+	+
$[D_\mu, u_\nu]$	-	+	+
$[D_\mu, \hat{u}_\nu]$	-	+	+

Table 4: Transformation properties of $A_{\mu\nu\dots}$.

With the transformation properties at hand we can write down all operators invariant under parity, charge conjugation and hermitian conjugation at a given chiral order. At first chiral order $O(p)$ we find the relativistic pion nucleon Lagrangian, including the axion

$$\mathcal{L}_{\pi N}^{(1)} = \bar{\Psi} \left(i\not{D} - m_N + \frac{g_A}{2} \not{u} \gamma_5 + \frac{g_0}{2} \not{u} \gamma_5 \right) \Psi, \quad (\text{A.29})$$

given in Eq. (2.20). At the next higher chiral order $O(p^2)$ we find the most general Lagrangian to be

$$\begin{aligned} \mathcal{L}_{\pi N}^{(2)} = \bar{\Psi} \left[c_1 \langle \chi_+ \rangle - \left(\frac{c_2}{8m_N^2} \langle u_\mu u_\nu \rangle D^{\mu\nu} + \text{h.c.} \right) + \frac{c_3}{2} u \cdot u + c_4 \frac{i}{4} [u_\mu, u_\nu] \sigma^{\mu\nu} \right. \\ \left. + c_5 \tilde{\chi}_+ - \left(\frac{c_8}{8m_N^2} \{ \hat{u}_\mu, u_\nu \} D^{\mu\nu} + \text{h.c.} \right) + \frac{c_9}{2} \hat{u} \cdot u \right] \Psi. \end{aligned} \quad (\text{A.30})$$

Note that we dropped all $1/f_a^2$ terms, all terms $\propto [\hat{u}_\mu, u_\nu] \sim \partial_\mu a \partial_\nu \pi^a [1, \tau^a] = 0$, as well as terms $\propto [\hat{u}, \hat{u}] = 0$. Note that $c_{6,7}$ are terms proportional to the field strength tensor, which we do not include here.

Next, we treat the nucleons in the HBChPT limit, as described in Sec. 2.3. We define projection operators according

$$P_{v\pm} = \frac{1 \pm \not{v}}{2}, \quad (\text{A.31})$$

and introduce velocity-dependent fields, *i.e.* velocity eigenstates, N_v and H_v

$$N_v \equiv e^{im_N v \cdot x} P_{v+} \Psi, \quad H_v \equiv e^{im_N v \cdot x} P_{v-} \Psi, \quad (\text{A.32})$$

satisfying

$$\not{v} N_v = +N_v, \quad \not{v} H_v = -H_v. \quad (\text{A.33})$$

Note that we drop the subscript in the main text however it should also there be understood as velocity-dependent. Therefore the nucleon field is decomposed as

$$\Psi(x) = e^{-im_N v \cdot x} [N_v(x) + H_v(x)]. \quad (\text{A.34})$$

Let us consider a positive plane wave solution to the free Dirac equation with momentum \vec{p}

$$\psi_{\vec{p}}^{(+)(\alpha)}(\vec{x}, t) = u^{(\alpha)}(\vec{p}) e^{-ip \cdot x}, \quad (\text{A.35})$$

$$u^{(\alpha)}(\vec{p}) = \sqrt{E(\vec{p}) + m_N} \begin{pmatrix} \chi^{(\alpha)} \\ \frac{\vec{\sigma} \cdot \vec{p}}{E(\vec{p}) + m_N} \chi^{(\alpha)} \end{pmatrix} \quad (\text{A.36})$$

where $E(\vec{p}) = p^0 = \sqrt{\vec{p}^2 + m_N^2}$ and with our choice of v^μ , they are given by

$$P_{v+} = \begin{pmatrix} \mathbb{1}_{2 \times 2} & 0_{2 \times 2} \\ 0_{2 \times 2} & 0_{2 \times 2} \end{pmatrix}, \quad P_{v-} = \begin{pmatrix} 0_{2 \times 2} & 0_{2 \times 2} \\ 0_{2 \times 2} & \mathbb{1}_{2 \times 2} \end{pmatrix}. \quad (\text{A.37})$$

Therefore, the velocity eigenstates take the form

$$N_v^{(\alpha)}(x) = \sqrt{E(\vec{p}) + m_N} \begin{pmatrix} \chi^{(\alpha)} \\ 0_{2 \times 1} \end{pmatrix} e^{-i[E(\vec{p}) - m_N]t + i\vec{p} \cdot \vec{x}}, \quad (\text{A.38})$$

$$H_v^{(\alpha)}(x) = \sqrt{E(\vec{p}) + m_N} \begin{pmatrix} 0_{2 \times 1} \\ \frac{\vec{\sigma} \cdot \vec{p}}{E(\vec{p}) + m_N} \chi^{(\alpha)} \end{pmatrix} e^{-i[E(\vec{p}) - m_N]t + i\vec{p} \cdot \vec{x}}. \quad (\text{A.39})$$

Next, we integrate out the heavy component. We plug the decomposed nucleon field, Eq. (A.34) into the leading order EOM from Eq. (2.20) and get rid of the phase. Then we project out P_{v+} and P_{v-} components, solve one formally for H_v using the definitions

$$A_{\perp}^{\mu} = A^{\mu} - v \cdot A v^{\mu}, \quad v \cdot A_{\perp} = 0, \quad \hat{A}_{\perp} = A_{\perp}^{\mu} \gamma_{\mu}. \quad (\text{A.40})$$

and plug it into the remaining equation, which leads to the following Lagrangian

$$\begin{aligned} \hat{\mathcal{L}} = & \bar{N}_v \left(i v \cdot D + \frac{g_A}{2} \not{v}_{\perp} \gamma_5 + \frac{g_0}{2} \not{v}_{\perp} \gamma_5 \right) N_v + \bar{N}_v \left(i \not{D}_{\perp} + \frac{g_A}{2} v \cdot u \gamma_5 + \frac{g_0}{2} v \cdot \hat{u} \gamma_5 \right) \\ & \times \left(2m_N + i v \cdot D - \frac{g_A}{2} \not{v}_{\perp} \gamma_5 - \frac{g_0}{2} \not{v}_{\perp} \gamma_5 \right)^{-1} \left(i \not{D}_{\perp} - \frac{g_A}{2} v \cdot u \gamma_5 - \frac{g_0}{2} v \cdot \hat{u} \gamma_5 \right) N_v. \end{aligned} \quad (\text{A.41})$$

Now we define the velocity-dependent spin operator

$$S_v^{\mu} \equiv \frac{i}{2} \gamma_5 \sigma^{\mu\nu} v_{\nu} = -\frac{1}{2} (\gamma^{\mu} \not{v} - v^{\mu}), \quad (S_v^{\mu})^{\dagger} = \gamma_0 S_v^{\mu} \gamma_0, \quad (\text{A.42})$$

where again we drop the v sub- or superscript in the main text. It has the properties

$$v \cdot S_v = 0, \quad \{S_v^{\mu}, S_v^{\nu}\} = \frac{1}{2} (v^{\mu} v^{\nu} - \eta^{\mu\nu}), \quad [S_v^{\mu}, S_v^{\nu}] = i \epsilon^{\mu\nu\rho\sigma} v_{\rho} S_v^{\sigma}. \quad (\text{A.43})$$

This definition is very useful since we can trade the 6 different Dirac structures that appear in Eq. (A.41) with two 4×4 matrices, $\mathbb{1}_{4 \times 4}$ and S_v . To that end we use the relations

$$\bar{N}_v \mathbb{1}_{4 \times 4} N_v = \bar{N}_v \mathbb{1}_{4 \times 4} N_v, \quad (\text{A.44a})$$

$$\bar{N}_v \gamma_5 N_v = 0, \quad (\text{A.44b})$$

$$\bar{N}_v \gamma^{\mu} N_v = v^{\mu} \bar{N}_v N_v, \quad (\text{A.44c})$$

$$\bar{N}_v \gamma^{\mu} \gamma_5 N_v = 2 \bar{N}_v S_v^{\mu} N_v, \quad (\text{A.44d})$$

$$\bar{N}_v \sigma^{\mu\nu} N_v = 2 \epsilon^{\mu\nu\rho\sigma} v_{\rho} \bar{N}_v S_v^{\sigma} N_v, \quad (\text{A.44e})$$

$$\bar{N}_v \sigma^{\mu\nu} \gamma_5 N_v = 2i (v^{\mu} \bar{N}_v S_v^{\nu} N_v - v^{\nu} \bar{N}_v S_v^{\mu} N_v). \quad (\text{A.44f})$$

We expand the second bracket in the last term of Eq. (A.41) in orders of $1/m_N^n$ and write

$$\hat{\mathcal{L}} = \hat{\mathcal{L}}_{\pi N}^{(1)} + \sum_{n=1}^{\infty} \frac{1}{(2m_N)^n} \hat{\mathcal{L}}^{(n)}, \quad (\text{A.45})$$

where the first term is exactly given by

$$\hat{\mathcal{L}}_{\pi N}^{(1)} = \bar{N}_v (i v \cdot D + g_A S_v \cdot u + g_0 S \cdot \hat{u}) N_v, \quad (\text{A.46})$$

which we recognize as the leading pion nucleon HBChPT Lagrangian including the axion, see Eq. (2.23). The first term in the sum leads to relativistic corrections at chiral order $O(p^2)$.

Despite relativistic corrections from integrating out the heavy component from the leading order Lagrangian, the other contribution comes from the Lagrangian Eq. (A.30), and we write at chiral order $O(p^2)$

$$\hat{\mathcal{L}}_{\pi N}^{(2)} = \hat{\mathcal{L}}_{\pi N, c_i}^{(2)} + \hat{\mathcal{L}}_{\pi N, 1/m_N}^{(2)}. \quad (\text{A.47})$$

Note that relativistic corrections from integrating out H_v from the EOM of $\mathcal{L}_{\pi N}^{(2)}$ will enter at $O(p^3)$, which we do not need for our analysis in full generality. Therefore, it is sufficient to consider the P_{v+} projection of the $O(p^2)$ EOM and only keep the term proportional to the light component N_v , since the term $\propto H_v$ will only generate relativistic $1/m_N^2$ corrections of chiral order $O(p^3)$. Then, using the relations Eq. (A.44), one finds

$$\begin{aligned} \hat{\mathcal{L}}_{\pi N, c_i}^{(2)} = & \bar{N}_v \left(c_1 \langle \chi_+ \rangle + \frac{c_2}{2} (v \cdot u)^2 + c_3 (u \cdot u) + c_4 [S^\mu, S^\nu] u_\mu u_\nu + c_5 \tilde{\chi}_+ + \right. \\ & \left. + \frac{c_8}{4} (v \cdot u)(v \cdot \hat{u}) + c_9 (u \cdot \hat{u}) \right) N_v. \end{aligned} \quad (\text{A.48})$$

The relativistic corrections come from the first term in the sum of Eq. (A.45), namely

$$\begin{aligned} \hat{\mathcal{L}}_{\pi N, 1/m_N}^{(2)} = & \frac{1}{2m_N} \hat{\mathcal{L}}^{(1)} \\ \simeq & \frac{1}{2m_N} \bar{N}_v \left(i \not{D}_\perp + \frac{g_A}{2} v \cdot u \gamma_5 + \frac{g_0}{2} v \cdot \hat{u} \gamma_5 \right) \left(i \not{D}_\perp - \frac{g_A}{2} v \cdot u \gamma_5 - \frac{g_0}{2} v \cdot \hat{u} \gamma_5 \right) N_v \\ = & \frac{1}{2m_N} \bar{N}_v \left[-D^2 + (v \cdot D)^2 - ig_A \{D \cdot S_v, v \cdot u\} - ig_0 \{D \cdot S_v, v \cdot \hat{u}\} \right. \\ & \left. - \frac{g_A^2}{4} (v \cdot u)^2 - \frac{g_0^2}{4} (v \cdot \hat{u})^2 - \frac{g_A g_0}{2} (v \cdot u)(v \cdot \hat{u}) + \frac{i}{4} \epsilon^{\mu\nu\rho\sigma} [u_\mu, u_\nu] v_\rho S_\sigma^v \right] N_v, \end{aligned} \quad (\text{A.49})$$

where we used

$$\not{D}_\perp \not{D}_\perp = D^2 - (v \cdot D)^2 - \frac{i}{4} \epsilon^{\mu\nu\rho\sigma} [u_\mu, u_\nu] v_\rho S_\sigma^v, \quad (\text{A.50a})$$

$$\not{D}_\perp \gamma_5 = 2D \cdot S_v. \quad (\text{A.50b})$$

The result is therefore

$$\begin{aligned} \hat{\mathcal{L}}_{\pi N}^{(2)} = & \hat{\mathcal{L}}_{\pi N, c_i}^{(2)} + \hat{\mathcal{L}}_{\pi N, 1/m_N}^{(2)} = \\ = & \bar{N}_v \left[-\frac{1}{2m_N} \left(D^2 - (v \cdot D)^2 + ig_A \{S_v \cdot D, v \cdot u\} + ig_0 \{S_v \cdot D, v \cdot \hat{u}\} \right) \right. \\ & + \hat{c}_1 \langle \chi_+ \rangle + \frac{\hat{c}_2}{2} (v \cdot u)^2 + \hat{c}_3 (u \cdot u) + \frac{\hat{c}_4}{2} i \epsilon^{\mu\nu\rho\sigma} [u_\mu, u_\nu] v_\rho S_\sigma^v \\ & \left. + \hat{c}_5 \tilde{\chi}_+ + \frac{\hat{c}_8}{4} (v \cdot u)(v \cdot \hat{u}) + \hat{c}_9 (u \cdot \hat{u}) \right] N_v, \end{aligned} \quad (\text{A.51})$$

where \hat{c}_i include relativistic $1/m_N$ corrections,

$$\begin{aligned}\hat{c}_1 &= c_1, & \hat{c}_2 &= c_2 - \frac{g_A^2}{4m_N}, & \hat{c}_3 &= c_3, & \hat{c}_4 &= c_4 + \frac{1}{4m_N}, \\ \hat{c}_5 &= c_5, & \hat{c}_8 &= c_8 - \frac{g_A g_0}{m_N}, & \hat{c}_9 &= c_9.\end{aligned}\tag{A.52}$$

Now there are still terms in $\hat{\mathcal{L}}_{\pi N, 1/m_N}^{(2)}$ that can be eliminated by appropriate field re-definitions. One can, for instance, eliminate terms $\propto (v \cdot D)^2$. However, since this term does not contribute to our process in practice we do not eliminate it. For completeness, we define

$$N_v \rightarrow \left[1 + \frac{iv \cdot D}{4m_N} - \frac{g_A S_v \cdot u}{4m_N} - \frac{g_0 S_v \cdot \hat{u}}{4m_N} \right] N_v,\tag{A.53}$$

and insert it into Eq. (2.23) gives, up to total derivatives,

$$\begin{aligned}\hat{\mathcal{L}}_{\pi N}^{(1)} &\rightarrow \hat{\mathcal{L}}_{\pi N}^{(1)} + \Delta \hat{\mathcal{L}}_{\pi N}^{(2)} \\ &= \hat{\mathcal{L}}_{\pi N}^{(1)} + \frac{1}{2m_N} \bar{N}_v \left[-(v \cdot D)^2 - \frac{g_A^2}{4} i \epsilon^{\mu\nu\rho\sigma} [u_\mu, u_\nu] v_\rho S_\sigma^v - \frac{g_A^2}{2} (v \cdot u)^2 \right. \\ &\quad \left. + \frac{g_A^2}{4} (u \cdot u) - \frac{g_A g_0}{4} \{v \cdot u, v \cdot \hat{u}\} + g_A g_0 (u \cdot \hat{u}) \right] N_v,\end{aligned}\tag{A.54}$$

and we neglected terms $O(1/m_N^2, 1/f_a^2)$. The first term cancels the EOM term in Eq. (A.49), while the remaining terms shift the constants in Eq. (A.48). In total, we find the HBChPT Lagrangian at chiral order $O(p^2)$ as the sum $\hat{\mathcal{L}}_{\pi N, c_i}^{(2)} + \hat{\mathcal{L}}_{\pi N, 1/m_N}^{(2)} + \Delta \hat{\mathcal{L}}_{\pi N}^{(2)}$ to be

$$\begin{aligned}&\hat{\mathcal{L}}_{\pi N, c_i}^{(2)} + \hat{\mathcal{L}}_{\pi N, 1/m_N}^{(2)} + \Delta \hat{\mathcal{L}}_{\pi N}^{(2)} \\ &= \bar{N}_v \left[-\frac{1}{2m_N} (D^2 + i g_A \{S_v \cdot D, v \cdot u\} + i g_0 \{S_v \cdot D, v \cdot \hat{u}\}) \right. \\ &\quad + \frac{a_1}{m_N} \langle \chi_+ \rangle + \frac{a_2}{2m_N} (v \cdot u)^2 + \frac{a_3}{m_N} (u \cdot u) + \frac{a_4}{2m_N} i \epsilon^{\mu\nu\rho\sigma} [u_\mu, u_\nu] v_\rho S_\sigma^v \\ &\quad \left. + \frac{a_5}{m_N} \tilde{\chi}_+ + \frac{a_8}{8m_N} \{v \cdot u, v \cdot \hat{u}\} + \frac{a_9}{m_N} (u \cdot \hat{u}) \right] N_v\end{aligned}\tag{A.55}$$

where

$$\begin{aligned}\frac{a_1}{m_N} &= c_1, & \frac{a_2}{m_N} &= c_2 - \frac{g_A^2}{8m_N}, & \frac{a_3}{m_N} &= c_3 + \frac{g_A^2}{8m_N}, & \frac{a_4}{m_N} &= c_4 + \frac{1 - g_A^2}{4m_N}, \\ \frac{a_5}{m_N} &= c_5, & \frac{a_8}{m_N} &= c_8 - \frac{g_A g_0}{2m_N}, & \frac{a_9}{m_N} &= c_9 + \frac{g_A g_0}{2m_N}.\end{aligned}\tag{A.56}$$

Note, however, that for convenience in the main text, we will work with the redundant basis of Eq. (A.51).

A.4 Construction of nucleon contact terms

We now construct terms that have four nucleon fields instead of two. We split the construction into pure nucleon contact terms and terms with four nucleons as well as pions or axions.

A.4.1 Pure nucleon contact terms

We start by constructing all possible contact terms containing not more than four nucleons and no other fields. According to Table 3, the only terms with correct transformation properties are

$$\bar{N}N\bar{N}N, \quad \bar{N}S^\mu N\bar{N}S_\mu N. \quad (\text{A.57})$$

Further we can add any number of isospin matrices τ^a , *e.g.* $\bar{N}\tau^a N\bar{N}\tau^a N$ or one including spin matrices such as $\bar{N}S^\mu\tau^a N\bar{N}S_\mu\tau^a N$, as long as all their indices are contracted in the end. It can be shown by doing simple algebraic manipulations that all of them can be written as a linear combination of the operators given in Eq. (A.57), which are, therefore, the only two linear independent operators one can construct. Hence, the Lagrangian for the 2-nucleon contact terms is given by

$$\mathcal{L}_{NN} = -\frac{1}{2}C_S(\bar{N}N)(\bar{N}N) + 2C_T(\bar{N}S N) \cdot (\bar{N}S N), \quad (\text{A.58})$$

with the two well known constants C_S and C_T . Note that the constant $F_\pi^2 C_T \approx 0.02$ is very small [70] and its contribution therefore typically negligible. This is, however, not necessarily the case for the C_S term.

A.4.2 Higher order nucleon contact terms

Next, we aim to construct all possible 2-nucleon contact terms, which include either the field u_μ or \hat{u}_μ . Those are the only fields with chiral dimension one from table Table 4. We start with the ones including u_μ . From Table 4 and Table 3 the only terms one can construct to fulfill the right transformation properties are

$$\bar{N}S^\mu N\bar{N}u_\mu N, \quad \bar{N}N\bar{N}S^\mu u_\mu N, \quad \epsilon^{abc}\epsilon^{\mu\nu\rho\sigma}v_\sigma\bar{N}S_\nu\tau^b N\bar{N}S_\rho\tau^c Nu_\mu^a. \quad (\text{A.59})$$

It can easily be shown that taking the non-relativistic limit and applying Fierz and other basic identities, these are in fact not independent of each other. The explicit relations are $\bar{N}S^\mu N\bar{N}u_\mu N = -\bar{N}N\bar{N}S^\mu u_\mu N$ and $8\bar{N}S^\mu N\bar{N}u_\mu N = \epsilon^{abc}\epsilon^{\mu\nu\rho\sigma}v_\sigma\bar{N}S_\nu\tau^b N\bar{N}S_\rho\tau^c Nu_\mu^a$. Therefore we only need one of them in the Lagrangian which following the literature (*e.g.* [119]) we write as

$$\mathcal{L}_{\pi NN} \supset \frac{c_D}{2f_\pi^2\Lambda_\chi}(\bar{N}N)(\bar{N}S^\mu u_\mu N). \quad (\text{A.60})$$

For the terms involving \hat{u}_μ things are even simpler because \hat{u}_μ is proportional to the identity matrix in isospin space. There are only two possible combinations satisfying the transformation properties given by

$$\bar{N}N\bar{N}S^\mu\hat{u}_\mu N, \quad \bar{N}\tau^a N\bar{N}S^\mu\hat{u}_\mu\tau^a N. \quad (\text{A.61})$$

Again, it can easily be seen that $\bar{N}\tau^a N\bar{N}S^\mu\hat{u}_\mu\tau^a N = -3\bar{N}N\bar{N}S^\mu\hat{u}_\mu N$ and so we find for the Lagrangian

$$\mathcal{L}_{\pi NN} \supset \frac{\tilde{c}_D}{2f_\pi^2\Lambda_\chi}(\bar{N}N)(\bar{N}S^\mu\hat{u}_\mu N). \quad (\text{A.62})$$

This concludes the construction of all terms of the Lagrangian necessary to calculate the corrections to the axion-nucleon coupling. Note, however, that the c_D and \tilde{c}_D terms are not Δ -enhanced, and thus, we do not include them in our calculation of the vertex corrections.

B Cooling rates at finite density

In this appendix, we review how to calculate emissivities in thermal field theory. In App. B.1 we set the stage with basics about thermal field theory in the real-time formalism and eventually derive the density modified nucleon propagator in. We note that this propagator can be derived without using thermal field theory, see App. A of Ref. [94]. We continue to use the previously derived propagator to review thermal particle production rates in App. B.2, have a look at cutting rules at finite density in App. B.3, and eventually discuss how to calculate an emissivity for *e.g.* a SN in App. B.4.

We would like to note that the results in the subsequent sections can be equally derived in thermal field theory using the imaginary time formalism, see *e.g.* [120, 121].

B.1 Nucleon propagator in thermal field theory

The goal of this subsection is to review the derivation of the propagator of a fermion field interacting with a background. In this section we closely follow the review Refs. [92, 122]. In thermal field theory one is mainly concerned with generating functionals of the form

$$\text{Tr} \left[e^{-\beta(\hat{H}-\mu\hat{N})} T \exp \left(i \int_{-t_0}^{t_0} dt \int d^3\vec{x} \bar{j}(x)\psi(x) + j(x)\bar{\psi}(x) \right) \right], \quad (\text{B.1})$$

where $t_0 \in \mathbb{R}$, $j(x)$ is a classical source and T denotes time ordering. Propagators are calculated by taking functional derivatives with respect to the sources. The apparent problem is a systematic way to evaluate the above trace, which includes real-time exponentials as well as imaginary exponentials. The solution is to extend the time variable on a contour in the complex plane and to introduce contour ordering T_c .

We write the generating functional in its path integral representation

$$Z[j, \bar{j}] = \mathcal{N} \int \mathcal{D}[\psi, \bar{\psi}] \exp \left(i \int_{\mathcal{C}} d^4x (\mathcal{L} + \mu\bar{\psi}\gamma_0\psi + \bar{j}\psi + j\bar{\psi}) \right), \quad (\text{B.2})$$

subject to fermionic boundary conditions. We split the Lagrangian into fermion bilinears $\mathcal{L}_0 + \mu\bar{\psi}\gamma_0\psi$ and the interacting part \mathcal{L}_I and formally solve the generating functional

$$\begin{aligned} Z[j, \bar{j}] &= Z_0 \exp \left(i \int d^4y \mathcal{L}_I \left[\frac{\delta}{i\delta\bar{j}}, \frac{\delta}{-i\delta j} \right] \right) \\ &\times \exp \left(-i \int d^4x \int d^4z \bar{j}(x) G_0^{(c)}(x-z) j(z) \right), \end{aligned} \quad (\text{B.3})$$

such that the free, contour ordered propagator satisfies

$$[i\cancel{\partial} + \mu\gamma_0 - m] G_0^{(c)}(x) = \delta^{(4)}(x). \quad (\text{B.4})$$

In terms of retarded and advanced functions we can write the propagator as

$$iG_0^{(c)}(x) = \theta_c(t) \langle \psi(x)\bar{\psi}(0) \rangle_0 - \theta_c(-t) \langle \bar{\psi}(0)\psi(x) \rangle_0, \quad (\text{B.5})$$

where $\langle \cdot \rangle$ denotes the expectation value with respect to the generating functional. The propagator can be explicitly calculated using

$$\begin{aligned}\psi(x) &= \sum_s \int \frac{d^3k}{(2\pi)^3} \frac{1}{\sqrt{2\omega_k}} \left(a_k^s u_k^s e^{-ikx} + b_k^{s\dagger} v_k^s e^{ikx} \right) e^{i\mu t}, \\ \bar{\psi}(x) &= \sum_s \int \frac{d^3k}{(2\pi)^3} \frac{1}{\sqrt{2\omega_k}} \left(a_k^{s\dagger} \bar{u}_k^s e^{+ikx} + b_k^s \bar{v}_k^s e^{-ikx} \right) e^{-i\mu t},\end{aligned}\tag{B.6}$$

where we use

$$\begin{aligned}\langle a_k^s a_p^{s'\dagger} \rangle &= (2\pi)^3 \delta^{ss'} \delta^{(3)}(\vec{k} - \vec{p}) [1 - f_{FD}(\omega_k, \mu)], \\ \langle b_k^{s\dagger} b_p^{s'} \rangle &= (2\pi)^3 \delta^{ss'} \delta^{(3)}(\vec{k} - \vec{p}) f_{FD}(\omega_k, -\mu),\end{aligned}\tag{B.7}$$

with the Fermi-Dirac distribution

$$f_{FD}(\omega, \mu) = \frac{1}{e^{\beta(\omega - \mu)} + 1}.\tag{B.8}$$

One can now explicitly calculate the retarded and advanced functions from Eq. (B.5), using Eqs. (B.6), (B.7), to give the contour dependent particle propagator

$$iG_0^{(c)}(x) = (i\not{\partial} + m) \int \frac{d^4k}{(2\pi)^4} e^{-ikx} \rho_0(k) [f_{FD}(-\omega_k, -\mu)\theta_c(t) - f_{FD}(\omega_k, \mu)\theta_c(-t)],\tag{B.9}$$

with the spectral density

$$\begin{aligned}\rho_0(k) &= 2\pi [\theta(k_0) - \theta(-k_0)] \delta(k^2 - m^2) \\ &= i [\theta(k_0) - \theta(-k_0)] \left(\Delta_{0F}(k) - \Delta_{0F}^\dagger(k) \right),\end{aligned}\tag{B.10}$$

where

$$\Delta_{0F}(k) = \frac{1}{k^2 - m^2 + i\epsilon}.\tag{B.11}$$

Taking the Fourier transform, the propagator can be rewritten as

$$iG_0^{(c)}(k) = iG_{0F}(k) - 2\pi(\not{k} + m)\delta(k^2 - m^2)F_{FD}(\omega_k, \mu),\tag{B.12}$$

where $iG_{0F}(k) = i(\not{k} + m)\Delta_{0F}(k)$ and

$$F_{FD}(\omega_k, \mu) \equiv \theta(k^0) f_{FD}(\omega_k, \mu) + \theta(-k^0) f_{FD}(-\omega_k, -\mu).\tag{B.13}$$

At this point we need to specify a contour \mathcal{C} for the complex time t . Instead of taking the obvious purely imaginary contour from $t_0 \rightarrow t_0 - i\beta$ which gives rise to the imaginary time formalism, we will be interested in the real-time contour shown in Fig. 15. As discussed in Refs. [92, 122], it can be shown that for the contour $\mathcal{C} = \mathcal{C}_1 \cup \mathcal{C}_2 \cup \mathcal{C}_3$ the generating functional factorizes in the limit of infinite real times t_0, t_f

$$\lim_{t_f \rightarrow \infty} \lim_{t_0 \rightarrow -\infty} Z[\bar{j}, j] = Z_{12}[\bar{j}, j] Z_3[\bar{j}, j],\tag{B.14}$$

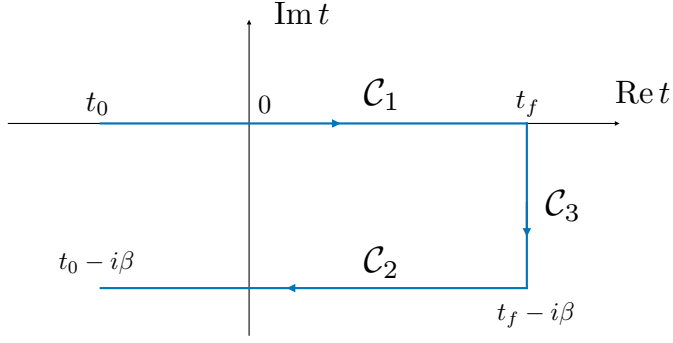


Figure 15: Real-time contour $\mathcal{C} = \mathcal{C}_1 \cup \mathcal{C}_2 \cup \mathcal{C}_3$.

with the important implication that all convolutions of operators from $\mathcal{C}_{1,2}$ with \mathcal{C}_3 vanish. Therefore, we can focus on $Z_{12}[\bar{j}, j]$ and write

$$Z_{12}[j, \bar{j}] = Z_0 \exp \left(i \int d^4 y \left\{ \mathcal{L}_1 \left[\frac{\delta}{i\delta \bar{j}_1}, \frac{\delta}{-i\delta j_1} \right] - \mathcal{L}_1 \left[\frac{\delta}{i\delta \bar{j}_2}, \frac{\delta}{-i\delta j_2} \right] \right\} \right) \times \exp \left(-i \int d^4 x \int d^4 z \bar{j}_k(x) G_0^{(kl)}(x-z) j_l(z) \right), \quad (\text{B.15})$$

where the indices indicate one of the contours, $k, l = 1, 2$, and the second term in the exponential comes with a minus since time runs opposite on \mathcal{C}_2 with respect to \mathcal{C}_1 .

Now we can construct the propagator for arbitrary times $t \in \mathcal{C}_1 \cup \mathcal{C}_2$, and importantly convolutions of operators thereof. Using Eq. (B.9) together with Eq. (B.10) we find

$$i\mathbf{G}(k) = i\mathbf{G}_{0F}(k) + i\mathbf{G}_{0T}(k) = \begin{pmatrix} i\mathbf{G}_{0F}(k) & \\ & -i\mathbf{G}_{0F}^\dagger(k) \end{pmatrix} - 2\pi(\not{k} + m)\delta(k^2 - m^2) \sin \Theta(k) \begin{pmatrix} \sin \Theta(k) & \cos \Theta(k) \\ \cos \Theta(k) & \sin \Theta(k) \end{pmatrix}, \quad (\text{B.16})$$

where $\sin^2 \Theta(k) = F_{FD}(\omega_k, \mu)$. Therefore one finds that the propagator becomes a 2×2 dimensional matrix at finite temperature. For instance the 11-component is given by

$$i\mathbf{G}^{(11)}(k) = (\not{k} + m) \left[\frac{i}{k^2 - m^2 + i\epsilon} - 2\pi\delta(k^2 - m^2)F_{FD}(\omega_k, \mu) \right]. \quad (\text{B.17})$$

In the limit $\beta \rightarrow \infty$ the situation simplifies since the propagator diagonalizes *i.e.* since $\cos \Theta(k) \rightarrow 0$. Furthermore, since the external states of any diagram are always fixed to be on the (real) contour \mathcal{C}_1 all one ever needs at zero temperature is

$$i\mathbf{G}^{(11)}(k) = (\not{k} + m) \left[\frac{i}{k^2 - m^2 + i\epsilon} - 2\pi\delta(k^2 - m^2)\theta(k^0)\theta(k_f - |\vec{k}|) \right] \simeq \frac{i}{l^0 + i\epsilon} - 2\pi\delta(l^0)\theta(k^0)\theta(k_f - |\vec{l}|) \quad (\text{B.18})$$

where we expanded the propagators for non-relativistic nucleons by decomposing their momenta as before $k^\mu = mv^\mu + l^\mu$.

In the above analysis, we considered the background of a single Dirac fermion. In case of nucleons, an isospin doublet, the above derivation goes through analogously with the difference that the chemical potentials of the nuclei μ_N (and therefore also their Fermi momenta in the limit $T \rightarrow 0$) are different for protons and neutrons. One finds, at finite T in the non-relativistic limit

$$iG(k) = \frac{i}{k^0 + i\epsilon} - 2\pi\delta(k^0) \left[\frac{1 + \tau^3}{2} F_{FD}(\omega, \mu_p) + \frac{1 - \tau^3}{2} F_{FD}(\omega, \mu_n) \right], \quad (\text{B.19})$$

with the proton and neutron chemical potentials μ_p and μ_n . The generalization to $T \rightarrow 0$ is straightforward.

B.2 Particle production rates

In vacuum, QFT parameters are related to observable quantities in a straightforward manner. The amplitude squared $|M|^2$ of a certain process is linked to an experimentally observable cross section σ . The matrix element M is, per construction, defined as the scattering process of n incoming asymptotic states to m outgoing asymptotic states. In thermal field theory, instead of scattering asymptotic states, we are interested in the evolution of particle distribution functions.

We are interested in the scenario where a particle, say an axion, is produced due to scattering of nucleons within the thermal bath, described by their distribution function, and then is able to free stream out of the bath. This scenario exactly describes a particle production rate. In vacuum, decay rates are related to the imaginary part of the self-energy. Similarly, the axion production rate in a nucleon density background is related to the imaginary part of the axion self-energy, see *e.g.* [120],

$$\Gamma_i(p_a) = \frac{1}{E_a} \text{Im} \Pi(p_a), \quad (\text{B.20})$$

which is given by the pole of the full propagator

$$i\mathcal{D}^{(11)}(p_a) = i\mathcal{D}(p_a) - F_{BE}(\omega_a) [i\mathcal{D}(p_a) - i\mathcal{D}^*(p_a)], \quad (\text{B.21})$$

with

$$i\mathcal{D}(p_a) = \frac{i}{p_a^2 - m_a^2 - \Pi(p_a) + i\epsilon}, \quad (\text{B.22})$$

where p_a denotes the axion momentum and $E_a = p_a^0$ its energy. The Bose-Einstein distribution F_{BE} is defined by

$$F_{BE}(\omega_k) \equiv \theta(k^0) f_{BE}(\omega_k) + \theta(-k^0) f_{BE}(-\omega_k) \quad \text{and} \quad f_{BE}(\omega_k) \equiv \frac{1}{e^{\beta\omega_k} - 1}. \quad (\text{B.23})$$

Note that without a density background, the imaginary part of the self-energy would of course vanish, *i.e.* the axion kinematically cannot decay to nucleons. Note also that as we are assuming the axion is free streaming, it has negligible density, thus the second

part of the propagator vanishes, $f_B(\omega_a) = 0^7$. The imaginary part of the self-energy gets a contribution from the (nucleon) density background.

$\Gamma_i(p_a)$ describes the production rate of axions with on-shell momentum p_a , *i.e.* the probability per time to produce an axion with momentum p_a . To obtain the production rate summed over all possible momenta, Γ , we have to integrate over the whole phase space and normalize accordingly. As p_a is on-shell and $p_a^0 > 0$, this is given by

$$d\Gamma = d\Gamma_i(p_a) \frac{V}{(2\pi)^3} d^3p_a, \quad (\text{B.24})$$

where $\int V/(2\pi)^3 d^3p_a = 1$. We are not only interested in Γ , our main goal is to calculate the axion emissivity $\dot{\epsilon}_a$ which is the emitted energy per volume and time. In other words

$$d\dot{\epsilon}_a = \frac{E_a}{VT} dP, \quad (\text{B.25})$$

whereas Γ is given is the probability per time *i.e.*

$$d\Gamma = \frac{1}{T} dP, \quad (\text{B.26})$$

and thus

$$d\dot{\epsilon}_a = \frac{E_a}{V} d\Gamma. \quad (\text{B.27})$$

Combining equations (B.20), (B.24) and (B.27) the emissivity reads

$$\dot{\epsilon}_a = \int \Gamma_i(p_a) E_a \frac{d^3p_a}{(2\pi)^3} = \int 2\text{Im}\Pi_{11}(p_a) E_a d\Pi_a, \quad (\text{B.28})$$

where we defined $d\Pi_a = d^3p_a / [(2\pi)^3 2E_a]$.

In conclusion, calculating the emissivity Eq. (B.28) boils down to calculating $\text{Im}\Pi_{11}(p_a)$ in the real-time formalism of thermal field theory, which is the problem we are going to review next.

B.3 Cutting rules at finite density

In quantum field theory in vacuum, one can use the so-called Cutkosky rules [124, 125] to calculate the imaginary part of amplitudes. One can show that twice the imaginary part of an amplitude is equal to the sum of its cuts. Cuts are nothing else than phase space integrals over internal on-shell particles. This was formulated in a systematic way in [126]. A very similar approach can be used within thermal field theory as we will review in the following.

The calculation of decay/production rates within thermal field theory was pioneered by Weldon [120] using the imaginary time formalism. Not long after, it was shown by Kobes and Semenoff [123, 127] that one can derive a set of rules along the lines of [126], which

⁷Dropping this assumption, one would need to be careful, as $\Pi(p_a)$ and the 11-component of the self-energy matrix $\Pi(p_a)_{ab}$ are non-trivially related. It can be shown (see *e.g.* [121, 123]) that $\text{Im}\Pi(p_a) = \tanh(\beta p_a^0/2) \text{Im}\Pi_{11}(p_a)$, which of course in the case of zero axion density reduces to be trivial.

simplify the calculation of the imaginary part of the self-energy function. However, it does not always provide a set of cutting rules as in the vacuum, as there are diagrams left which do not vanish and do not have a simple representation as a cut diagram.

Let us consider the cutting rules at finite density following [121, 123, 127, 128] in the case where we just have diagrams with external states of type 1 (physical states). In such a case it is sufficient to only consider internal vertices of type 1, as was shown in [121, 123, 128].

As we know from section Sec. B.1, the boson/fermion propagator is given by 2×2 matrix $i\mathbf{D}_{(ab)}/i\mathbf{G}_{(ab)}$. The components relevant in the following are for the bosons

$$i\mathbf{D}_{(11)}(p) = -i\mathbf{D}_{(22)}^*(p) = \frac{i}{p^2 - m^2 + i\epsilon} + 2\pi F_{\text{BE}}(\omega_p) \delta(p^2 - m^2), \quad (\text{B.29})$$

and we define the so-called "circled" propagators

$$i\mathbf{D}^\pm(p) = 2\pi [\theta(\pm p^0) + F_{\text{BE}}(\omega_p)] \delta(p^2 - m^2). \quad (\text{B.30})$$

For fermions the relevant expressions are

$$i\mathbf{G}_{(11)}(p) = -i\mathbf{G}_{(22)}^*(p) = \frac{i}{\not{p} - m + i\epsilon} - 2\pi(\not{p} + m)F_{\text{FD}}(\omega_p)\delta(p^2 - m^2), \quad (\text{B.31})$$

and

$$i\mathbf{G}^\pm(p) = 2\pi(\not{p} + m) [\theta(\pm p^0) - F_{\text{FD}}(\omega_p)] \delta(p^2 - m^2). \quad (\text{B.32})$$

For later convenience let us also define $\Sigma_F(p) \equiv \not{p} + m$.

We do not review the full set of rules, but only the ones needed to calculate the axion production rate at finite density. In the $T \rightarrow 0$ limit, all propagators are diagonal, simplifying the problem. The rules to obtain two times the imaginary part of any two-point function in the real-time formalism at finite density read as follows:

1. Draw all Feynman diagrams with the two corresponding external legs with all possible combinations where at least one vertex has a circle around it but at most all except one are circled.
2. Reverse the sign of each circled vertex.
3. Propagators $P_{(11)}$ connecting circled vertices are changed to $P_{(22)}$.
4. Propagators $P_{(11)}$ connecting circled and uncircled vertices are changed to the circled propagator P^+ if the momentum flows from uncircled to circled and to P^- if the momentum flows from circled to uncircled.

Further, it has been shown in [128] that diagrams with internal clusters of circled or uncircled vertices, which are not connected to an external line, vanish. Thus, we are left only with diagrams that have only type 1 vertices and the circled and uncircled vertices clustered around one of the external legs, which also has to be circled or uncircled respectively.

For self-energy functions this means that we can draw a line through the diagram with one external leg on each side, where all vertices on one side are circled and on the other side are uncircled or the other way round (see *e.g.* Figs. 17 and 18). In vacuum this mentioned "line" represents the usual on-shell cut obeying the Cutkosky rules.

Examples for such diagrams can be seen on the RHS of Figs. 17 and 18. This sets the stage for systematically calculating the axion emissivity from a SN within the real-time formalism of thermal field theory.

B.4 Axion emissivity from supernova explosions

According to the previous sections, in order to calculate the axion emissivity from a SN we have to calculate $\text{Im}\Pi_{11}(p_a)$ using the cutting rules given above. For SN environments the dominant contribution comes from diagrams where only nucleon lines are cut⁸. As diagrams with two nucleon lines are kinematically forbidden, and no diagrams with three nucleon lines cut can exist due to baryon number conservation, the leading order diagrams must have at least four nucleon lines cut. An example for such a diagram with the above rules applied is shown in Fig. 17. Applying now the rules summarized in the previous section, we find that the imaginary part of the self-energy induced by the specific diagram shown in Fig. 17 is equal to

$$\int d\Pi_1 d\Pi_2 d\Pi_3 d\Pi_4 (2\pi)^4 \delta^{(4)}(\sum_i p_i - p_a) |\mathcal{A}|^2 f_1 f_2 (1 - f_3) (1 - f_4), \quad (\text{B.33})$$

where \mathcal{A} is the matrix element of the diagram, $d\Pi_i = d^3 p_i / [(2\pi)^3 2E_i]$, and f_i is the Fermi-Dirac distribution of the i th nucleon defined in Eq. (B.8) and E_i the energy of the i th nucleon. Drawing consistently all possible diagrams at the same order, we arrive at

$$\dot{\epsilon}_a^{LO} = \int d\Pi_1 d\Pi_2 d\Pi_3 d\Pi_4 d\Pi_a (2\pi)^4 S |\mathcal{M}^{LO}|^2 \delta^{(4)}(\sum_i p_i - p_a) E_a f_1 f_2 (1 - f_3) (1 - f_4), \quad (\text{B.34})$$

where \mathcal{M}^{LO} is the sum of all possible tree-level OPE diagrams shown in figure Fig. 16. This shows that the emissivity obtained in [12] follows directly from the imaginary part of the self-energy of the axion propagator within the real-time formalism of thermal quantum field theory.

At next higher order, which in the language of self-energy diagrams means to add a $\nu = 1$ vertex instead of a $\nu = 0$ one. Going another order higher, we can add another loop as shown on the left-hand side of Fig. 18. Applying the above rules leads to the conclusion that this is equal to multiplying the complex conjugate of the tree-level diagram with the 1-loop diagram, as shown on the right-hand side of Fig. 18, and integrate over the same phase space as in the example before. Thus, as one would expect, the leading order result is equivalent to calculating the corresponding matrix element at leading order in (vacuum) QFT, averaging over incoming momenta and summing over outgoing momenta, both subject to the corresponding particle distribution functions. However, at higher order,

⁸If the pion density during the supernova is large, a diagram where one pion line is cut might also be important or even dominant, leading to the process discussed in [129]

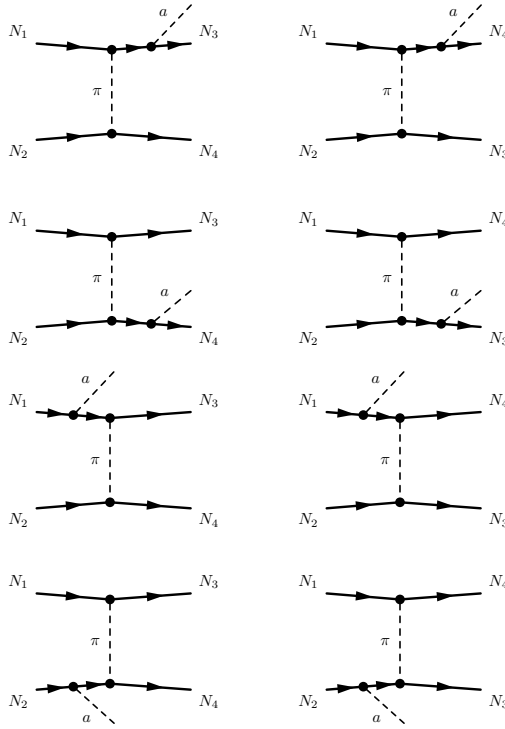


Figure 16: OPE diagrams contributing at leading order to the axion emissivity from SN.

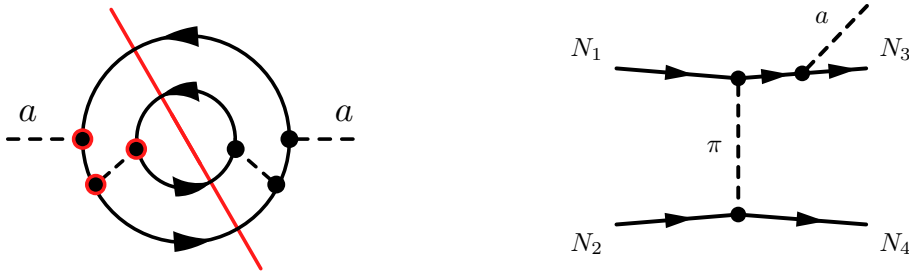


Figure 17: The left figure shows the self energy diagram whose imaginary part corresponds to the emissivity of the example OPE diagram \mathcal{A} on the right hand side.

density insertions become important and the result starts deviating from the corresponding vacuum calculation.

Thus, denoting by $|\mathcal{M}|^2 = |\mathcal{M}^{LO} + \mathcal{M}^{NLO} + \dots|^2$ the squared sum of all diagrams, the full emissivity is given by

$$\dot{\epsilon}_a = \int d\Pi_1 d\Pi_2 d\Pi_3 d\Pi_4 d\Pi_a (2\pi)^4 S |\mathcal{M}|^2 \delta^{(4)}(\sum_i p_i - p_a) E_a f_1 f_2 (1 - f_3) (1 - f_4). \quad (\text{B.35})$$

As discussed in Sec. 4.1, in order to systematically calculate the axion emissivity from a SN at one loop order, one would, in principle, have to include all possible one loop diagrams of the process $N + N \rightarrow N + N + a$, which we leave for future work. As a first step, however,

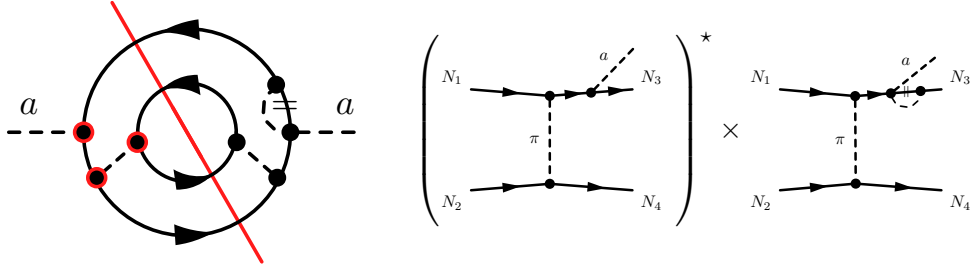


Figure 18: The left figure shows the self-energy diagram whose imaginary part corresponds to the emissivity of the product of the two diagrams shown on the right-hand side.

we include in this work all the diagrams correcting the nucleon-axion vertex at 1-loop order in finite density and relevant terms from the nucleon contact interaction.

C Explicit loop calculations

C.1 Useful integrals

In this appendix, we want to summarize the integrals needed to evaluate the diagrams contribution to the axion form factor.

C.1.1 Integrals for vacuum form factor

For the vacuum loops, the following standard integrals defined in [69] are needed

$$\Delta_\pi = -\frac{1}{i} \int \frac{d^d k}{(2\pi)^d} \frac{1}{k^2 - m_\pi^2 + i\eta} = 2m_\pi^2 \left(L(\lambda) + \frac{1}{(4\pi)^2} \ln \frac{m_\pi}{\lambda} \right) + \mathcal{O}(d-4), \quad (\text{C.1})$$

$$L(\lambda) = \frac{\lambda^{d-4}}{(4\pi)^2} \left(\frac{1}{d-4} - \frac{1}{2} [\ln(4\pi) + \Gamma'(1) + 1] \right), \quad (\text{C.2})$$

and

$$\frac{1}{i} \int \frac{d^d k}{(2\pi)^d} \frac{\{1, k_\mu, k_\mu k_\nu\}}{(k^2 - m_\pi^2 + i\eta)(\omega - v \cdot k + i\eta)} = \{J_0(\omega), v_\mu J_1(\omega), g_{\mu\nu} J_2(\omega) + v_\mu v_\nu J_3(\omega)\}, \quad (\text{C.3})$$

where

$$\begin{aligned} J_0(\omega) &= -4\omega L + \frac{2\omega}{(4\pi)^2} \left(1 - 2 \ln \frac{m_\pi}{\lambda} \right) - \frac{1}{8\pi^2} \frac{m_\pi^3}{(m_\pi^2 - \omega^2)} F \left(\frac{-\omega}{m_\pi} \right) + \mathcal{O}(d-4), \\ J_1(\omega) &= \omega J_0(\omega) + \Delta_\pi, \\ J_2(\omega) &= \frac{1}{d-1} [(m_\pi^2 - \omega^2) J_0(\omega) - \omega \Delta_\pi], \\ J_3(\omega) &= \omega J_1(\omega) - J_2(\omega). \end{aligned} \quad (\text{C.4})$$

Here we defined

$$F(x) = -(x^2 - 1 + i\varepsilon)^{3/2} \left[\log \left(x - \sqrt{x^2 - 1 + i\varepsilon} \right) - \log \left(x + \sqrt{x^2 - 1 + i\varepsilon} \right) \right], \quad (\text{C.5})$$

with $\varepsilon \rightarrow 0$ and $\epsilon > 0$, in order to properly account for the imaginary part of the loop integrals above the pion productions threshold $\omega > m_\pi$.

C.1.2 Integrals for finite density form factor

At finite density, the relevant standard integrals, given in [130, 131], read

$$\Gamma_0(m_\pi, |\vec{p}|) = \int_0^{k_f} dk \int_{-1}^1 dx \frac{k^2}{m_\pi^2 + |\vec{p}|^2 + k^2 + 2|\vec{p}|kx}, \quad (\text{C.6a})$$

$$\Gamma_1(m_\pi, |\vec{p}|) = \int_0^{k_f} dk \int_{-1}^1 dx \frac{k^3 x / |\vec{p}|}{m_\pi^2 + |\vec{p}|^2 + k^2 + 2|\vec{p}|kx}, \quad (\text{C.6b})$$

$$\Gamma_2(m_\pi, |\vec{p}|) = \int_0^{k_f} dk \int_{-1}^1 dx \frac{k^4 (1 - x^2) / 2}{m_\pi^2 + |\vec{p}|^2 + k^2 + 2|\vec{p}|kx}, \quad (\text{C.6c})$$

$$\Gamma_3(m_\pi, |\vec{p}|) = \int_0^{k_f} dk \int_{-1}^1 dx \frac{k^4 (3x^2 - 1) / (2|\vec{p}|^2)}{m_\pi^2 + |\vec{p}|^2 + k^2 + 2|\vec{p}|kx}. \quad (\text{C.6d})$$

Evaluating the integrals, they read as

$$\Gamma_0(m_\pi, |\vec{p}|) = k_f - m_\pi \left[\tan^{-1} \frac{k_f + |\vec{p}|}{m_\pi} + \tan^{-1} \frac{k_f - |\vec{p}|}{m_\pi} \right] + \frac{m_\pi^2 + k_f^2 - |\vec{p}|^2}{4|\vec{p}|} \log \frac{m_\pi^2 + (k_f + |\vec{p}|)^2}{m_\pi^2 + (k_f - |\vec{p}|)^2} \quad (\text{C.7a})$$

$$\begin{aligned} \Gamma_1(m_\pi, |\vec{p}|) &= \frac{k_f}{4|\vec{p}|^2} (m_\pi^2 + k_f^2 + |\vec{p}|^2) - \Gamma_0(|\vec{p}|) \\ &\quad - \frac{1}{16|\vec{p}|^3} \left[m_\pi^2 + (k_f + |\vec{p}|)^2 \right] \left[m_\pi^2 + (k_f - |\vec{p}|)^2 \right] \log \frac{m_\pi^2 + (k_f + |\vec{p}|)^2}{m_\pi^2 + (k_f - |\vec{p}|)^2}, \end{aligned} \quad (\text{C.7b})$$

$$\Gamma_2(m_\pi, |\vec{p}|) = \frac{k_f^3}{9} + \frac{1}{6} (k_f^2 - m_\pi^2 - |\vec{p}|^2) \Gamma_0(|\vec{p}|) + \frac{1}{6} (m_\pi^2 + k_f^2 - |\vec{p}|^2) \Gamma_1(|\vec{p}|), \quad (\text{C.7c})$$

$$\Gamma_3(m_\pi, |\vec{p}|) = \frac{k_f^3}{3|\vec{p}|^2} - \frac{m_\pi^2 + k_f^2 + |\vec{p}|^2}{2|\vec{p}|^2} \Gamma_0(|\vec{p}|) - \frac{m_\pi^2 + k_f^2 + 3|\vec{p}|^2}{2|\vec{p}|^2} \Gamma_1(|\vec{p}|). \quad (\text{C.7d})$$

For the calculation provided in Sec. 3.2.1 and App. C.3 it additionally turns out to be useful to define

$$I_1(m_\pi, \vec{p}, \vec{q}) = \int_0^{k_f} \frac{d^3 k}{(2\pi)^3} \frac{\vec{\sigma} \cdot (\vec{k} + \vec{p}) \vec{q} \cdot (\vec{k} + \vec{p})}{m_\pi^2 + (\vec{k} + \vec{p})^2} \quad (\text{C.8a})$$

$$= \frac{1}{4\pi^2} [(\vec{\sigma} \cdot \vec{q}) \Gamma_2(m_\pi, |\vec{p}|) + (\vec{\sigma} \cdot \vec{p}) (\vec{q} \cdot \vec{p}) (\Gamma_0(m_\pi, |\vec{p}|) + 2\Gamma_1(m_\pi, |\vec{p}|) + \Gamma_3(m_\pi, |\vec{p}|))],$$

$$I_2(m_\pi, \vec{p}) = \int_0^{k_f} \frac{d^3 k}{(2\pi)^3} \frac{(\vec{k} + \vec{p}) \cdot (\vec{k} + \vec{p})}{m_\pi^2 + (\vec{k} + \vec{p})^2} = \frac{1}{4\pi^2} \left(\frac{2k_f^3}{3} - m_\pi^2 \Gamma_0(m_\pi, |\vec{p}|) \right), \quad (\text{C.8b})$$

$$I_3(m_\pi, \vec{p}) = \int_0^{k_f} \frac{d^3 k}{(2\pi)^3} \frac{\vec{\sigma} \cdot (\vec{k} + \vec{p})}{m_\pi^2 + (\vec{k} + \vec{p})^2} = (\vec{\sigma} \cdot \vec{p}) \frac{1}{4\pi^2} (\Gamma_1(m_\pi, |\vec{p}|) + \Gamma_0(m_\pi, |\vec{p}|)). \quad (\text{C.8c})$$

To further simplify the notation in the main text we define the following expressions

$$G_1^N(\vec{p}, \vec{p}_a) = \frac{1}{16|\vec{p}_a|} \left[(\vec{\sigma} \cdot \vec{p}_a) I_2^N(m_\pi, \vec{p}) - 2 I_1^N(m_\pi, \vec{p}, \vec{p}_a) - \left\{ \begin{array}{l} m_\pi \rightarrow \tilde{m}_\pi \\ \vec{p} \rightarrow \vec{p} + \vec{p}_a \end{array} \right\} \right], \quad (\text{C.9a})$$

$$G_2^N(\vec{p}, \vec{p}_a) = \frac{1}{4|\vec{p}_a|} [I_3^N(m_\pi, \vec{p}) + I_3^N(\tilde{m}_\pi, \vec{p} + \vec{p}_a)], \quad (\text{C.9b})$$

$$G_3^N(\vec{p}, \vec{p}_a) = \frac{1}{2} [I_1^N(\tilde{m}_\pi, \vec{p} + \vec{p}_a, \vec{p}_a) + I_1^N(m_\pi, \vec{p}, \vec{p}_a) - (\vec{\sigma} \cdot \vec{p}_a)(I_2^N(\tilde{m}_\pi, \vec{p} + \vec{p}_a) + I_2^N(m_\pi, \vec{p}))], \quad (\text{C.9c})$$

$$G_4^N(\vec{p}, \vec{p}_a) = \frac{1}{2} [I_1^N(\tilde{m}_\pi, \vec{p} + \vec{p}_a, \vec{p}_a) + I_1^N(m_\pi, \vec{p}, \vec{p}_a) - |\vec{p}_a|^2 I_3^N(\tilde{m}_\pi, \vec{p} + \vec{p}_a)], \quad (\text{C.9d})$$

with $N = \{p, n\}$.

C.2 Loop corrections in vacuum

The loop diagrams at chiral order $\nu = 2$ given in Fig. 1 have been calculated in [81]. The first two diagrams both vanish,

$$(a_1) = (a_2) = 0. \quad (\text{C.10})$$

For the third diagram in Fig. 1 we find

$$(b) = \frac{2g_A c_{u-d} m_\pi^2}{f_a f_\pi^2} \tau^3 \left(L(\lambda) + \frac{1}{(4\pi)^2} \ln \frac{m_\pi}{\lambda} \right) S \cdot p_a, \quad (\text{C.11})$$

which agrees with [81] up to a typo. On the other hand, for the loop diagram (c) we find

$$(c) = \frac{\hat{c}_N g_A^2}{f_a f_\pi^2} \left(\frac{D-3}{4} \right) \frac{1}{v \cdot p_a} (J_2(0) - J_2(v \cdot p_a)) S \cdot p_a. \quad (\text{C.12})$$

where $D = 4 - 2\epsilon$ in dimensional regularization. In [81], they find $1/4$ instead of the factor $(D-3)/4$, which we believe is necessary in dimensional regularization to obtain the correct finite contributions. Renormalizing these diagrams appropriately by adding the counterterms given in diagram (d), we arrive at the result given in the main text in Eq. (3.6) and following.

Following the nomenclature of Fig. 2 we calculate the two non-vanishing one loop diagrams, (e₁) and (e₂), and give the results in terms of the standard integrals defined in App. C.1.

We find the results for the loop diagrams to be given by

$$(e_1) = \left(\frac{g_A c_{u-d}}{f_\pi^2 f_a \Lambda} \right) (c_3 - 2c_4) \tau^3 \vec{\sigma} \cdot \vec{p}_a J_2(v \cdot p_a), \quad (\text{C.13})$$

as well as

$$(e_2) = \left(\frac{g_A c_{u-d}}{f_\pi^2 f_a \Lambda} \right) (c_3 - 2c_4) \tau^3 \vec{\sigma} \cdot \vec{p}_a J_2(0). \quad (\text{C.14})$$

Summing them up and expanding the standard integrals leads to

$$\begin{aligned}
(e_1) + (e_2) &= -\frac{2g_A c_{u-d}}{f_a f_\pi^2} (\hat{c}_3 - 2\hat{c}_4) \tau^3 [J_2(v \cdot p_a) + J_2(0)] S \cdot p_a \\
&= -\frac{4g_A c_{u-d}}{3f_a f_\pi^2} (\hat{c}_3 - 2\hat{c}_4) \tau^3 \left\{ \frac{1}{16\pi^2} \left[m_\pi^2 (v \cdot p_a) - (v \cdot p_a)^3 - m_\pi^2 F\left(\frac{-v \cdot p_a}{m_\pi}\right) - m_\pi^2 F(0) \right] \right. \\
&\quad \left. - \Lambda(\lambda) (3m_\pi^2 (v \cdot p_a) - 2((v \cdot p_a))^3) \right\} S \cdot p_a.
\end{aligned} \tag{C.15}$$

Here $\Lambda(\lambda)$ is a function collecting the scale-dependent and divergent pieces in dimensional regularization given by

$$\Lambda(\lambda) = L(\lambda) + \frac{1}{16\pi^2} \log \frac{m_\pi}{\lambda}. \tag{C.16}$$

As described in the main text, we neglect all contributions that are not Δ -enhanced, *i.e.* not coming from \hat{c}_3 or \hat{c}_4 at this loop order and thus drop the \hat{c}_9 as well as \hat{c}_2 which is in principle Δ -enhanced but turns out to be kinematically suppressed.

C.2.1 Renormalization

In order to arrive at the result at Eq. (3.11), we renormalized the divergent pieces with terms at $\Delta = 3$ given by [82]

$$e_{117}(\lambda) \bar{N} (\langle \chi_+ \rangle S \cdot u i v \cdot D + \text{h.c.}) N, \tag{C.17}$$

$$e_{193}(\lambda) \bar{N} (S \cdot u i (v \cdot D)^3 + \text{h.c.}) N, \tag{C.18}$$

which give rise to the following tree level contributions

$$-\frac{4e_{117}}{f_a} c_{u-d} \tau^3 m_\pi^2 (v \cdot p_a) S \cdot p_a, \tag{C.19}$$

$$\frac{e_{193}}{f_a} c_{u-d} \tau^3 (v \cdot p_a)^3 S \cdot p_a. \tag{C.20}$$

As one can easily check this renormalizes the loop contribution if the beta functions

$$e_i(\lambda) = \bar{e}_i + \frac{\beta_i}{f_\pi^2} \Lambda(\lambda), \tag{C.21}$$

have the following property

$$\beta_{117} \supset g_A (\hat{c}_3 - 2\hat{c}_4), \tag{C.22}$$

$$\beta_{193} \supset \frac{8g_A}{3} (\hat{c}_3 - 2\hat{c}_4), \tag{C.23}$$

which exactly agrees with [82]. Note that the function collecting the divergent and scale-dependent pieces is given by

$$\Lambda(\lambda) = L(\lambda) + \frac{1}{16\pi^2} \log \frac{m_\pi}{\lambda}, \tag{C.24}$$

with $L(\lambda)$ given in Eq. (C.2). Note that as is customary in HBChPT, instead of the usual $\overline{\text{MS}}$ scheme, we use the modified $\widetilde{\text{MS}}$ scheme [62]. A priori there are finite pieces which however are zero for operators that can be eliminated by an appropriate field redefinition (proportional to $v \cdot D$), see *e.g.* [132].

C.3 Density corrections

The relevant non-vanishing vertex diagrams at order $\nu = 2$ and $\nu = 3$ are the ones shown in Fig. 6 and Fig. 7. We calculate them explicitly in the following first in the case of isospin symmetric nuclear matter and then in the case of arbitrarily mixed matter and give the results in terms of the standard integrals defined in C.1.

C.3.1 Isospin symmetric matter

In this section, we explicitly calculate some of the diagrams shown in Fig. 6 and Fig. 7 in the isospin symmetric limit and give the results for the others. In the isospin symmetric case, the propagator is given by Eq. (3.28). Let us consider the diagrams $(h_1) + (h_2)$ as an example. The ansatz for two loop integrals reads

$$(h_1) + (h_2) = \int \frac{d^4k}{(2\pi)^4} \left[-\frac{g_A}{2f_\pi} \vec{\sigma} \cdot (\vec{k} - \vec{p}) \tau^a \right] \left[\frac{i}{k^0} - 2\pi\delta(k^0)\theta(k_f - |\vec{k}|) \right] \left[\frac{c_N}{2f_a} \vec{\sigma} \cdot \vec{p}_a \right] \\ \times \left[\frac{i}{k^0 + p_a^0} - 2\pi\delta(k^0 + p_a^0)\theta(k_f - |\vec{k} + \vec{p}_a|) \right] \left[\frac{g_A}{2f_\pi} \vec{\sigma} \cdot (\vec{k} - \vec{p}) \tau^b \right] \left[\frac{-i\delta^{ab}}{m_\pi^2 - (k-p)^2} \right]. \quad (\text{C.25})$$

Taking care of the spin as well as the isospin structures and only keeping the density-dependent part (we already calculated the vacuum loop in diagram in App. C.2) leaves us, after simplifying and evaluating the k^0 integrals over the δ functions, with

$$(h_1) + (h_2) = \left(\frac{g_A^2 \hat{c}_N}{8f_\pi^2 f_a} \right) \frac{1}{p_a^0} \int_0^{k_f} \frac{d^3k}{(2\pi)^3} \left\{ \left[\frac{2\vec{\sigma} \cdot (\vec{k} - \vec{p}) \vec{p}_a \cdot (\vec{k} - \vec{p}) - \vec{\sigma} \cdot \vec{p}_a (\vec{k} - \vec{p})^2}{\tilde{m}_\pi^2 + (\vec{k} - \vec{p})^2} \right] \right. \\ \left. - \left[\frac{2\vec{\sigma} \cdot (\vec{k} - \vec{p} - \vec{p}_a) \vec{p}_a \cdot (\vec{k} - \vec{p} - \vec{p}_a) - \vec{\sigma} \cdot \vec{p}_a (\vec{k} - \vec{p} - \vec{p}_a)^2}{\tilde{m}_\pi^2 + (\vec{k} - \vec{p} - \vec{p}_a)^2} \right] \right\}, \quad (\text{C.26})$$

where we used that $m_\pi^2 - (k-p_a)^2 \simeq \tilde{m}_\pi^2 + (\vec{k} - \vec{p}_a)^2$, since $k_0 \sim \vec{k}^2/2m_N \ll |\vec{k}|$ and defined $\tilde{m}_\pi^2 = m_\pi^2 - (p_a^0)^2$. With the help of the standard integrals defined in App. C.1 we arrive at the final result

$$(h_1) + (h_2) = - \left(\frac{g_A^2 \hat{c}_N}{8f_\pi^2 f_a} \right) \frac{1}{|\vec{p}_a|} \left[2 [I_1(\tilde{m}_\pi, \vec{p} + \vec{p}_a, \vec{p}_a) - I_1(m_\pi, \vec{p}, \vec{p}_a)] \right. \\ \left. - (\vec{\sigma} \cdot \vec{p}_a) [I_2(\tilde{m}_\pi, \vec{p} + \vec{p}_a) - I_2(m_\pi, \vec{p})] \right]. \quad (\text{C.27})$$

The calculation of the diagrams (g_1) and (g_2) is very similar and yields

$$(g_1) = -\frac{c_u - d g_A p_a^0}{2f_\pi^2 f_a} \tau^3 I_3(\tilde{m}_\pi, \vec{p} + \vec{p}_a), \quad (\text{C.28a})$$

$$(g_2) = -\frac{c_u - d g_A p_a^0}{2f_\pi^2 f_a} \tau^3 I_3(m_\pi, \vec{p}). \quad (\text{C.28b})$$

For the diagrams at $\nu = 3$ we have different different vertices contribution to the same diagram, therefore we split up the calculation for the diagram into parts. Further, the

diagrams shown in Fig. 7 are not the only non-vanishing ones, as mentioned in the main text, and are shown in Fig. 19. For diagram (i_1) we find

$$\begin{aligned}
(i_1) = & + \left(\frac{g_A c_{u-d} c_3}{f_\pi^2 f_a \Lambda_\chi} \right) \tau^3 [I_1(\tilde{m}_\pi, \vec{p} + \vec{p}_a, \vec{p}_a) - |\vec{p}_a|^2 I_3(\tilde{m}_\pi, \vec{p} + \vec{p}_a)] \\
& + \left(\frac{3g_A c_9 c_{u+d}}{2f_\pi^2 f_a \Lambda_\chi} \right) [I_1(\tilde{m}_\pi, \vec{p} + \vec{p}_a, \vec{p}_a) - |\vec{p}_a|^2 I_3(\tilde{m}_\pi, \vec{p} + \vec{p}_a)] \\
& + \left(\frac{g_A c_{u-d} c_4}{f_\pi^2 f_a \Lambda_\chi} \right) \tau^3 [I_1(\tilde{m}_\pi, \vec{p} + \vec{p}_a, \vec{p}_a) - (\vec{\sigma} \cdot \vec{p}_a) I_2(\tilde{m}_\pi, \vec{p} + \vec{p}_a)] \\
& - \left(\frac{6g_A c_5 g_A^2 f_a}{f_\pi^4 \Lambda_\chi} \right) I_3(\tilde{m}_\pi, \vec{p} + \vec{p}_a),
\end{aligned} \tag{C.29}$$

and for diagram (i_2) we obtain

$$\begin{aligned}
(i_2) = & + \left(\frac{g_A c_{u-d} c_3}{f_\pi^2 f_a \Lambda_\chi} \right) \tau^3 I_1(m_\pi, \vec{p}, \vec{p}_a) + \left(\frac{3g_A c_9 c_{u+d}}{2f_\pi^2 f_a \Lambda_\chi} \right) I_1(m_\pi, \vec{p}, \vec{p}_a) \\
& + \left(\frac{g_A c_{u-d} c_4}{f_\pi^2 f_a \Lambda_\chi} \right) \tau^3 [I_1(m_\pi, \vec{p}, \vec{p}_a) - (\vec{\sigma} \cdot \vec{p}_a) I_2(m_\pi, \vec{p})] + \left(\frac{6g_A c_5 g_A^2 f_a}{f_\pi^4 \Lambda_\chi} \right) I_3(m_\pi, \vec{p}).
\end{aligned} \tag{C.30}$$

C.3.2 Arbitrarily mixed matter

For an arbitrary matter configuration, we also need vertex corrections where the nucleon propagator is altered as

$$-2\pi\delta(k_0)\theta(k_f - |\vec{k}|) \rightarrow -2\pi\delta(k_0)\theta(k_f - |\vec{k}|)\tau^3, \tag{C.31}$$

Together with the above results, we can then construct the full vertex corrections for arbitrary mixed matter using Eq. (3.25). Substituting the propagator as in Eq. (C.31) and defining $\tilde{c}_N = 3g_A c_{u-d} \mathbb{1} - g_0 c_{u+d} \tau_3$ leads to:

$$(g_1) + (g_2) \rightarrow \left(\frac{c_{u-d} g_A}{2f_\pi^2 f_a} \right) |\vec{p}_a| [I_3(m_\pi, \vec{p}) + I_3(\tilde{m}_\pi, \vec{p} + \vec{p}_a)]. \tag{C.32}$$

$$\begin{aligned}
(h_1) + (h_2) \rightarrow & - \left(\frac{g_A^2 \tilde{c}_N}{8f_\pi^2 f_a} \right) \frac{1}{|\vec{p}_a|} [2(I_1(\tilde{m}_\pi, \vec{p} + \vec{p}_a, \vec{p}_a) - I_1(m_\pi, \vec{p}, \vec{p}_a)) \\
& - (\vec{\sigma} \cdot \vec{p}_a) (I_2(\tilde{m}_\pi, \vec{p} + \vec{p}_a) - I_2(m_\pi, \vec{p}))].
\end{aligned} \tag{C.33}$$

$$\begin{aligned}
(i_1) \rightarrow & \left(\frac{g_A c_{u-d} c_3}{f_\pi^2 f_a \Lambda_\chi} \right) [I_1(\tilde{m}_\pi, \vec{p} + \vec{p}_a, \vec{p}_a) - |\vec{p}_a|^2 I_3(\tilde{m}_\pi, \vec{p} + \vec{p}_a)] \\
& - \left(\frac{g_A c_9 c_{u+d}}{2f_\pi^2 f_a \Lambda_\chi} \right) \tau^3 [I_1(\tilde{m}_\pi, \vec{p} + \vec{p}_a, \vec{p}_a) - |\vec{p}_a|^2 I_3(\tilde{m}_\pi, \vec{p} + \vec{p}_a)] \\
& - \left(\frac{g_A c_{u-d} c_4}{f_\pi^2 f_a \Lambda_\chi} \right) [I_1(\tilde{m}_\pi, \vec{p} + \vec{p}_a, \vec{p}_a) - (\vec{\sigma} \cdot \vec{p}_a) I_2(\tilde{m}_\pi, \vec{p} + \vec{p}_a)] \\
& + \left(\frac{6g_A c_5 g_A^2 f_a}{f_\pi^4 \Lambda_\chi} \right) \tau^3 I_3(\tilde{m}_\pi, \vec{p} + \vec{p}_a)
\end{aligned} \tag{C.34}$$

$$\begin{aligned}
(i_2) \rightarrow & \left(\frac{g_A c_u - d c_3}{f_\pi^2 f_a \Lambda_\chi} \right) I_1(m_\pi, \vec{p}, \vec{p}_a) - \left(\frac{g_A c_9 c_{u+d}}{2 f_\pi^2 f_a \Lambda_\chi} \right) \tau^3 I_1(m_\pi, \vec{p}, \vec{p}_a) \\
& - \left(\frac{g_A c_u - d c_4}{f_\pi^2 f_a \Lambda_\chi} \right) [I_1(m_\pi, \vec{p}, \vec{p}_a) - \vec{\sigma} \cdot \vec{p}_a I_2(m_\pi, \vec{p})] - \left(\frac{6 g_A c_5 g_A^2 f_a}{f_\pi^4 \Lambda_\chi} \right) \tau^3 I_3(m_\pi, \vec{p})
\end{aligned} \tag{C.35}$$

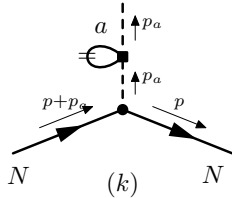


Figure 19: Additional 1-loop finite density diagram contributing at chiral order $\nu = 3$ which is not Δ enhanced and therefore neglected. This can be matched to the effect considered in [27] coming from the medium-modified axion pion mixing angle.

For completeness, we also calculate the diagram shown in Fig. 19. This gives rise to a medium-modified axion pion mixing and yields

$$(k) = \left(\frac{4 k_f^3 g_A c_5 f_a g_A^2}{3 \pi^2 m_\pi^2 f_\pi^4 \Lambda_\chi} \right) \tau^3 (\vec{\sigma} \cdot \vec{p}_a). \tag{C.36}$$

As it is not Δ enhanced, it is not included in our calculation. However, it has been included in the estimates given in [27]. Note also that this effect is important for a model-independent bound on the QCD axion [76].

Combining these results and the ones for symmetric matter above, we can assemble the density corrections for an arbitrary mixture of matter. In arbitrary matter, the propagator is given by Eq. (3.25), *i.e.* a combination of either the propagator with the identity matrix used in the section for symmetric matter and the one where the substitution Eq. (C.31) has been made which we used here.

C.4 DFSZ axion additional results

Here we show additional results for the DFSZ axion for different values of $\sin^2 \beta$ as well as for pure neutron matter. For readability, these figures are not shown in the main text. In Fig. 20, we show the momentum dependence of the DFSZ axion-nucleon coupling for $\sin^2 \beta = 0.1$ and $\sin^2 \beta = 1/2$ respectively. In Fig. 21 we show the results for the axion neutron and axion proton coupling in mixed matter for the DFSZ axion with $\sin^2 \beta = 1/2$, while in Fig. 22 we show the axion neutron coupling for $\sin^2 \beta = 0.1$ as well as $\sin^2 \beta = 1/2$ pure neutron matter.

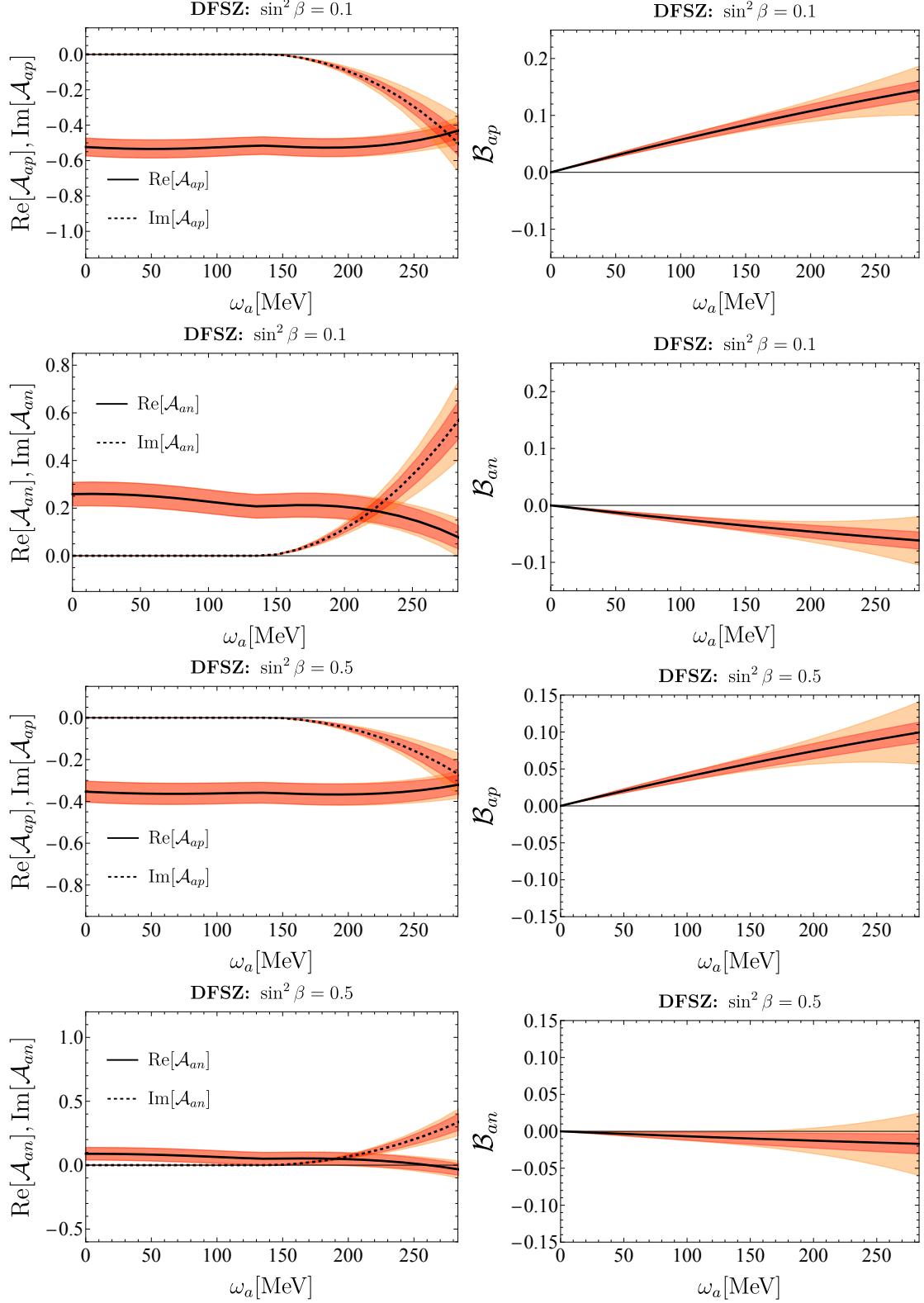


Figure 20: Momentum dependence of the DFSZ for $\sin^2 \beta = 0.1$ and $\sin^2 \beta = 0.5$ axion-nucleon couplings. Error bars are shown as in Fig. 5. At $\omega_a \sim m_\pi$ one can again see the pion production threshold, at which the coupling also gets an imaginary part.

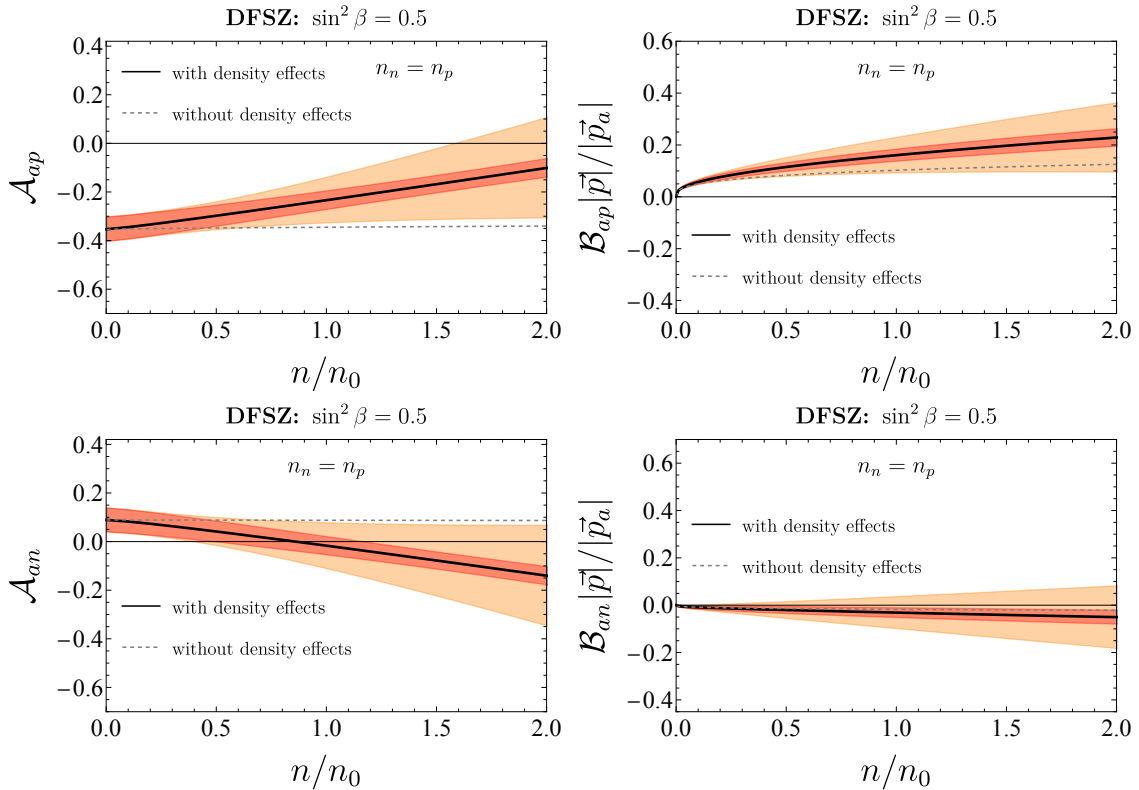


Figure 21: Density dependence of the DFSZ axion-nucleon couplings with $\sin^2 \beta = 1/2$ in symmetric nuclear matter as a function of density in units of nuclear saturation density n_0 . Error bars are shown as in Fig. 5. The gray dashed line again shows the results of Eq. (3.33)

D Temperature corrections

So far, when talking about finite density loop corrections presented in Sec. 3.2, we neglected finite temperature effects. In the following we verify that in the environments we consider, neglecting the temperature dependence in the propagator is indeed a good approximation. Note, however, that while temperature corrections in the propagator are not important, temperature changes the momentum scale at which the form factors have to be evaluated. We show below that this effect, which, of course, was taken into account in Sec. 4.1, is indeed non-negligible.

As explained in App. B.1, when the temperature is not set to zero, the 11-component of the nucleon propagator in the non-relativistic limit is given by Eq. (B.19). When evaluating the resulting diagrams at finite temperature, occurring standard integrals, defined in Eq. (C.6), can be numerically evaluated once the Fermi surface is smeared out. Doing so for typical SN temperatures $T \lesssim 50$ MeV one finds only small changes compared to the zero temperature case. These are within the uncertainties of the low energy constants summarized in Table 2. As an example, we show in Fig. 23 the effect of temperature cor-

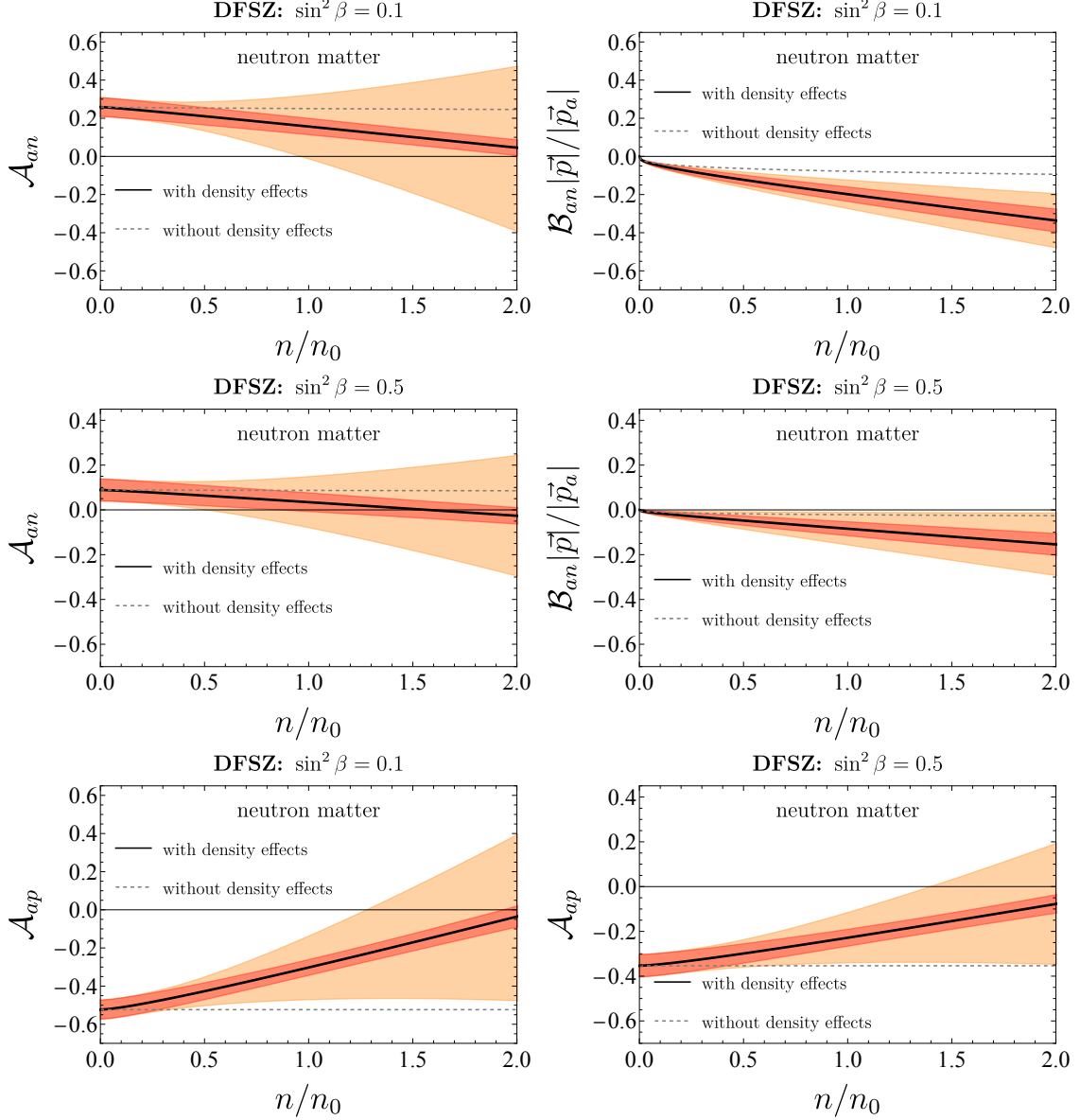


Figure 22: Density dependence of the DFSZ axion-nucleon couplings with $\sin^2 \beta = 0.1$ (upper panel) as well as $\sin^2 \beta = 1/2$ (lower panel) in neutron matter as a function of density in units of nuclear saturation density n_0 . Error bars are shown as in Fig. 5. The gray dashed line again shows the results of Eq. (3.33).

rections to axion-nucleon couplings for the KSVZ model in symmetric nuclear matter for $T = 10$ MeV and $T = 50$ MeV. We conclude that, to a good approximation, we can neglect finite temperature corrections to the nucleon propagator at typical SN temperatures and densities.

However, the momenta at which the form factors \mathcal{A}_{aN} and \mathcal{B}_{aN} are evaluated when calculating the axion emissivity, see Eq. (4.1), heavily depend on the temperature as the variance of the Fermi-Dirac distribution f_i occurring in the emissivity roughly goes as

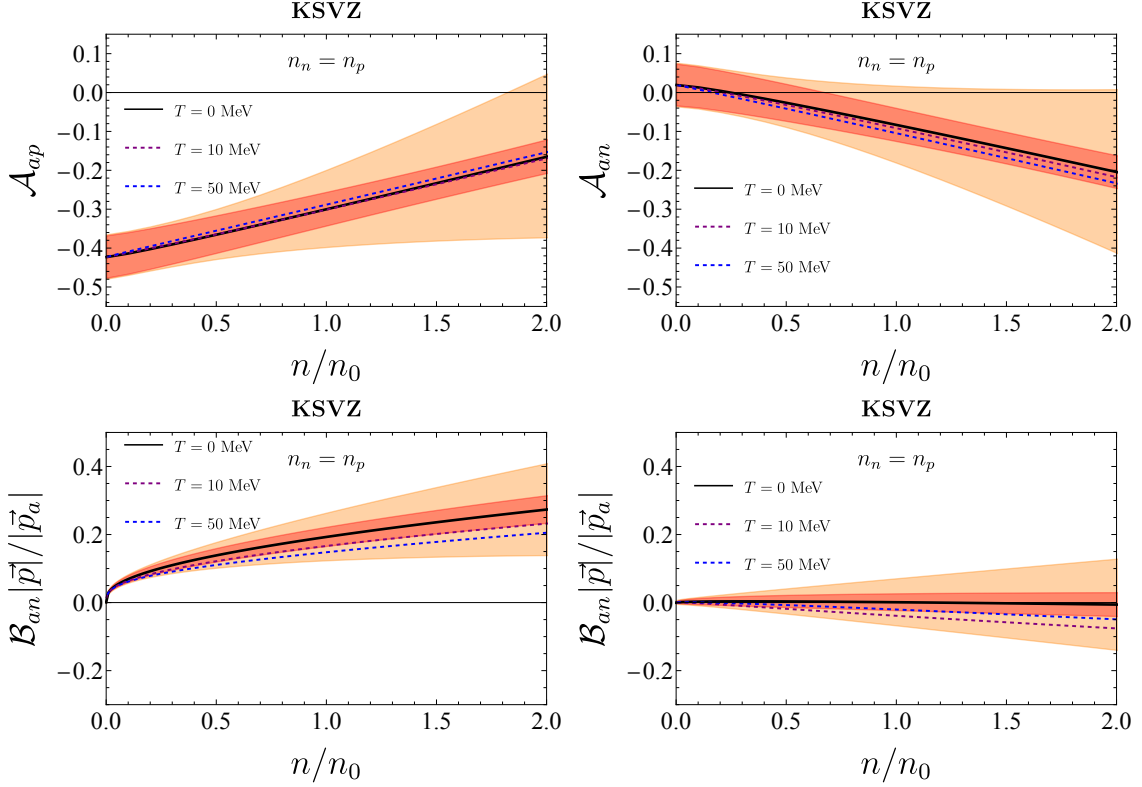


Figure 23: Density dependence of the KSVZ axion-nucleon couplings in isospin symmetric nuclear matter as a function of density in units of nuclear saturation density n_0 for different temperatures T . Error bars are shown as in Fig. 5. The black solid line is, as in Fig. 8, the mean value for $T = 0$. The two dashed lines are the mean values for $T = 10$ MeV (green line) and $T = 50$ MeV (purple line).

$\sim \sqrt{3m_N T}$. This temperature dependence is what we are studying in the following.

We calculate the expectation value of the form factors $\mathcal{A}(p, k_f^{p/n}, p_a)$ and $\mathcal{B}(p, k_f^{p/n}, p_a)$ which we define by

$$\langle \mathcal{A} \rangle \equiv \mathcal{N} \int \left(\prod_i d\Pi_i \right) d\Pi_a \mathcal{A}(p, k_f^{p/n}, p_a) \delta^{(4)}(\sum_i p_i - p_a) f_1 f_2 (1 - f_3) (1 - f_4), \quad (\text{D.1})$$

using the same integration kernel and, therefore, also kinematics as in Eq. (4.1). Here \mathcal{N} is a normalization constant defined such that $\langle \mathcal{A} \rangle = 1$ for $\mathcal{A} = 1$. We choose a value for T and scan over values for densities n up to $2n_0$, where the corresponding value of the chemical potential μ for each case is determined from the relation

$$n(\mu, T) = 4 \int \frac{d^3 k}{(2\pi)^3} f_{\text{FD}}(k, \mu, T). \quad (\text{D.2})$$

We evaluate Eq. (D.1) for the momentum the form factor depends on $p = p_{1/2}$ being an incoming momentum (as this leads to the strongest effect) at the two temperatures $T = 20$ MeV and $T = 40$ MeV, which we show in Fig. 24. One can clearly see that this

temperature dependence cannot be neglected and is included in the calculation of the axion emissivity from SN in Sec. 4.1 as can also be seen from Fig. 14.

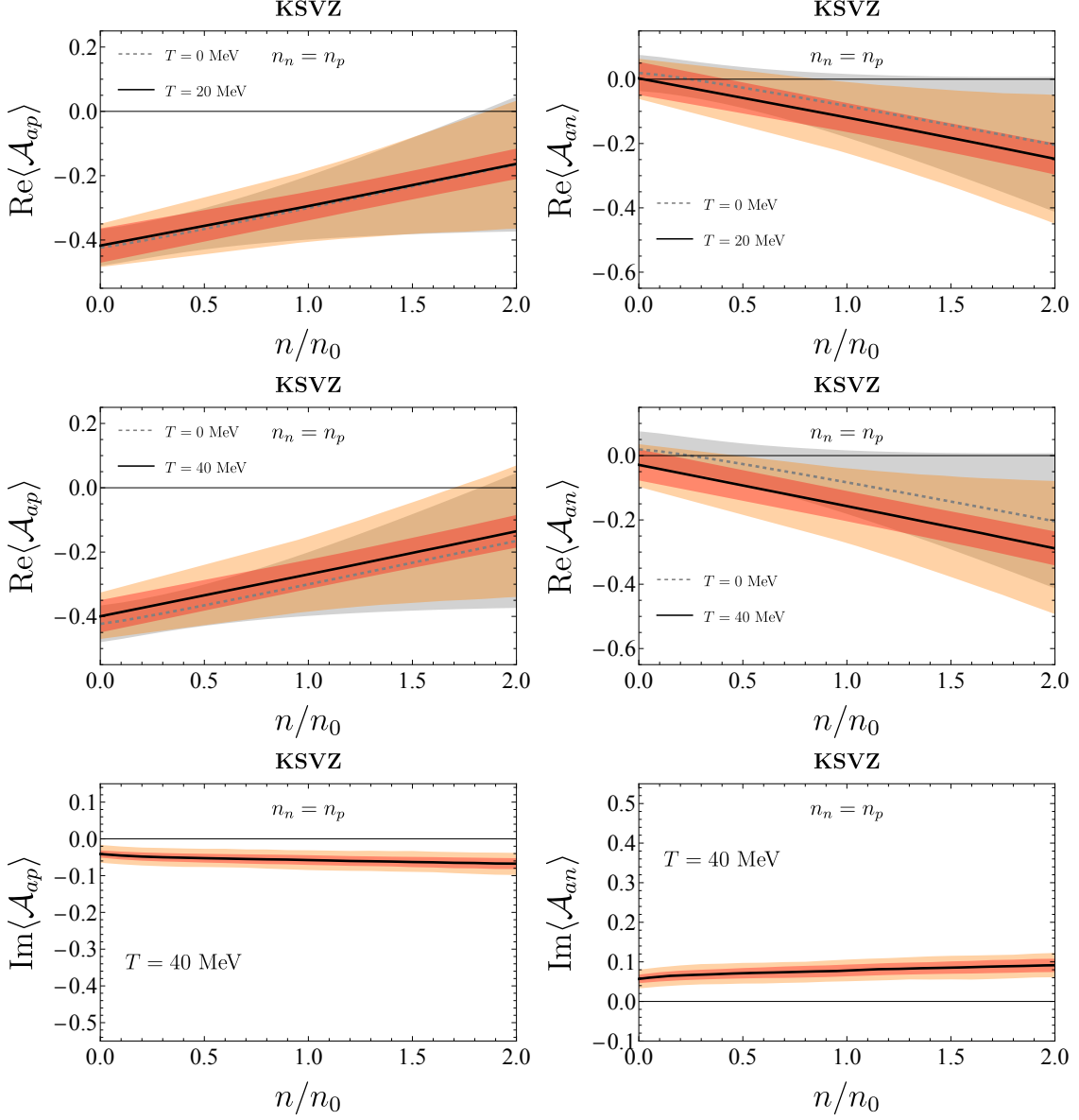


Figure 24: Density dependence of the KSVZ axion-nucleon couplings for $T = 20$ MeV and $T = 40$ MeV. Density is in units of nuclear saturation density n_0 . Error bars are shown as in Fig. 5. The dashed gray line represents the $T \rightarrow 0$ MeV result, with the gray area representing the combined error. For $T = 20$ MeV, we only show the real part of the form factor, as the imaginary part is negligibly small, as typical momenta are not above the pion threshold. On the other hand for $T = 40$ MeV, we show both real and imaginary parts.

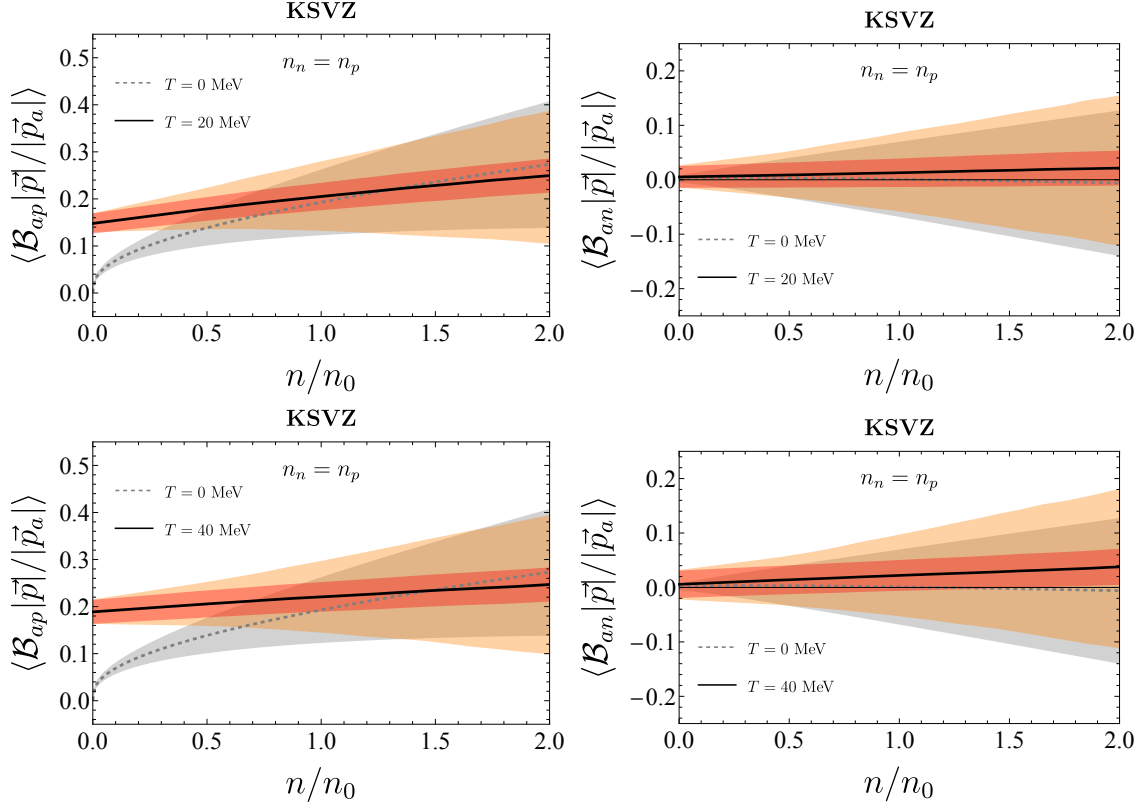


Figure 25: Density dependence of the KSVZ axion-nucleon couplings for $T = 20$ MeV and $T = 40$ MeV. Density is in units of nuclear saturation density n_0 . Error bars are shown as in Fig. 5. The dashed gray line represents the $T \rightarrow 0$ MeV result, while the gray area represents the combined error.

References

- [1] S. Weinberg, *A new light boson?*, *Phys. Rev. Lett.* **40** (Jan, 1978) 223–226.
- [2] F. Wilczek, *Problem of Strong P and T Invariance in the Presence of Instantons*, *Phys. Rev. Lett.* **40** (1978) 279–282.
- [3] R. D. Peccei and H. R. Quinn, *CP Conservation in the Presence of Instantons*, *Phys. Rev. Lett.* **38** (1977) 1440–1443.
- [4] C. Vafa and E. Witten, *Parity conservation in quantum chromodynamics*, *Phys. Rev. Lett.* **53** (Aug, 1984) 535–536.
- [5] J. Preskill, M. B. Wise, and F. Wilczek, *Cosmology of the Invisible Axion*, *Phys. Lett. B* **120** (1983) 127–132.
- [6] L. F. Abbott and P. Sikivie, *A Cosmological Bound on the Invisible Axion*, *Phys. Lett. B* **120** (1983) 133–136.
- [7] M. Dine and W. Fischler, *The Not So Harmless Axion*, *Phys. Lett. B* **120** (1983) 137–141.
- [8] G. Raffelt and D. Seckel, *Bounds on Exotic Particle Interactions from SN 1987a*, *Phys. Rev. Lett.* **60** (1988) 1793.

- [9] G. G. Raffelt, *Astrophysical methods to constrain axions and other novel particle phenomena*, *Phys. Rept.* **198** (1990) 1–113.
- [10] G. G. Raffelt, *Astrophysical axion bounds*, *Lect. Notes Phys.* **741** (2008) 51–71, [[hep-ph/0611350](#)].
- [11] N. Iwamoto, *Axion Emission from Neutron Stars*, *Phys. Rev. Lett.* **53** (1984) 1198–1201.
- [12] R. P. Brinkmann and M. S. Turner, *Numerical Rates for Nucleon-Nucleon Axion Bremsstrahlung*, *Phys. Rev. D* **38** (1988) 2338.
- [13] A. Burrows, M. S. Turner, and R. P. Brinkmann, *Axions and SN 1987a*, *Phys. Rev. D* **39** (1989) 1020.
- [14] A. Burrows, M. T. Ressel, and M. S. Turner, *Axions and SN1987A: Axion trapping*, *Phys. Rev. D* **42** (1990) 3297–3309.
- [15] M. S. Turner, *Axions from SN 1987a*, *Phys. Rev. Lett.* **60** (1988) 1797.
- [16] L. Di Luzio, M. Giannotti, E. Nardi, and L. Visinelli, *The landscape of QCD axion models*, *Phys. Rept.* **870** (2020) 1–117, [[arXiv:2003.01100](#)].
- [17] A. Caputo and G. Raffelt, *Astrophysical Axion Bounds: The 2024 Edition*, in *1st Training School of the COST Action COSMIC WISPerS (CA21106)*, 1, 2024. [arXiv:2401.13728](#).
- [18] M. S. Turner, *Axions, SN 1987a and One Pion Exchange*, *Phys. Rev. D* **40** (1989) 299–308.
- [19] M. Carena and R. D. Peccei, *The Effective Lagrangian for Axion Emission From SN1987A*, *Phys. Rev. D* **40** (1989) 652.
- [20] W. Keil, H.-T. Janka, D. N. Schramm, G. Sigl, M. S. Turner, and J. R. Ellis, *A Fresh look at axions and SN-1987A*, *Phys. Rev. D* **56** (1997) 2419–2432, [[astro-ph/9612222](#)].
- [21] T. E. O. Ericson and J. F. Mathiot, *Axion Emission from SN 1987a: Nuclear Physics Constraints*, *Phys. Lett. B* **219** (1989) 507–514.
- [22] M. Buschmann, C. Dessert, J. W. Foster, A. J. Long, and B. R. Safdi, *Upper Limit on the QCD Axion Mass from Isolated Neutron Star Cooling*, *Phys. Rev. Lett.* **128** (2022), no. 9 091102, [[arXiv:2111.09892](#)].
- [23] P. Carena, T. Fischer, M. Giannotti, G. Guo, G. Martínez-Pinedo, and A. Mirizzi, *Improved axion emissivity from a supernova via nucleon-nucleon bremsstrahlung*, *JCAP* **10** (2019), no. 10 016, [[arXiv:1906.11844](#)]. [Erratum: *JCAP* 05, E01 (2020)].
- [24] J. H. Chang, R. Essig, and S. D. McDermott, *Supernova 1987A Constraints on Sub-GeV Dark Sectors, Millicharged Particles, the QCD Axion, and an Axion-like Particle*, *JHEP* **09** (2018) 051, [[arXiv:1803.00993](#)].
- [25] G. Grilli di Cortona, E. Hardy, J. Pardo Vega, and G. Villadoro, *The QCD axion, precisely*, *JHEP* **01** (2016) 034, [[arXiv:1511.02867](#)].
- [26] A. Hook and J. Huang, *Probing axions with neutron star inspirals and other stellar processes*, *JHEP* **06** (2018) 036, [[arXiv:1708.08464](#)].
- [27] R. Balkin, J. Serra, K. Springmann, and A. Weiler, *The QCD axion at finite density*, *JHEP* **07** (2020) 221, [[arXiv:2003.04903](#)].
- [28] R. Balkin, J. Serra, K. Springmann, S. Stelzl, and A. Weiler, *Density Induced Vacuum Instability*, [arXiv:2105.13354](#).

- [29] R. Balkin, J. Serra, K. Springmann, S. Stelzl, and A. Weiler, *Runaway relaxation from finite density*, *JHEP* **06** (2022) 023, [[arXiv:2106.11320](#)].
- [30] R. Balkin, J. Serra, K. Springmann, S. Stelzl, and A. Weiler, *White dwarfs as a probe of exceptionally light QCD axions*, *Phys. Rev. D* **109** (2024), no. 9 095032, [[arXiv:2211.02661](#)].
- [31] R. Balkin, J. Serra, K. Springmann, S. Stelzl, and A. Weiler, *Heavy neutron stars from light scalars*, [arXiv:2307.14418](#).
- [32] A. Gómez-Bañón, K. Bartnick, K. Springmann, and J. A. Pons, *Constraining light QCD axions with isolated neutron star cooling*, [arXiv:2408.07740](#).
- [33] V. Bernard, N. Kaiser, and U.-G. Meissner, *Chiral dynamics in nucleons and nuclei*, *Int. J. Mod. Phys. E* **4** (1995) 193–346, [[hep-ph/9501384](#)].
- [34] C. Brandenstein, S. Stelzl, E. Gutsmedl, W. Schott, A. Weiler, and P. Fierlinger, *Towards an electrostatic storage ring for fundamental physics measurements*, *EPJ Web Conf.* **282** (2023) 01017, [[arXiv:2211.08439](#)].
- [35] M. Jiang, H. Su, A. Garcon, X. Peng, and D. Budker, *Search for axion-like dark matter with spin-based amplifiers*, *Nature Phys.* **17** (2021), no. 12 1402–1407, [[arXiv:2102.01448](#)].
- [36] **JEDI** Collaboration, S. Karanth et al., *First Search for Axionlike Particles in a Storage Ring Using a Polarized Deuteron Beam*, *Phys. Rev. X* **13** (2023), no. 3 031004, [[arXiv:2208.07293](#)].
- [37] C. Abel et al., *Search for Axionlike Dark Matter through Nuclear Spin Precession in Electric and Magnetic Fields*, *Phys. Rev. X* **7** (2017), no. 4 041034, [[arXiv:1708.06367](#)].
- [38] C. Gao, W. Halperin, Y. Kahn, M. Nguyen, J. Schütte-Engel, and J. W. Scott, *Axion Wind Detection with the Homogeneous Precession Domain of Superfluid Helium-3*, *Phys. Rev. Lett.* **129** (2022), no. 21 211801, [[arXiv:2208.14454](#)].
- [39] J. Lee, M. Lisanti, W. A. Terrano, and M. Romalis, *Laboratory Constraints on the Neutron-Spin Coupling of feV-Scale Axions*, *Phys. Rev. X* **13** (2023), no. 1 011050, [[arXiv:2209.03289](#)].
- [40] I. M. Bloch, Y. Hochberg, E. Kuflik, and T. Volansky, *Axion-like Relics: New Constraints from Old Comagnetometer Data*, *JHEP* **01** (2020) 167, [[arXiv:1907.03767](#)].
- [41] G. Vasilakis, J. M. Brown, T. W. Kornack, and M. V. Romalis, *Limits on New Long Range Nuclear Spin-Dependent Forces Set with a K-He3 Comagnetometer*, *PRL* **103** (Dec., 2009) 261801, [[arXiv:0809.4700](#)].
- [42] D. F. Jackson Kimball et al., *Overview of the Cosmic Axion Spin Precession Experiment (CASPER)*, *Springer Proc. Phys.* **245** (2020) 105–121, [[arXiv:1711.08999](#)].
- [43] T. Wu et al., *Search for Axionlike Dark Matter with a Liquid-State Nuclear Spin Comagnetometer*, *Phys. Rev. Lett.* **122** (2019), no. 19 191302, [[arXiv:1901.10843](#)].
- [44] A. Garcon et al., *Constraints on bosonic dark matter from ultralow-field nuclear magnetic resonance*, *Sci. Adv.* **5** (2019), no. 10 eaax4539, [[arXiv:1902.04644](#)].
- [45] K. Wei et al., *Dark matter search with a strongly-coupled hybrid spin system*, [arXiv:2306.08039](#).
- [46] Z. Xu et al., *Constraining Ultralight Dark Matter through an Accelerated Resonant Search*, [arXiv:2309.16600](#).

- [47] S. Chigusa, T. Moroi, K. Nakayama, and T. Sichanugrist, *Dark matter detection using nuclear magnetization in magnet with hyperfine interaction*, *Phys. Rev. D* **108** (2023), no. 9 095007, [[arXiv:2307.08577](#)].
- [48] **NASDUCK** Collaboration, I. M. Bloch, G. Ronen, R. Shaham, O. Katz, T. Volansky, and O. Katz, *New constraints on axion-like dark matter using a Floquet quantum detector*, *Sci. Adv.* **8** (2022), no. 5 abl8919, [[arXiv:2105.04603](#)].
- [49] **NASDUCK** Collaboration, I. M. Bloch, R. Shaham, Y. Hochberg, E. Kuflik, T. Volansky, and O. Katz, *Constraints on axion-like dark matter from a SERF comagnetometer*, *Nature Commun.* **14** (2023), no. 1 5784, [[arXiv:2209.13588](#)].
- [50] P. W. Graham, S. Hacıömeroğlu, D. E. Kaplan, Z. Omarov, S. Rajendran, and Y. K. Semertzidis, *Storage ring probes of dark matter and dark energy*, *Phys. Rev. D* **103** (2021), no. 5 055010, [[arXiv:2005.11867](#)].
- [51] V. M. Mostepanenko and G. L. Klimchitskaya, *The State of the Art in Constraining Axion-to-Nucleon Coupling and Non-Newtonian Gravity from Laboratory Experiments*, *Universe* **6** (2020), no. 9 147, [[arXiv:2009.04517](#)].
- [52] E. G. Adelberger, B. R. Heckel, S. A. Hoedl, C. D. Hoyle, D. J. Kapner, and A. Upadhye, *Particle Physics Implications of a Recent Test of the Gravitational Inverse Square Law*, *Phys. Rev. Lett.* **98** (2007) 131104, [[hep-ph/0611223](#)].
- [53] A. Bhusal, N. Houston, and T. Li, *Searching for Solar Axions Using Data from the Sudbury Neutrino Observatory*, *Phys. Rev. Lett.* **126** (2021), no. 9 091601, [[arXiv:2004.02733](#)].
- [54] J. Menendez, D. Gazit, and A. Schwenk, *Chiral two-body currents in nuclei: Gamow-Teller transitions and neutrinoless double-beta decay*, *Phys. Rev. Lett.* **107** (2011) 062501, [[arXiv:1103.3622](#)].
- [55] P. Gysbers et al., *Discrepancy between experimental and theoretical β -decay rates resolved from first principles*, *Nature Phys.* **15** (2019), no. 5 428–431, [[arXiv:1903.00047](#)].
- [56] E. Peik and C. Tamm, *Nuclear laser spectroscopy of the 3.5 eV transition in Th-229*, *Europhysics Letters* **61** (jan, 2003) 181.
- [57] C. J. Campbell, A. G. Radnaev, A. Kuzmich, V. A. Dzuba, V. V. Flambaum, and A. Derevianko, *Single-Ion Nuclear Clock for Metrology at the 19th Decimal Place*, *Phys. Rev. Lett.* **108** (Mar., 2012) 120802, [[arXiv:1110.2490](#)].
- [58] A. Caputo, D. Gazit, H.-W. Hammer, J. Kopp, G. Paz, G. Perez, and K. Springmann, *On the sensitivity of nuclear clocks to new physics*, [arXiv:2407.17526](#).
- [59] H. Kim and G. Perez, *Oscillations of atomic energy levels induced by QCD axion dark matter*, *Phys. Rev. D* **109** (2024), no. 1 015005, [[arXiv:2205.12988](#)].
- [60] E. Fuchs, F. Kirk, E. Madge, C. Paranjape, E. Peik, G. Perez, W. Ratzinger, and J. Tiedau, *Implications of the laser excitation of the Th-229 nucleus for dark matter searches*, [arXiv:2407.15924](#).
- [61] S. Weinberg, *Phenomenological Lagrangians*, *Physica A* **96** (1979), no. 1-2 327–340.
- [62] J. Gasser and H. Leutwyler, *Chiral Perturbation Theory to One Loop*, *Annals Phys.* **158** (1984) 142.
- [63] J. Gasser and H. Leutwyler, *Chiral Perturbation Theory: Expansions in the Mass of the Strange Quark*, *Nucl. Phys. B* **250** (1985) 465–516.

- [64] E. E. Jenkins and A. V. Manohar, *Baryon chiral perturbation theory using a heavy fermion Lagrangian*, *Phys. Lett. B* **255** (1991) 558–562.
- [65] S. Weinberg, *Nuclear forces from chiral Lagrangians*, *Phys. Lett. B* **251** (1990) 288–292.
- [66] S. Weinberg, *Effective chiral Lagrangians for nucleon - pion interactions and nuclear forces*, *Nucl. Phys. B* **363** (1991) 3–18.
- [67] S. Weinberg, *Three body interactions among nucleons and pions*, *Phys. Lett. B* **295** (1992) 114–121, [[hep-ph/9209257](#)].
- [68] V. Bernard, N. Kaiser, J. Kambor, and U. G. Meissner, *Chiral structure of the nucleon*, *Nucl. Phys. B* **388** (1992) 315–345.
- [69] S. Scherer, *Introduction to chiral perturbation theory*, *Adv. Nucl. Phys.* **27** (2003) 277, [[hep-ph/0210398](#)].
- [70] E. Epelbaum, H.-W. Hammer, and U.-G. Meissner, *Modern Theory of Nuclear Forces*, *Rev. Mod. Phys.* **81** (2009) 1773–1825, [[arXiv:0811.1338](#)].
- [71] N. Isgur and M. B. Wise, *Weak Decays of Heavy Mesons in the Static Quark Approximation*, *Phys. Lett. B* **232** (1989) 113–117.
- [72] E. Eichten and B. R. Hill, *An Effective Field Theory for the Calculation of Matrix Elements Involving Heavy Quarks*, *Phys. Lett. B* **234** (1990) 511–516.
- [73] H. Georgi, *An Effective Field Theory for Heavy Quarks at Low-energies*, *Phys. Lett. B* **240** (1990) 447–450.
- [74] A. V. Manohar and M. B. Wise, *Heavy quark physics*, vol. 10. 2000.
- [75] E. E. Jenkins and A. V. Manohar, *Chiral corrections to the baryon axial currents*, *Phys. Lett. B* **259** (1991) 353–358.
- [76] K. Springmann, M. Stadlbauer, S. Stelzl, and A. Weiler, *Model-independent supernova bound on the QCD axion*, *In preparation*.
- [77] L. Di Luzio, F. Mescia, E. Nardi, P. Panci, and R. Ziegler, *Astrophobic Axions*, *Phys. Rev. Lett.* **120** (2018), no. 26 261803, [[arXiv:1712.04940](#)].
- [78] G. Lucente, L. Mastrototaro, P. Carena, L. Di Luzio, M. Giannotti, and A. Mirizzi, *Axion signatures from supernova explosions through the nucleon electric-dipole portal*, *Phys. Rev. D* **105** (2022), no. 12 123020, [[arXiv:2203.15812](#)].
- [79] **Particle Data Group** Collaboration, R. L. Workman et al., *Review of Particle Physics*, *PTEP* **2022** (2022) 083C01.
- [80] **Flavour Lattice Averaging Group (FLAG)** Collaboration, Y. Aoki et al., *FLAG Review 2021*, *Eur. Phys. J. C* **82** (2022), no. 10 869, [[arXiv:2111.09849](#)].
- [81] T. Vonk, F.-K. Guo, and U.-G. Meißner, *Precision calculation of the axion-nucleon coupling in chiral perturbation theory*, *JHEP* **03** (2020) 138, [[arXiv:2001.05327](#)].
- [82] U.-G. Meissner, G. Müller, and S. Steininger, *Renormalization of the chiral pion - nucleon Lagrangian beyond next-to-leading order*, *Annals Phys.* **279** (2000) 1–64, [[hep-ph/9809446](#)].
- [83] J. Kambor and M. Mojziz, *Field redefinitions and wave function renormalization to $O(p^{**4})$ in heavy baryon chiral perturbation theory*, *JHEP* **04** (1999) 031, [[hep-ph/9901235](#)].
- [84] V. Bernard and U.-G. Meissner, *The Nucleon axial-vector coupling beyond one loop*, *Phys. Lett. B* **639** (2006) 278–282, [[hep-lat/0605010](#)].

- [85] G. Colangelo, J. Gasser, and H. Leutwyler, $\pi\pi$ scattering, *Nucl. Phys. B* **603** (2001) 125–179, [[hep-ph/0103088](#)].
- [86] D. Siemens, V. Bernard, E. Epelbaum, A. M. Gasparyan, H. Krebs, and U.-G. Meißner, *Elastic and inelastic pion-nucleon scattering to fourth order in chiral perturbation theory*, *Phys. Rev. C* **96** (2017), no. 5 055205, [[arXiv:1704.08988](#)].
- [87] M. Hoferichter, J. Ruiz de Elvira, B. Kubis, and U.-G. Meißner, *Matching pion-nucleon Roy-Steiner equations to chiral perturbation theory*, *Phys. Rev. Lett.* **115** (2015), no. 19 192301, [[arXiv:1507.07552](#)].
- [88] E. Epelbaum, U. G. Meissner, W. Gloeckle, and C. Elster, *Resonance saturation for four nucleon operators*, *Phys. Rev. C* **65** (2002) 044001, [[nucl-th/0106007](#)].
- [89] T. Vonk, F.-K. Guo, and U.-G. Meißner, *The axion-baryon coupling in $SU(3)$ heavy baryon chiral perturbation theory*, *JHEP* **08** (2021) 024, [[arXiv:2104.10413](#)].
- [90] A. J. Niemi and G. W. Semenoff, *Thermodynamic Calculations in Relativistic Finite Temperature Quantum Field Theories*, *Nucl. Phys. B* **230** (1984) 181–221.
- [91] A. J. Niemi and G. W. Semenoff, *Finite Temperature Quantum Field Theory in Minkowski Space*, *Annals Phys.* **152** (1984) 105.
- [92] N. P. Landsman and C. G. van Weert, *Real and Imaginary Time Field Theory at Finite Temperature and Density*, *Phys. Rept.* **145** (1987) 141.
- [93] L. Di Luzio, V. Fiorentino, M. Giannotti, F. Mescia, and E. Nardi, *Do Finite Density Effects Jeopardize Axion Nucleophobia in Supernovae?*, [arXiv:2410.04613](#).
- [94] M. Ghosh, Y. Grossman, W. Tangarife, X.-J. Xu, and B. Yu, *Neutrino forces in neutrino backgrounds*, *JHEP* **02** (2023) 092, [[arXiv:2209.07082](#)].
- [95] **Kamiokande-II** Collaboration, K. Hirata et al., *Observation of a Neutrino Burst from the Supernova SN 1987a*, *Phys. Rev. Lett.* **58** (1987) 1490–1493.
- [96] R. M. Bionta et al., *Observation of a Neutrino Burst in Coincidence with Supernova SN 1987a in the Large Magellanic Cloud*, *Phys. Rev. Lett.* **58** (1987) 1494.
- [97] G. G. Raffelt, *Stars as laboratories for fundamental physics: The astrophysics of neutrinos, axions, and other weakly interacting particles*. 5, 1996.
- [98] K. Choi, H. J. Kim, H. Seong, and C. S. Shin, *Axion emission from supernova with axion-pion-nucleon contact interaction*, [arXiv:2110.01972](#).
- [99] S. Bacca, K. Hally, C. J. Pethick, and A. Schwenk, *Chiral effective field theory calculations of neutrino processes in dense matter*, *Phys. Rev. C* **80** (2009) 032802, [[arXiv:0812.0102](#)].
- [100] G. I. Lykasov, C. J. Pethick, and A. Schwenk, *A Unified approach to structure factors and neutrino processes in nucleon matter*, *Phys. Rev. C* **78** (2008) 045803, [[arXiv:0808.0330](#)].
- [101] A. Bartl, C. J. Pethick, and A. Schwenk, *Supernova matter at subnuclear densities as a resonant Fermi gas: Enhancement of neutrino rates*, *Phys. Rev. Lett.* **113** (2014) 081101, [[arXiv:1403.4114](#)].
- [102] A. Bartl, R. Bollig, H.-T. Janka, and A. Schwenk, *Impact of Nucleon-Nucleon Bremsstrahlung Rates Beyond One-Pion Exchange*, *Phys. Rev. D* **94** (2016) 083009, [[arXiv:1608.05037](#)].
- [103] C. Hanhart, D. R. Phillips, and S. Reddy, *Neutrino and axion emissivities of neutron stars from nucleon-nucleon scattering data*, *Phys. Lett. B* **499** (2001) 9–15, [[astro-ph/0003445](#)].

- [104] A. Schwenk, P. Jaikumar, and C. Gale, *Neutrino bremsstrahlung in neutron matter from effective nuclear interactions*, *Phys. Lett. B* **584** (2004) 241–250, [[nucl-th/0309072](#)].
- [105] K. Springmann, M. Stadlbauer, S. Stelzl, and A. Weiler, *Impact of Nucleon-Nucleon interaction in supernova environments*, *In preparation*.
- [106] G. Raffelt and D. Seckel, *Multiple scattering suppression of the bremsstrahlung emission of neutrinos and axions in supernovae*, *Phys. Rev. Lett.* **67** (1991) 2605–2608.
- [107] Garching Core-Collapse Supernova Archive:
<https://wwwmpa.mpa-garching.mpg.de/ccsnarchive/>.
- [108] R. Bollig, W. DeRocco, P. W. Graham, and H.-T. Janka, *Muons in Supernovae: Implications for the Axion-Muon Coupling*, *Phys. Rev. Lett.* **125** (2020), no. 5 051104, [[arXiv:2005.07141](#)]. [Erratum: *Phys.Rev.Lett.* 126, 189901 (2021)].
- [109] M. Rampp and H. T. Janka, *Radiation hydrodynamics with neutrinos: Variable Eddington factor method for core collapse supernova simulations*, *Astron. Astrophys.* **396** (2002) 361, [[astro-ph/0203101](#)].
- [110] A. Marek, H. Dimmelmeier, H. T. Janka, E. Muller, and R. Buras, *Exploring the relativistic regime with Newtonian hydrodynamics: An Improved effective gravitational potential for supernova simulations*, *Astron. Astrophys.* **445** (2006) 273, [[astro-ph/0502161](#)].
- [111] R. Buras, M. Rampp, H. T. Janka, and K. Kifonidis, *Two-dimensional hydrodynamic core-collapse supernova simulations with spectral neutrino transport. 1. Numerical method and results for a 15 solar mass star*, *Astron. Astrophys.* **447** (2006) 1049–1092, [[astro-ph/0507135](#)].
- [112] N. Iwamoto, *Nucleon-nucleon bremsstrahlung of axions and pseudoscalar particles from neutron star matter*, *Phys. Rev. D* **64** (2001) 043002.
- [113] D. G. Yakovlev, A. D. Kaminker, O. Y. Gnedin, and P. Haensel, *Neutrino emission from neutron stars*, *Phys. Rept.* **354** (2001) 1, [[astro-ph/0012122](#)].
- [114] D. G. Yakovlev and K. P. Levenfish, *Modified URCA process in neutron star cores.*, *A&A* **297** (May, 1995) 717.
- [115] R. Mayle, J. R. Wilson, J. R. Ellis, K. A. Olive, D. N. Schramm, and G. Steigman, *Updated Constraints on Axions from SN 1987a*, *Phys. Lett. B* **219** (1989) 515.
- [116] S. Goriely, N. Chamel, and J. M. Pearson, *Further explorations of Skyrme-Hartree-Fock-Bogoliubov mass formulas. 13. The 2012 atomic mass evaluation and the symmetry coefficient*, *Phys. Rev. C* **88** (2013), no. 2 024308.
- [117] A. Caputo, K. Springmann, M. Stadlbauer, S. Stelzl, and A. Weiler, *Systematic neutrino production at finite density and temperature*, *In preparation*.
- [118] N. Fettes, U.-G. Meissner, M. Mojzsis, and S. Steininger, *The Chiral effective pion nucleon Lagrangian of order p^{**4}* , *Annals Phys.* **283** (2000) 273–302, [[hep-ph/0001308](#)]. [Erratum: *Annals Phys.* 288, 249–250 (2001)].
- [119] E. Epelbaum, A. Nogga, W. Gloeckle, H. Kamada, U. G. Meissner, and H. Witala, *Three nucleon forces from chiral effective field theory*, *Phys. Rev. C* **66** (2002) 064001, [[nucl-th/0208023](#)].
- [120] H. A. Weldon, *Simple Rules for Discontinuities in Finite Temperature Field Theory*, *Phys. Rev. D* **28** (1983) 2007.

- [121] W. Keil, *Radiative Corrections and Renormalization at Finite Temperature: A Real Time Approach*, *Phys. Rev. D* **40** (1989) 1176.
- [122] R. J. Furnstahl and B. D. Serot, *Covariant Feynman rules at finite temperature: Time-path formulation*, *Phys. Rev. C* **44** (1991) 2141–2174.
- [123] R. L. Kobes and G. W. Semenoff, *Discontinuities of Green Functions in Field Theory at Finite Temperature and Density. 2*, *Nucl. Phys. B* **272** (1986) 329–364.
- [124] R. E. Cutkosky, *Singularities and discontinuities of Feynman amplitudes*, *J. Math. Phys.* **1** (1960) 429–433.
- [125] M. J. G. Veltman, *Diagrammatica: The Path to Feynman rules*, vol. 4. Cambridge University Press, 5, 2012.
- [126] G. 't Hooft and M. J. G. Veltman, *DIAGRAMMAR*, *NATO Sci. Ser. B* **4** (1974) 177–322.
- [127] R. L. Kobes and G. W. Semenoff, *Discontinuities of Green Functions in Field Theory at Finite Temperature and Density*, *Nucl. Phys. B* **260** (1985) 714–746.
- [128] P. F. Bedaque, A. K. Das, and S. Naik, *Cutting rules at finite temperature*, *Mod. Phys. Lett. A* **12** (1997) 2481–2496, [[hep-ph/9603325](#)].
- [129] P. Carena, B. Fore, M. Giannotti, A. Mirizzi, and S. Reddy, *Enhanced Supernova Axion Emission and its Implications*, *Phys. Rev. Lett.* **126** (2021), no. 7 071102, [[arXiv:2010.02943](#)].
- [130] J. W. Holt, N. Kaiser, and W. Weise, *Density-dependent effective nucleon-nucleon interaction from chiral three-nucleon forces*, *Phys. Rev. C* **81** (2010) 024002, [[arXiv:0910.1249](#)].
- [131] J. W. Holt, M. Kawaguchi, and N. Kaiser, *Implementing chiral three-body forces in terms of medium-dependent two-body forces*, *Front. in Phys.* **8** (2020) 100, [[arXiv:1912.06055](#)].
- [132] N. Fettes, U.-G. Meissner, and S. Steininger, *Pion - nucleon scattering in chiral perturbation theory. 1. Isospin symmetric case*, *Nucl. Phys. A* **640** (1998) 199–234, [[hep-ph/9803266](#)].